XAFS studies on the well-defined fuel cell model catalysts

燃料電池モデル触媒の XAFS 研究

Kaiyue Dong

董凱悦

Division of Quantum Science and Engineering

Graduate School of Engineering, Hokkaido University

June 2024

Abstract

To meet the target of carbon neutralization society and solve the critical issue arising from the depletion of traditional fossil storage and high demand for renewable energy resources, fuel cell technology provides a promising solution to the problems. Oxygen reduction reaction (ORR) at cathode side of fuel cells is the crucial rate determining step, which is accelerated by the monometallic Pt and bimetallic Pt-based PtM (M=Pd, Au, etc) alloy nanoparticles (NPs) catalysts supported on porous carbons. In order to increase the activity and durability and to further contribute to the development of fuel cell, it is significantly important to investigate the relationship between the electronic and geometric structures of Pt (PtM) nanoparticles and their activities. Nevertheless, these porous carbon powder catalyst supports usually exhibit an ill-defined structure, which is hard to give an exact description of structure and related active sites. An alternative way is to use a model catalyst system to make it possible to apply surface science techniques to reveal the detailed structures at atomic scales. Furthermore, *in situ* characterization must be necessary to obtain precise insights into real reaction processes. X-ray absorption fine structure (XAFS) is the most suitable surface science technique, which allows us to carry out *in situ* characterization of electronic and geometric structures of Pt (PtM) NPs on atomic level. However, when I tried to apply it to the model systems, new developments in XAFS techniques are needed. In this work I developed three new XAFS techniques: a bent crystal Laue analyzer + back illuminated / high energy resolution fluorescence detection X-ray absorption fine structure (BCLA+BI/HERFD-XAFS), BCLA enhanced polarization-dependent total reflection fluorescence XAFS (BCLA+PTRF-XAFS) technique, and *in situ* electrochemical PTRF-XAFS (EC-PTRF-XAFS) technique. These new XAFS techniques are applied to the Pt-based model systems. I found several new and important concepts for the development of noble metal Pt-based ORR catalysts.

The first chapter gave a general introduction.

The second chapter described experimental methods and analysis details, which included model catalyst preparation for monometallic (Pt) and bimetallic Pt-based (PtM) model catalyst systems, development of *in-situ* electrochemical XAFS apparatus, and related surface science characterizations.

The third chapter described the investigation of model catalyst structure for monometallic Pt NPs in a small amount (~ 10^{15} Pt atoms cm^{-2}) supported on the flat HOPG. A novel BCLA/HERFD-BI-XAFS method was applied for the structure study under *in-situ* conditions

which corresponded to the ORR reactions. Structure framework and surface adsorbates were successfully investigated.

The fourth chapter focused on the development of *in-situ* EC-BCLA+PTRF-XAFS measurement apparatus for structure studies of diluted noble metals supported by single crystal surfaces. The limited target element amount and enormous elastic scatterings arises from solutions hinders the *in-situ* EC-XAFS studies. The applications of BCLA perfectly solved abovementioned problems with delicate adjustment between the BCLA position and X-ray footprints, especially for EXAFS of bimetallic PtAu system under solution free case, for which elements possess a close absorption energy edge. Nevertheless, the application of BCLA in for diluted PtAu model catalyst system under solution condition didn't significantly choose the target Pt fluorescence signals because of huge contribution of inelastic scatterings arise from solutions was too large to be easily removed by simply application of BCLA monochromator. Further improvements should be considered to eliminate the negative solution effect in *in-situ* XAFS measurement.

In the fifth chapter, I challenged to apply the developed *in-situ* PTRF-XAFS technique to track the formation process of spontaneously deposited $[PtCl_4]^{2-}$ species under *in-situ* conditions. The as-prepared sample with a very limited Pt amount (~ 0.2 ML) formed via self-deposition method, where a planar structure $[PtCl_4]^{2-}$ was assumed in Feff8 theoretical simulation.

In the sixth chapter, I successfully applied the *in-situ* EC-PTRF-XAFS method to the bimetallic Pt-based model catalyst system of Pt sub-ML supported by Au (111), and confirmed the strain effect in this model system. The Pt-Pt bond distance in this model catalyst was expanded to Au-Au in Au foil as 2.88 Å, which was induced by Au (111) underlying substrate because of lattice constant between Pt and Au species.

The seventh chapter gave the general conclusion of the dissertation. I successfully developed three XAFS methods suitable for structure investigation of monometallic and bimetallic Pt-based model catalysts for ORR under *in-situ* conditions. The developed XAFS apparatus will be contribute to the catalyst fundamental research, which is possible to establish the relationship between the Pt-based catalyst and corresponding ORR catalytic activities and further providing an essential guiding line for ORR catalyst design.

Contents

Preface

This PhD work couldn't be finished without a lot of peoples' help. First of all, I would like to express my deepest appreciation to my supervisor Prof. Kiyotaka Asakura. I was deeply inspired by his attitude toward new scientific challenges as well as positive personalities. It was his overwhelming encouragement and support during those tough days that helped me get through the depressions. The three promises we made in this laboratory, always focusing on interested research, cooperating with others, and respecting people, will always accompany me.

I would like to show my sincere appreciation to Prof. Satoru Takakusagi for his professional guidance in the electrochemistry field as well as kind discussions. I was able to carry out and design the experiments accordingly to finish a lot of this dissertation work with his help.

Thanks to Dr. Kido and Dr. Lu for their kind guidance in academic research and patience in discussions from fundamental knowledge to applications. Thanks for Dr. Wada's kindness in technique assistance and kind help throughout five years' beamtime. In addition, I would like to thank all members of Asakura Laboratory for the great time we had in the past five years.

Thanks to all professors in Division of Quantum Science and Engineering, especially for Prof. Kamiyama's kindness for having me during my last three months' Doctor Course. Additionally, I would like to thank all staffs in the technique division of ICAT in Hokkaido University, BL12C, BL15A, and NW10A in KEK and BL36XU in SPring-8.

Finally, and most importantly, I would like to extend my great thanks to my parents. I couldn't have made it so far without their firm support.

Chapter 1 General Introduction

1.1 Overview

The rapid population growth worldwide and the development of technological advancements have drawn a larger requirement for power sources, as well as extended the need for transportation, where the fossil fuel remains the largest contribution to the world energy demand[1,2]. The combustion of fossil fuels raises negative environmental issues, such as greenhouse gas emission and climate changes[3,4]. In addition, the storage of traditional fossil fuels are depleting, which forces the exploration toward a more sustainable sectors, such as solar energy, wind energy, or hydrogen energy, etc. with lower pollutant emissions, to deal with the increasing energy demand[5]. Among these developed alternative energy schemes, hydrogen fuel-driven polymer electrolyte membrane fuel cells (PEMFCs) showed an outstanding potential owing to several advantages: high efficiency, durability, low noise, no tailpipe emission other than water, low operating temperature and fast start[6]. PEMFCs are a galvanic system that convert the chemical energy contained in the fuels into electricity, where the hydrogen oxidation reaction (HOR) occurs at the anode side to oxidize the hydrogen fuel into proton, whereas the oxygen reduction reaction (ORR) takes place at the cathode side to reduce the oxygen to water in acidic environment[7], as shown in Figure 1-1. Catalysts layer is usually applied in the cathode side because it effectively lowers the activation energy to accelerate the overall reaction rate to the target products without changing itself before and after reaction[8–10]. As the chemical reactions occurs over the catalyst surface or near the surface, the geometric structure of catalyst affect the ORR catalytic activity and selectivity[11]. The special surface morphology and highly active facets of these structures show a better ORR performance than the conventional Pt/C catalysts. In addition, the electronic structure can also change the catalytic activity by changing the d-band center position or via charge transfer

effect[12]. Therefore, it is necessary to systematically investigate how does the geometric and electronic structure affect the ORR catalytic activity in detail, which will provide a fundamental understanding of structure-activity relationship for ORR research. Furthermore, the advanced characterization techniques offers a great opportunity to get deeper understanding toward working principle of Pt-based catalysts under real operating conditions, which is crucial for establishing the rational structure design guidance for high performance catalysts and facilitating the wide application of PEMFCs.

1.2 Rate determining step of fuel cell and catalytic mechanisms in ORR Process.

The chemical reaction occurs in the PEMFCs can be summarized as follows:

$$Anode\ side\ (Hydrogen\ oxidation\ reaction): 2H_2 - 4e^- \rightarrow 4H^+, E^0 = 0\ V\ (E\ vs\ RHE) \tag{1-1}$$

$$Cathode\ side\ (Oxygen\ reduction\ reaction): O_2 + 4e^- + 4H^+ \rightarrow 2H_2O, E^0 = 1.23\ V\ (E\ vs\ RHE) \tag{1-2}$$

It is worth mentioning that the catalyst layer is usually applied in the cathode side because it effectively lowers the activation energy to accelerate the overall reaction rate without changing itself before and after reaction, as shown in Figure 1-2. The precious group metals (PGMs), such as Pt and Pd are commonly used as the most effective electrocatalysts for ORR. It should be noted that the cathode side contains more than 80% of all PGMs used in the device compared to the usage in the anode. However, the reaction kinetic for ORR is six orders lower than that of anode for HOR[13,14]. The ORR occurs at the cathode side is regarded as the rate determined step because of the kinetic requirements of four electrons or kinetically retarded four electron process.

The detailed ORR reaction steps involve multiple intermediates formation processes. Typically, a four-electron driven ORR process proceeds through a dissociative or associative pathway[15–17], depending on whether the adsorbed O_2 molecules dissociates before reduction:

Dissociative pathway:

$$O_2^* \rightarrow O^* + O^*$$

$$O^* + H^+ + e^- \rightarrow OH^*$$

$$OH^* + H^+ + e^- \rightarrow H_2O^*$$

(1-3)

Associative Pathway:

$$O_2^* + H^+ + e^- \rightarrow OOH^*$$

$$OOH^* \rightarrow O^* + OH^*$$

$$O^* + H^+ + e^- \rightarrow OH^*$$

$$OH^* + H^+ + e^- \rightarrow H_2O^*$$

(1-4)

When the O_2 molecules are firmly bound to the catalyst surface, or the oxygen coverage is low, the dissociative route is preferred. However, when the O_2 is weakly adsorbed on the catalyst surface, or the surface oxygen coverage is elevated, the associative pathway is preferred. Figure 1-3 shows the schematic illustration of ORR pathways and corresponding intermediates.

The relationship between the adsorbed species and the catalysts surface is crucial for improving catalytic activities, which is revealed by the Sabatier principle. The chemical bond between the

catalyst surface and oxygen species should be neither overly strong nor too weak because the ORR kinetics would be hindered by the electron or proton transfer processes. The classic volcanic diagram demonstrates the relationship between the ORR activity and oxygen binding energy with catalysts, as shown in Figure 1-4. According to Nørskov's reports[18], the ORR kinetic rate is dictated by the metal d-band center. The shift of d-band center with respect to Fermi level has a significant effect on adsorbate-metal bonding strength, which further contribute to the catalytic activity[19,20]. For instance, if the d-band center of the metal catalyst is too high, the oxygen will strongly bind to the catalyst surface, leading to hard desorption process of oxygenated intermediates and block of active sites. On the contrary, if the d-band center is too lower, the surface kinetics of electron/proton transfer process is hindered due to the weak binding between the oxygen and catalyst surfaces. In this realm, d-band center should be carefully tuned to achieve the higher catalytic activity.

1.3 Carbon supported Pt Monometallic Catalysts

Porous carbon supported Pt species powder catalyst showed an outstanding performance in ORR[21–24]. Carbon materials possess a high surface area and sufficient porosity to support highly dispersed Pt NPs, as well as excellent electronic conductivity and chemical stability. Figure 1-5 shows TEM image for the carbon black supported Platinum. Commercially available carbon blacks, such as Vulcan XC-72 and Ketjen Black, are the most widely used high surface area carbon-based catalysts support in PEMFCs. However, the dissolution of the carbon support and the weak connection between the Pt particles and the carbon support severely limited the catalyst stability[25]. Considering from the aspect from the Pt NPs, the application of expensive noble metal Pt has greatly inhibited the wide spreading of fuel cell technology. In addition, the Pt species can be oxidized into PtO, PtO_2, and PtO_3 at higher potentials, and dissolve as Pt^{2+} in acidic

environments[26]. This process is a facet-dependent process that involves different surface species. With the increase of the applying potential, at Pt(100), the anode dissolution occurs because of Pt oxidation when the potential is higher than 1.0 V. For Pt(111), the anodic dissolution begins at a potential more than 1.2 V, which confirms that the Pt(111) has a better stability than Pt(100)[27]. Besides, the aggregation of Pt species occurs because of Ostwald ripening process or electrochemical processes[26,28]. Consequently, the number of active sites decreases in this process, leading to less utilization of Pt atoms. Figure 1-6 shows the schematic diagram of the loss mechanism of Pt/C catalysts in ORR[29].

1.4 Pt-based Bimetallic Catalysts

Given the fact that the carbon supported monometallic Pt species are suffering several drawbacks. An alternative way to improve the Pt utilization as well as improve the ORR activity is to use Pt-based bimetallic electrocatalysts for ORR[30–32]. The bimetallic catalyst contributes to the catalytic activity via synergistic effects where Pt-M' metal bonding plays an essential role[33]. It has been demonstrated by DFT that the synergistic effect in bimetallic system can decrease the reaction activation energy[34], which can be classified into three types as follows:

1. Geometric / strain effect

   The lattice mismatch between two metallic components can lead to changes in atomic spacing and metal-metal bond distance, the modified geometric configuration contributes to the improved ORR activity[35,36]. It has been reported that the Au-Pt bimetallic nanoparticle showed higher catalytic performance with a lattice expansion in Pt and a shrink in Au[37].
2. Electronic / ligand effect

The electron environment in bimetallic system is altered by the introduction of a second metal species, where the electronic configuration of the active metal site can be altered, or the electron transfer between the metals occurs, both helps in modification of d-band center, which is closely related to the adsorption strength of the ORR intermediates. The introduction of Cu to Ag NPs modified the Fermi level to a more moderate state, the altered electronic structure can significantly improve the ORR catalytic activity[38].

3. Stabilizing effect

   The introduction of the second metal into metallic catalyst improve the stability of active metal in the system. Pt_6Ru_1/C catalyst showed a higher SO_2 poisoning property because Ru metal is less poisoned by SO_2[39].

1.5 Structure Determined Catalytic Activity and Application of Model Catalyst Systems

As the chemical reactions take place over the catalyst surface or near the surface, the catalyst surface morphology and facets significantly affect the ORR catalytic activity and selectivity. Various Pt-based bimetallic shape-selective catalysts have been studied, such as core@shell[40], nanowire[41], nanotube[42], and nanoframe[43], etc. It is necessary to systematically investigate how does the structure parameters in those specially designed structures[44] affect the ORR catalytic activity especially at atomic scales.

The practical chemical reaction usually involves multiple steps, where adsorption, diffusion, dissociation of reactant, and desorption of products occurs in sequence. Each step occurs on different surface-active sites, the complex mechanism hampers the detailed understanding toward the overall reaction process. The application of a simplified model catalyst could solve this problem. The model catalyst system usually consisted of a well-defined substrate, such as metal single crystal, or the metal oxide single crystals, with a deposition of monolayer (ML) or

submonolayer (subML) noble metal species, these materials can effectively simulate the complex practical catalyst systems to establish a fundamental understanding of the surface structure, and metal-support effect on catalytic activity and selectivity[45,46]. In summary, it is possible to reveal the relationship between the catalyst structure and catalytic activity by applying model catalysts.

1.6 Surface Science techniques

1.6.1 In-situ Surface Science Application and Limitations

The capturing of active sites, concomitant intermediates as well as the reaction products during the conversion and reconstruction process is challenging to elucidating the ORR mechanism since the catalyst layer undergoes a complex dynamic evolution in the practical chemical reaction process[47]. In this realm, it is necessary to apply various *in-situ* surface science techniques to track the real-time evolution of catalyst structures, for example, phase transition, electronic transfer trend, coordination variation as well as the trace of catalyst surface adsorption and desorption behavior, and products formation process.

For phase transition study, mostly used method is X-ray Diffraction (XRD), which can provide unique patterns for periodically structured materials to reveal the crystallographic information for materials. The *in-situ* XRD can provide real-time crystalline phase transition information by detecting diffraction patterns varied with time for catalysts. Escudero-Escribano et al[48]. reported a phase transition study for Pt overlayer formed on Gd/Pt(111) alloys during ORR by applying *in-situ* synchrotron grazing incidence XRD method. This method elucidated the formation of slight compressive strain relaxation in Pt overlayer during the repetition of electrochemical cycling during ORR potential region. The stable structure framework maintained with the persistence of 0.8% compressive strain even after 8000 cycles. This work proved that the Pt overlayer with a compressive strain act as the main active sites for ORR. However, for low-crystallinity materials,

it is hard to track the phase properties. Local sites phase information is also hard to be studied by *in-situ* XRD.

For *in-situ* catalyst surface morphology investigation, scanning/transmission electron microscopy (S/TEM) can be applied to obtain the crystal structure information like interlayer spacing. S/TEM is usually divided into two kinds of imagery models, bright field images and high-angle annular dark-fields (HAADF) imaging. The latter depicts structure information at atomic level. Furthermore, these models are usually equipped with electron energy loss spectroscopy (EELS) and energy dispersive X-ray spectroscopy to facilitate the investigation of elemental, component, and electronic configuration information for catalysts. Gocyla et al.[49] adopted an *in-situ* TEM to observe the morphology evolution of outmost atomic layer for octahedral $PtNi_{1.5}$ NP had a concaved octahedral structure with a rich Pt edge and rich Ni facets. Dai et al.[50] used the *in-situ* TEM to check the surface composition of the disordered Pt_3Co NPs and related dynamic changes for morphology evolutions during the *in-situ* heating conditions. However, *in-situ* TEM has a high requirement in material preparation and operating environment especially under liquid environment, model catalyst with thickness in millimeter order cannot be applied. Scanning probing microscopies is an alternative technique to reveal surface morphologies. For example, *in-situ* AFM can provide vertical morphology of the catalyst surface using a constant repulsive / attraction force between the tip and the catalyst interface. AFM works independently from material conductivity. Nevertheless, manipulating the contact between the cantilever and sample surface under solution condition is very challenging.

The *in-situ* Fourier Transform Infrared Spectroscopy (FT-IR) spectrum allows real-time investigation of groups generated on catalyst surface during ORR process. The problem is the IR light is sensitive to water molecules, which made the signal of *in-situ* IR spectrum very weak.

Raman spectroscopy can help to identify structural information of molecules with Raman active vibrational modes. The development of surface enhanced Raman spectroscopy (SERRS) and shell-separated nanoparticle-enhanced Raman spectroscopy (SHINERS) successfully provided in-depth investigation in revealing ORR mechanisms. Even in aqueous solutions, the vibrational and rotational energy levels of intermediates on the Pt surface can be acquired[51,52]. These two methods focus on elucidating the kind of surface adsorbates instead of explaining the effect of surface adsorbates on metal species, whereas the latter is essential for catalyst structure studies.

To investigate the valence state or electronic structure variation during the chemical reaction process, X-ray photoelectron spectroscopy (XPS) and X-ray absorption fine structure (XAFS) might be good candidates. XPS is a surface sensitive technique, which utilize the photoelectron effect to obtain qualitative distinguish for compositional analysis and oxidation state for elements consisted in catalyst material, and quantitative analysis for elemental amount studies. However, XPS requires an ultra-high vacuum (UHV) condition, which is hard for structure investigation especially in solid-liquid interface studies. Because travelling path of emitted photoelectrons are greatly limited by the element-specific mean free path, especially blocked in the liquid environment. As one of surface sensitive techniques, XAFS has achieved this target by applying the total reflection condition. For example, when applying the flat single crystals, the X-ray incidents in a very small angle, it doesn't have to travel through a long path within single crystal bulk. Therefore, only the structure information near the surface are investigated. XAFS measurements have been successfully applied to trace the electron transfer behavior during ORR. For example, the Pt L_3 edge reflects the dipole transition from 2p to 5d orbitals, therefore, the valence state change can be directly observed from the whiteline (WL) intensity in XANES spectra[53]. Pt oxide formation at high electrochemical potentials on PEMFCs cathodes was

assumed by comparing the WL peak properties at different potentials and under electrolyte environment. For bimetallic catalysts, electron transfer trend can be determined via comparing the WL property variation at both metal absorption edges[54].

In summary, surface science techniques tremendously contribute to the ORR mechanism investigations, each technique has its own unique detection characteristics and should be applied accordingly for different targets, while further development are necessarily considered to facilitate the *in-situ* characterizations. For example, high speed and high-resolution methods should be developed to avoid negative effect of traditional characterization like beam damages. In addition, the modification of *in-situ* cells to coupling multi-functional structure investigation is necessary to offer more information about the intermediate structure.

1.6.2 XAFS principles

Among various surface science techniques for *in-situ* catalyst structure investigation, X-ray absorption fine structure (XAFS) is one of the most powerful surface sensitive techniques to coupling the function of geometric and electronic structure investigation as well as the interaction study between the metals and surface adsorbates at atomic scales, which is element-specific and possess a high sensitivity. The incident X-rays with a certain high energy E go through the sample, where partial photons are absorbed by atoms in the sample and further lead to ejection of inner electrons to higher energy levels. In other word, XAFS is a measurement of the absorption coefficient of a sample, which is determined by the decay of incident X-ray intensity I_0 with a sample thickness of t. The relationship between the incident and transmitted intensity I_t can be expressed by,

$$A = \frac{I_t}{I_0} = \exp(-\mu t)$$

(1-5)

where A is the absorption coefficient, this item can be plotted as a function of incident X-ray energy E. With the increasement of photon energy, the spectrum shows sharp rises which is called absorption edges as shown in Figure 1-7. Different atoms possess characteristic absorption edge positions in XAFS measurement, which is the origin for element-specific property.

The XAFS spectrum can be divided into two distinct portions, X-ray Absorption Near Edge Structure (XANES) and Extended X-ray Absorption Fine Structure, as shown in Figure 1-8. XANES reveals the electronic configuration and symmetry of the central atom, providing information on the state of electrons. It usually arises from the pre-edge part and extended to 20 eV or 30 eV after absorption edge. This process can be described as: the X-ray with energy of $h\nu$ incidents on the target atom which has an electron with binding energy of E_b, the absorption taken place once $h\nu \geq E_b$. The left energy is transferred to the electrons located at lower energy level. The excited electron with kinetic energy $E_k = h\nu - E_b$ at lower energy level leave the original lower energy position. Therefore, electrons transition occurs from lower atomic levels to higher levels, for example, in L_2 and L_3 edge observations, the transition is from $2p$-orbital to $5d$-orbital. The absorption edges reflect corresponding binding energies of all electrons within the atom. Usually, regulated by dipole allowed rule, the core electron transition from lower atomic energy to higher energy level results in sharp intensive peak immediately after edge jump. This characteristic peak is element-specific, the peak intensity reveals the occupancy of higher energy level. For transition element and L_3 edge, larger peak intensity means more empty state or higher valence. The resulted sharp peak is also called “whiteline” (WL) in many literatures.

EXAFS contains information on the structure around central atom, providing information on interatomic distance and coordination number. EXAFS occurred after XANES part, usually extend to higher energy side of XANES in range of 1 keV. In the XANES process, ejected electrons are transmitted to higher energy levels. As is well known that electrons have both particle and wave character, it is possible to describe the electron motion in space by wavefunctions. The ejected electron can be scattered back from a neighboring atom. Consequently, the outgoing wavefunction and scattered wavefunctions interfere. The difference in wavelength of emitted electron and scattered electron, distance between the ejected electron and the scattered electron and phase shift caused by scattering event can all lead to enhance or elimination between two wavefunctions and result in a total wavefunction in form of sine function. The resulted sin function reflects detailed local structure information on bond distance, coordination number and surrounding environment of absorbing atom.

As EXAFS indicates the local structure information of absorbing atoms, it is necessary to indicate how does EXAFS reflects structure parameters. Typically speaking, the wiggles increase with the number of surrounded atoms increases, the oscillation frequency and bond distance in adjacent layers have inversely relationship. The EXAFS function, $\chi(k)$, is extracted from the X-ray absorption spectrum by removing the background, which customarily express the signal as a function of the wave number.

EXAFS function $\chi(k)$ is the sum of the scattering contribution from all atoms in neighboring coordination shells, which can be expressed as following equation:

$$\chi(k) = S_0^2 \sum_i \frac{N_i F_i(k)}{k r_i^2} e^{-2k^2\sigma_i^2} \sin\left(2kr_i + \phi_i(k)\right)$$

(1-6)

$$k = \sqrt{\frac{2m}{\hbar^2}(E - E_0)}$$

(1-7)

where

$\chi(k)$ is the EXAFS function.

k is the wave number of the ejected electron.

$\mu(E)$ is the absorption coefficient

$\mu_s(E)$ is the smooth ingredients of $\mu(E)$

$\hbar$ is the reduced Planck's constant.

m is electron rest mass

i is the label of coordination shells around the absorbing atom.

r_i is the distance between the absorbing atom and atoms in the ith coordination shell.

$\phi_i(k)$ is the total phase shift of phase shift of the backscattering atom plus twice that of absorbing atom.

N_i is the coordination number of the atoms in the ith coordination shell.

S_0^2 is the amplitude reduction factor.

F_i is the back-scattering amplitude function.

λ is the inelastic mean free path of the electron.

σ^2 is the Debye Waller factor.

E_0 is the incident X-ray energy.

E is the absorption edge energy.

$\chi(k)$ oscillation is proportional to the coordination number N_i and S_0^2, and inversely proportional to the Debye Waller factor σ^2. The oscillation frequency is inversely proportional to the bond distance.

In short, local structure features are investigated from the process of ejected electron is scattered from the neighboring atoms around the absorption atom and the interferences occur between the outgoing and scattered electron wavefunctions.

1.7 Dissertation Targets

In summary, the above-mentioned techniques, especially the *in-situ* structure characterization methods enables the catalysts structure-activity relationship determination for ORR mechanism studies, which is essential for the development of advanced catalysts for PEMFCs. XAFS is the most suitable technique for *in-situ* structure investigation. However, further development for *in-situ* XAFS applied to model catalyst systems applying flat substrates, like HOPG and single crystals, is necessary to overcome the extremely challenging detection conditions, such as diluted system characterization and electrolyte appeared *in-situ* investigation. This dissertation is going to introduce three kinds of developed XAFS techniques: a bent crystal Laue analyzer assisted back illuminated / high energy resolution fluorescence detection X-ray absorption fine structure (BCLA+BI/HERFD-XAFS) (Chapter 3), BCLA enhanced polarization-dependent total reflection fluorescence XAFS (BCLA+PTRF-XAFS) technique (Chapter 4), and *in situ* electrochemical PTRF-XAFS (EC-PTRF-XAFS) technique (Chapter 5 and Chapter 6). These new XAFS

techniques are suitable for structure study of Pt-based model systems. Several new and important concepts for the *in-situ* XAFS measurement development of noble metal Pt-based ORR catalysts studies are discussed and I propose the final conclusions about merits and prospects of these newly developed interface XAFS methods.

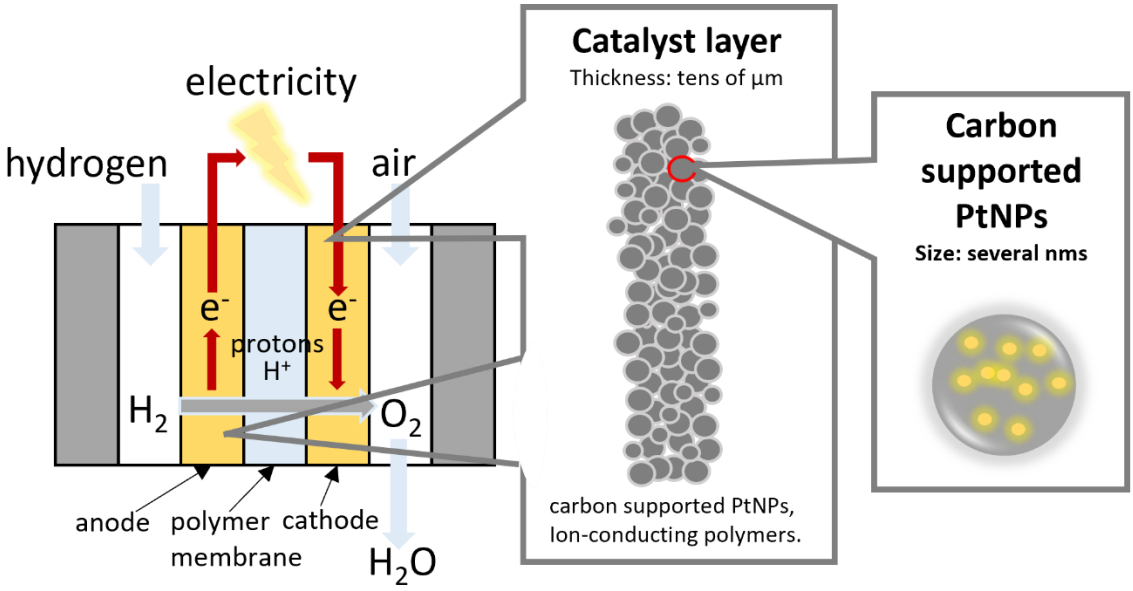

Figure 1-1. Schematic description for PEMFCs and catalyst applications in electrodes.

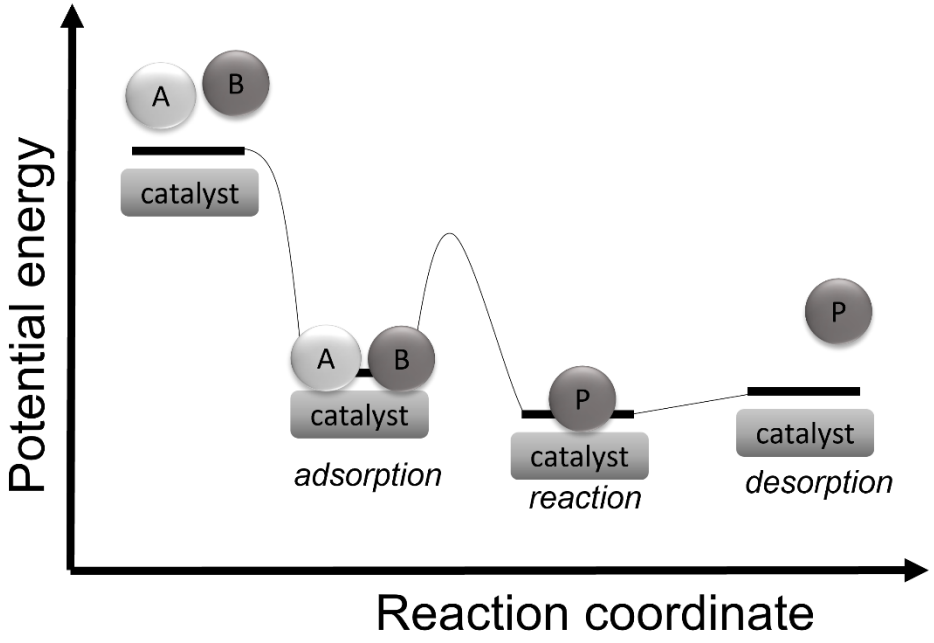

Figure 1-2. Catalysts favored chemical reactions.

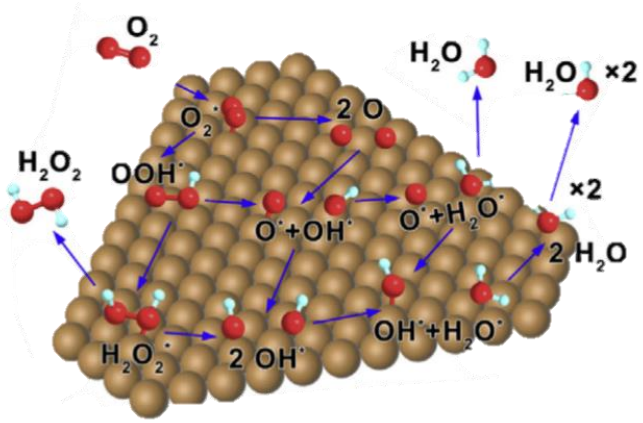

Figure 1-3. Schematic illustration of oxygen reduction reaction pathways and corresponding intermediates. [55]

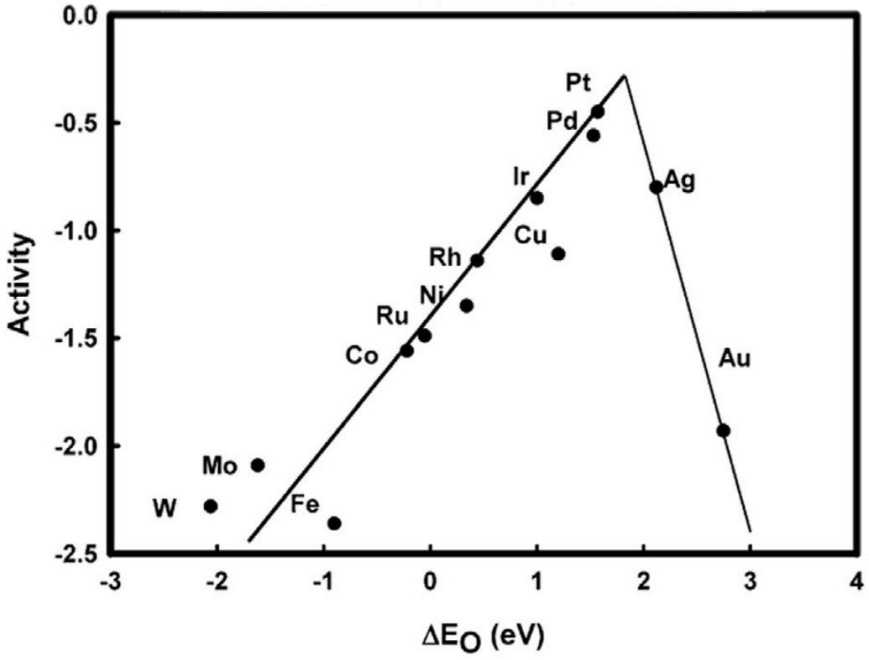

Figure 1-4. The relationship between ORR activity and oxygen-binding energy for various metals. [44]

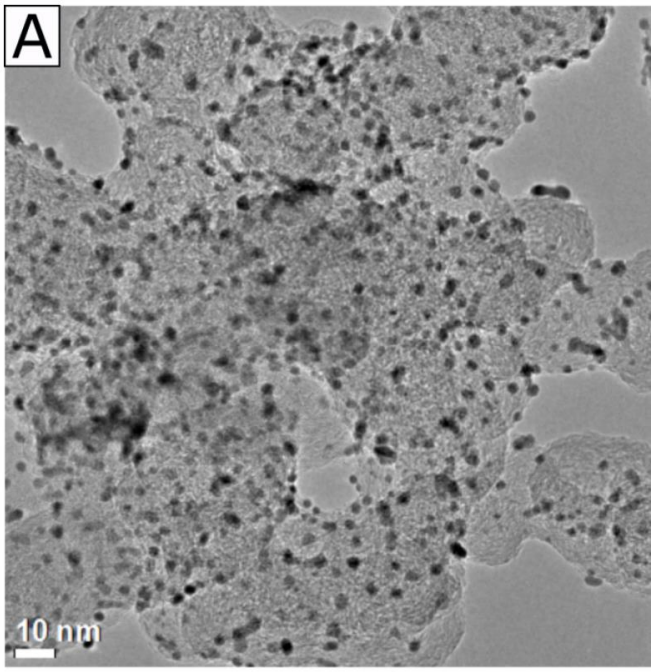

Figure 1-5. Bright-field TEM images of 20%wt platinum supported on carbon black (Pt/C 20%) with an average particle size of (2.6 ± 0.5) nm. [56]

Figure 1-6. Schematic diagram of the performance loss mechanism of Pt/C catalysts in ORR.

[29]

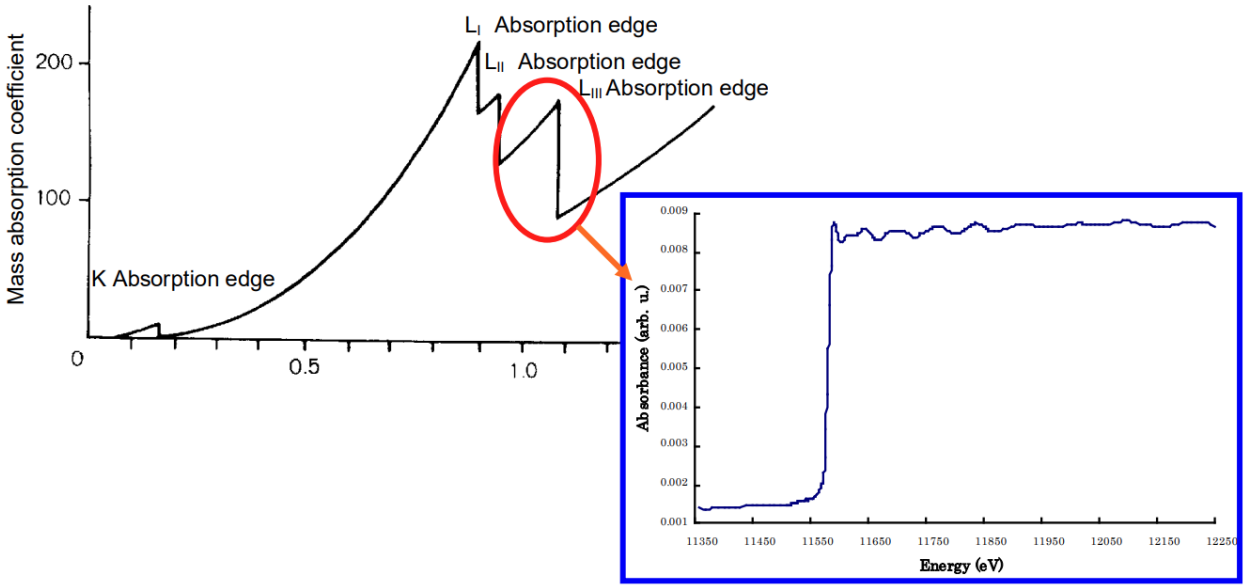

Figure 1-7. Absorption Coefficient Vs. X-Ray Wavelengths. The absorption coefficient that appears smooth in the left-hand graph shows complex ripples near the absorption edge in the right-hand graph.

Manual for XAFS Analysis Software Rex2000, Rigaku Corporation.

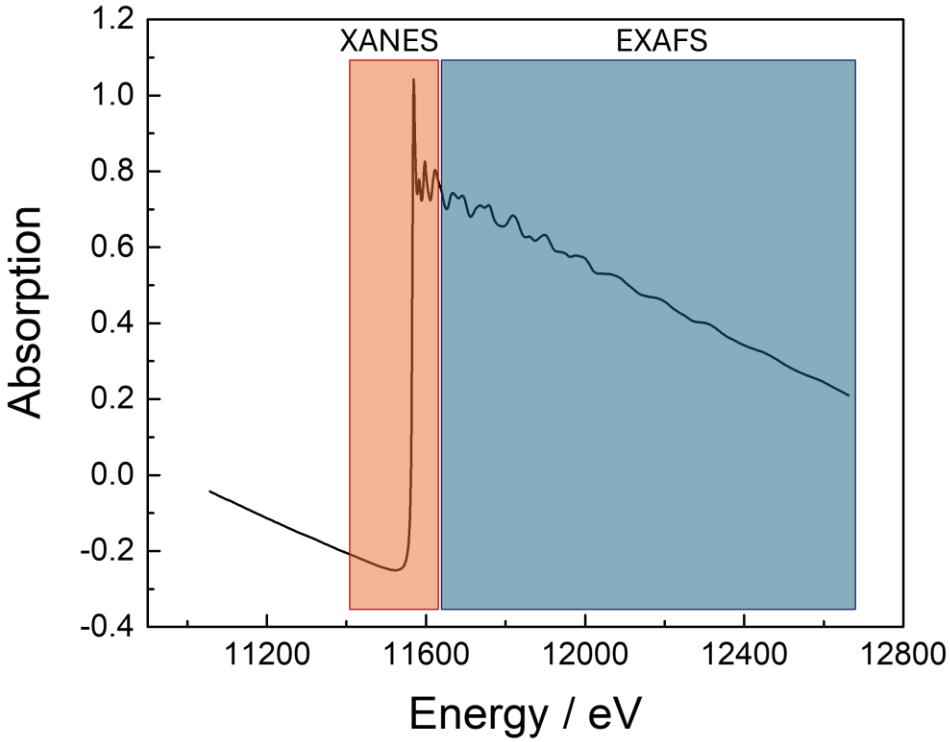

Figure 1-8. XAFS spectra at Pt L_3 edge.

Reference

[1] M.J. Stolarski, K. Warmiński, M. Krzyżaniak, E. Olba-Zięty, P. Stachowicz, Energy 204 (2020) 117952.

[2] K. Al-Shayji, E. Aleisa, Energy 158 (2018) 681–692.

[3] C. Fant, B. Boehlert, K. Strzepek, P. Larsen, A.E. White, S. Gulati, Y. Li, J. Martinich, Energy 195 (2020) 116899.

[4] I. Hanif, S.M.F. Raza, P. Gago-de-Santos, M. Alharthi, Q. Abbas, Energy 171 (2019) 493–501.

[5] M.A. Abdelkareem, M.E.H. Assad, M.E.H. Assad, E.T. Sayed, B. Soudan, Desalination 444 (2018) 178.

[6] A.G. Olabi, T. Wilberforce, M.A. Abdelkareem, Energy 214 (2020) 118955.

[7] S. Walch, A. Dhanda, M. Aryanpour, Heinz Pitsch, H. Pitsch, Journal of Physical Chemistry C 112 (2008) 8464–8475.

[8] J. H. Sinfelt, Surface Science 500 (2002) 923–946.

[9] G.A. Somorjai, B.E. Bent, Introduction to surface chemistry and catalysis, (1994).

[10] H.A. Gasteiger, S.S. Kocha, B. Sompalli, F.T. Wagner, Applied Catalysis B-Environmental 56 (2005) 9–35.

[11] N.M. Markovic, T.J. Schmidt, V.R. Stamenkovic, P.N. Ross, Fuel Cells 1 (2001) 105–116.

[12] N. Jung, D.Y. Chung, J. Ryu, S.J. Yoo, Y.-E. Sung, Nano Today 9 (2014) 433–456.

[13] M.K. Debe, Nature 486 (2012) 43–51.

[14] H.T. Chung, D.A. Cullen, D. Higgins, B.T. Sneed, E.F. Holby, K.L. More, P. Zelenay, Science 357 (2017) 479–484.

[15] I.E.L. Stephens, A.S. Bondarenko, U. Grønbjerg, J. Rossmeisl, I. Chorkendorff, Energy and Environmental Science 5 (2012) 6744–6762.

[16] N.M. Markovic, P.N. Ross, Surface Science Reports 45 (2002) 117–229.

[17] Y. Wang, H. Su, Y. He, L. Li, S. Zhu, H. F. Shen, H. Shen, P. Xie, X. Fu, G. Zhou, C. Feng, D. Zhao, F. Xiao, X. Zhu, Y. Zeng, M. Shao, S. Chen, G. Wu, J. Zeng, C. Wang, Chemical Reviews 120 (2020) 12217–12314.

[18] J.K. Nørskov, F. Abild-Pedersen, F. Studt, T. Bligaard, Proceedings of the National Academy of Sciences of the United States of America 108 (2011) 937–943.

[19] Y.-J. Wang, W. Long, X. Hu, L. Wang, L. Wang, R. Yuan, A. Ignaszak, B. Fang, D.P. Wilkinson, Energy and Environmental Science 11 (2018) 258–275.

[20] G. Wang, Z. Yang, Y. Du, Y. Yang, Y.S. Yang, Angewandte Chemie 58 (2019) 15848–15854.

[21] H. Yang, Z. Chen, S. Kou, G. Lu, D. Chen, Z. Liu, Journal of Materials Chemistry 9 (2021) 15919–15936.

[22] S. Sui, X. Wang, X. Zhou, Y. Su, S. Riffat, C. Liu, Journal of Materials Chemistry 5 (2017) 1808–1825.

[23] S. Patowary, R. Chetry, C. Goswami, B.Chutia, P. Bharali, Chemcatchem (2021).

[24] J. Lian, J.-Y. Zhao, X.-M. Wang, Acta Metallurgica Sinica (English Letters) 34 (2021) 885–899.

[25] N.R. Elezović, V. Radmilovic, N.V. Krstajić, RSC Advances 6 (2016) 6788–6801.

[26] J. Zhang, Y. Yuan, L. Gao, G. Zeng, M. Li, H. Huang, Advanced Materials 33 (2021) 2006494.

[27] T. Fuchs, J. Drnec, F. Calle-Vallejo, N. Stubb, D.J.S. Sandbeck, M. Ruge, S. Cherevko, D.A. Harrington, O.M. Magnussen, Nature Catalysis 3 (2020) 754–761.

[28] C.-Y. Ahn, J.-E. Park, J.E. Park, S. Kim, O.-H. Kim, W. Hwang, M. Her, S.Y. Kang, S. Park, O.J. Kwon, H.S. Park, Y.-H. Cho, Y.-E. Sung, Chemical Reviews (2021).

[29] Q. Sun, X.-H. Li, K.-X. Wang, T.-N. Ye, J.-S. Chen, Energy & Environmental Science 16 (2023) 1838–1869.

[30] A.U. Nilekar, Y. Xu, J. Zhang, M.B. Vukmirovic, K. Sasaki, R.R. Adzic, M. Mavrikakis, Topics in Catalysis 46 (2007) 276–284.

[31] V.R. Stamenkovic, B.S. Mun, Matthias Arenz, M. Arenz, K.J.J. Mayrhofer, C. Lucas, G. Wang, P.N. Ross, N.M. Markovic, Nature Materials 6 (2007) 241–247.

[32] B.-J. Hwang, S.M.S. Kumar, C.-H. Chen, Monalisa, M.-Y. Cheng, and D. Liu, J.-F. Lee, Journal of Physical Chemistry C 111 (2007) 15267–15276.

[33] J. Campos, Nature Reviews Chemistry 4 (2020) 696–702.

[34] Y. Wang, L. Cao, N.J. Libretto, X. Li, C. Li, Y. Wan, C. He, J. Lee, J.M. Gregg, H. Zong, D. Su, J.T. Miller, T. Mueller, C. Wang, C. Wang, Journal of the American Chemical Society 141 (2019) 16635–16642.

[35] J.R. Kitchin, J.K. Nørskov, M.A. Barteau, J.G. Chen, Physical Review Letters 93 (2004) 156801.

[36] M. Mavrikakis, B. Hammer, J.K. Nørskov, Physical Review Letters 81 (1998) 2819–2822.

[37] P. Wu, H. Liu, Y. Cao, S. Xi, Z. Li, Z. He, L. Song, J. Xu, P. Bai, L. Zhao, S. Mintova, Z. Yan, Microporous and Mesoporous Materials 316 (2021) 110982.

[38] S. Yin, Y. Shen, J. Zhang, H. Yin, X. Liu, Y. Ding, Applied Surface Science 545 (2021) 149042.

[39] L. Yuxin, L. Du, F. Kong, G. Han, Y. Gao, C. Du, P. Zuo, G. Yin, ACS Sustainable Chemistry & Engineering 8 (2020) 1295–1301.

[40] M. Oezaslan, F. Hasché, P. Strasser, Journal of Physical Chemistry Letters 4 (2013) 3273–3291.

[41] M. Li, Z. Zhao, T. Cheng, A. Fortunelli, C.-Y. Chen, R. Yu, Q. Zhang, L. Gu, B.V. Merinov, Z. Lin, E. Zhu, T.H. Yu, Q. Jia, J. Guo, L. Zhang, W.A. Goddard, Y. Huang, X. Duan, Science 354 (2016) 1414–1419.

[42] C.-T. Hsieh, J.-Y. Lin, J.-L. Wei, International Journal of Hydrogen Energy 34 (2009) 685–693.

[43] C. Chen, Y. Kang, Z. Huo, Z. Zhu, W. Huang, H.L. Xin, J. Snyder, D. Li, J.A. Herron, M. Mavrikakis, M. Chi, K.L. More, Y. Li, N.M. Markovic, G.A. Somorjai, P. Yang, V.R. Stamenkovic, Science 343 (2014) 1339–1343.

[44] J.K. Nørskov, J. Rossmeisl, A. Logadottir, L. Lindqvist, J.R. Kitchin, T. Bligaard, H. Jónsson, Journal of Physical Chemistry B 108 (2004) 17886–17892.

[45] P.L.J. Gunter, J.W. Niemantsverdriet, F.H. Ribeiro, G.A. Somorjai, Catalysis Reviews-Science and Engineering 39 (1997) 77–168.

[46] D.W. Goodman, Model studies in catalysis using surface science probes, Chemical Reviews 95 (1995) 523–536.

[47] J. Zhao, J. Lian, Z. Zhao, X. Wang, J. Zhang, Nano-Micro Letters 15 (2022).

[48] M. Escudero-Escribano, A.G. Pedersen, E.T. Ulrikkeholm, K.D. Jensen, M.H. Hansen, J. Rossmeisl, I.E.L. Stephens, I. Chorkendorff, Chemistry: A European Journal 24 (2018) 12280–12290.

[49] M. Gocyla, S. Kuehl, M. Shviro, H. Heyen, S. Selve, R.E. Dunin-Borkowski, M. Heggen, P. Strasser, Shape ACS Nano 12 (2018) 5306–5311.

[50] S. Dai, Y. Hou, M. Onoue, S. Zhang, W. Gao, , X. Yan, G.W. Graham, R. Wu, X. Pan, Nano Letters 17 (2017) 4683–4688.

[51] C. Hess, Chemical Society Reviews 50 (2021) 3519–3564.

[52] J.-C. Dong, X.-G. Zhang, V. Briega-Martos, X. Jin, J. Yang S. Chen, Z. Yang, D.-Y. Wu, J.M. Feliu, C.T. Williams, T. Zhang, Z.-Q. Tian, J.-F. Li, Nature Energy 4 (2019) 60–67.

[53] D. Friebel, D. Miller, C.P. O'Grady, T. Anniyev, J.R. Bargar, U. Bergmann, H. Ogasawara, K.T. Wikfeldt, L.G.M. Pettersson, A. Nilsson, Physical Chemistry Chemical Physics 13 (2011) 262–266.

[54] B.M. Gibbons, M. Wette, M.B. Stevens, R.C. Davis, S. Siahrostami, M.E. Kreider, A. Mehta, D. Higgins, B.M. Clemens, T.F. Jaramillo, Chemistry of Materials 32 (2020) 1819–1827.

[55] W. Zhang, J. Chang, Y. Yang, SusMat 3 (2023) 2–20.

[56] O. Holderer, M. Carmo, M. Shviro, W. Lehnert, Y. Noda, S. Koizumi, M.-S. Appavou, M. Appel, H. Frielinghaus, Materials 13 (2020) 1474.

CHAPTER 2 Experimental Methods

2.1 Construction of model catalyst systems

In order to have a detailed investigation of the relationship between structure and catalytic activity for ORR at atomic scales, the application of well-prepared model catalyst system with stable and recyclable substrates is necessary. In this work, HOPG and single crystal Au (111) are chosen as substrates for the monometallic and bimetallic Pt-based catalysts studies.

2.1.1 Monometallic Pt-based model catalyst system

[HOPG substrate treatment]

HOPG was chosen as the carbon support. The HOPG is a layered polycrystal, which surface includes multiple randomly placed atomic steps and make up for several layers. For research purposes, the HOPG is a superior material with low impurities and highly ordered flat surface. Freshly prepared HOPG samples can be obtained via pressing an adhesive tape to commercially purchased HOPG surface and peeling it off. Double-sided HOPG can be used from both sides and its property doesn't vary in depth.

[SPIN-COATING]

A monodispersed Pt NPs was then deposited on the flat HOPG by spin-coating method to ensure uniform depositions. This unique method has been tremendously applied for thin film depositions. A typical process includes depositing a small droplet of liquid materials onto the substrate center, and then the substrate rotate at a high speed. The liquids overcomes the centripetal acceleration and gives a thin and uniform film formed over substrate. The property of the final obtained film depends on several factors, such as surface tension, rotation speed, acceleration, and drying rate, etc. The practical process can be divided into several steps:

1. Dispense step: Two common methods of dispensing are usually applied, static dispense, and dynamic dispense. Static dispense deposit a droplet of solution on the substrate to cover the whole surface firstly, and then providing a high speed for sample rotation. However, in dynamic dispensation, the sample starts rotation before liquid deposition. This configuration leads to less waste of fluid material because it is not necessary to cover the overall surface.
2. Accelerate step: The next step is to speed up the rotation to a relatively high value to ensure the desired final thickness. The acceleration should be carefully controlled since the liquids are easily evaporated at the very first few seconds. The speed (rpm) affects the degree of centrifugal force applied to the liquids. The thickness of films greatly depends on applying centripetal force provided by spin speed. In general, higher spin speeds and longer spin time can make thinner films. In addition, during the acceleration and spin process, it is necessary to keep a stable air flow and minimize the turbulence above the sample because objective surrounding environment plays an essential role in coating process.
3. Drying step: This process is crucial since the long drying time may increase physical stability before other handling processes.

2.1.2 Bimetallic Pt-based model catalyst system

[Au (111) single crystal treatment]

Au (111) single crystal was chosen as the substrate. The noble metal deposition on single crystals is highly affected by the substrate quality. Therefore, repeated used Au (111) should be carefully treated before every experimental. Firstly, to obtain a Pt-free surface, the sample was mechanically polished using diamond suspension polycrystalline black (Sankei, Japan) from 3 μm, 1 μm down to 0.01 μm and MasterTex Polishing Cloths (Buehler, USA). The sample should be washed

thoroughly by 18 MΩ ultrapure water after each polishing. The polished sample was sent to the furnace annealing at 900 ℃ under Ar (>99.999 vol.%, AIR WATER INC.) atmosphere instead of sending to electropolishing directly, to avoid the severe roughing of the surface. Then, partially recovered Au (111) substrate was send for electropolishing in 0.1 M $HClO_4$ + 5 mM NaCl at current density of 0.05 μA cm^{-2} over 2 days. The electropolishing (EP) can make the intrinsic terrace of Au (111) wider. Finally, the roughed Au (111) sample was sent to furnace annealing at 900 ℃ under Ar atmosphere for 12 hours. Furnace annealing is necessary to remove reductant Au atoms or particles aggregated near the kink positions, which is formed during EP, providing a flatter surface for metal depositions. The flame annealing by butane gas is necessary to recover the ordered structure before every deposition experiment. The surface quality is checked by AFM and CV in 50 mM H_2SO_4 before deposition experiments. Specific treatment procedures should be repeated according to the surface quality.

[Facile Electrochemical Methods for Pt-based Model Catalyst System]

Electrochemical methods are applied for noble metal depositions, underpotential deposition (UPD) and surface limited redox replacement (SLRR) reactions.

[[Underpotential deposition]]

Underpotential deposition reveals the process of a foreigner metal M, deposited on a metal substrate M' at potentials positive than the Nernst potentials of the corresponding M/M^{n+}, which is usually several hundred millivolts positive to the reversible potential for the bulk metal deposition. In the meanwhile, the strong interaction between adsorbed adatom of M and substrate M' should be stronger than M and itself, which ensures ML deposition of M. This process can be expressed as:

$$M^{n+} + \gamma_{UPD} e(S) \rightleftharpoons M^{(n-\gamma_{UPD})^+}(S)$$

(2-1)

Where S is the substrate, and γ_{UPD} is the electrosorption valency. The latter describes the charge flow during the process at the constant applied potential. Considering electrosorption valency is ranged between zero and ionic charge n, when the electrosorption valency is close to the n, completely discharge is expected for adsorbed species. While when the value is lower than the n, which indicates the adsorption with partial charge transfer.

The thermodynamic equilibrium for the metal deposition process with considering the activity of the reductant to be constant and set to unity can be expressed by Nernst equation as follows,

$$E_{M^{m+}/M} = E^0 + \frac{RT}{mF}\ln[a_{M^{m+}}]$$

(2-2)

Where E^0 is the standard equilibrium potential, R is the gas constant, n is the ion valence state, F is the Faraday's constant, and $a_{M^{n+}}$ denotes the activity of the metal ion. However, at the charge transfer equilibrium of a metal deposition in the underpotential range, the activity of the subML reductant should give less than unity values and is varied with the surface coverage (θ) accordingly. Consequently, the activity for sub ML reductant is defined as:

$$a_{ML} = f_M\theta(0 \le \theta \le 1)$$

(2-3)

$$a_{ML} = f_M = 1(\theta \ge 1)$$

(2-4)

Thus, the standard ML equilibrium potential E_{ML} can be obtained by

$$E_{M^{m+}/M}(\theta)_{ML} = E^0 + \frac{RT}{nF}\ln\left[\frac{f_{M^{m+}}c_{M^{m+}}}{f_M\theta}\right]$$

(2-5)

Where the $f_{M^{m+}}$and f_M represent the activity coefficient for the metal ions and metallic metals, respectively, and $c_{M^{m+}}$ is the concentration of metal ions. This equation gives an equilibrium potential, which is always more positive than the corresponding bulk deposition process derived from Nernst equation.

The UPD process perfectly controls the ML structure through the applied potentials and electrolyte compositions. The properties of UPD peaks, for example, peak positions, peak intensity and the number of peaks included in the CV or LSV processes directly reveal the deposition process details, which greatly depend on the substrate nature, the ratio between the diameter of the adsorbate species and the distance of two adjacent adsorption sites, degree of UPD coverage, and electrolyte components. [1]

[[Surface limited redox replacement reaction]]

The deposition of noble metals is of great interest in the ORR while the expensive approaches and setups as well as specifically developed logistics for deposition routines are required in conventional ultrahigh vacuum (UHV) deposition. In addition, electrochemical methods of overpotential deposition usually led to non-uniform surface morphologies. Therefore, it is necessary to develop an alternative approach with simplified deposition protocols and cost-effective properties to obtain smooth, uniform, and continuous homoepitaxial Pt metal layer. The SLRR has drawn great attention because of its outstanding layer by layer growth morphology and precise growth control without any electricity applied. This is a unique technique that requires a pre-formed sacrificial layer, utilizing the nobility difference between the UPD layer and metal of

interest to drive the galvanic displacement of the pre-deposited sacrificial metal layer by the target metal ions[2]. The irreversible experimental process can be presented as:

$$(\theta_M \cdot \rho_M) M^0_{UPD}/S(h,k,l) + (\theta_M \cdot \rho_M)\left(\frac{m}{p}\right) P^{p+}_{solv}$$

$$\Rightarrow\ (\theta_M \cdot \rho_M) M^{m+}_{solv} + (\theta_M \cdot \rho_M)\left(\frac{m}{p}\right) P^0_s/S(h,k,l)$$

(2-6)

where M is the pre-deposited metallic UPD metal species, P is the noble metal ion with valence state of P^{p+}. S is the well-defined supporting substrate, where single crystals are usually applied. ρ represents the packing density factor, which indicate the number of M atoms per one substrate atom. θ represents the coverage of UPD layer. After replacement reaction, the reactant is usually consisted of oxidized sacrificial metal with valence state of m^+, and reduced noble metal. Subscripts s and $solv$ represents the physical state of the metal (s = deposited metallic phase, $solv$ = solution phase). The precise amount of target metal is determined by reaction stoichiometry, structure, and coverage of UPD layer before SLRR starts. For example, in case of Ag growth (p=1) by SLRR of a full Pb UPD layer (m=2), where $\rho_{Pb} \approx 0.65$. Consequently, 1.3 ML Ag is expected to be obtained in one UPD + SLRR cycle[3,4]. This growth process is schematically presented in Figure 2-1.

The driving force for this spontaneous process is the difference (ΔU) between the equilibrium potential ($\Delta E_{P^{p+}/P}$) of the noble metal P in contact with its metal ions and the equilibrium potential ($\Delta E^{\theta\to 0}_{\frac{M^{m+}}{M}}$) of the UPD metal adlayer M, this relationship can be expressed by:

$$\Delta U = \Delta E_{P^{p+}/P} - \Delta E^{\theta\to 0}_{\frac{M^{m+}}{M}} > 0$$

(2-7)

Where the $\Delta E_{\frac{M}{M}}^{\theta \to 0}$ represents the equilibrium potential of a UPD layer at the most positive limit where UPD metal coverage approaches 0[5].

For SLRR, the rate equation can be defined as change of the surface concentration of UPD metal M ($dC_{M_{UPD}}$) in unit time (dt):

$$r_{SLRR} = -\frac{dC_{M_{UPD}}}{dt}$$

(2-8)

Considering the limiting step in the SLRR process, the determined step is either transportation of noble metal ions from bulk solution to electrode surface process, or diffusion of noble mental ions process. Therefore, the overall expression of Equation (2-8) can be altered into a more precise way according to the different determining parameters.

Zero ordered reaction kinetics

When the limiting step is transportation of noble metal ions from bulk electrolyte to the electrode surface, which can be termed as transport limited redox replacement (TLRR), the rate of SLRR can be described as the flux of the approaching noble ions to the electrode surface, the rate can be expressed by:

$$r_{SLRR} = -\frac{dC_{M_{UPD}}}{dt} = \left(\frac{m}{p}\right) \cdot \frac{D_{P^{p+}} \cdot \Delta C_{P^{p+}}^{\infty}}{\delta}$$

(2-9)

Where $D_{P^{p+}}$ represents the diffusion coefficient of noble metal P^{p+} ions, $\Delta C_{P^{p+}}^{\infty}$ is the P^{p+} ions concentration difference between the bulk solution and electrode surface, δ is the thickness of diffusion layer. Considering the transport limiting condition, the concentration of P^{p+} ions approaches 0, in other words, the rate is determined by concentration of P^{p+} ions in bulk solution. In this realm, the $\Delta C_{P^{p+}}^{\infty} \approx C_{P^{p+}}^{\infty}$= constant. In addition, the surface concentration of UPD metal M at any time equals to the product of the starting surface concentration of UPD metal M at t = 0 (Γ_i^{UPD}[mol cm^{-2}]) multiplied by coverage of the remaining UPD ML (θ_{UPD})at a specific time. In this case, it is interesting to find that the right side of the above equation has no coverage dependent feature, it is only determined by experimental conditions, which means the right-side item equals constant and consequently can be replaced with a new constant k_0,

$$k_0 = -\frac{d\theta_{UPD}}{dt} = \left(\frac{m}{p}\right) \cdot \frac{D_{P^{p+}} \cdot C_{P^{p+}}^{\infty}}{\Gamma_i^{UPD} \cdot \delta} \tag{2-10}$$

where the k_0 possess the unit of [s^{-1}].

First and Nth ordered reaction kinetics

When the diffusion flux of noble metal P^{p+} ions limit the reaction, the reaction kinetics can be expressed as follows:

$$-\frac{dC_{M_{UPD}}}{dt} = k \cdot (C_{M_{UPD}})^N \cdot \left(C_{P^{p+}}^i\right)^L \tag{2-11}$$

Where $C_{P^{p+}}^i$ is the concentration of noble metal P^{p+} ions at the electrode surface, N and L represent the reaction order for surface concentration from aspect of M adatoms and P^{p+} ions,

respectively. The rate constant k is the fundamental rate constant of SLRR process, which equals to $k = Z \cdot \exp\left(-\frac{E_a}{RT}\right)$, where Z is the collision frequency between P^{p+} ions and UPD adatoms, $E_a$is the activation energy of redox replacement reaction.

The rate equation can be further expressed by introducing a new constant $k' = k(C^i_{P^{p+}})^L$,

reaction rate constant k' can be introduced to give a simplified expression:

$$-\frac{dC_{M_{UPD}}}{dt} = k'(C_{M_{UPD}})^N \tag{2-12}$$

As $(C_{M_{UPD}})^N = \Gamma_i^{UPD}\theta_{UPD}$, the new constant k'' can be defined as $k'' = k'(\Gamma_i^{UPD})^{N-1} = k(C^i_{P^{p+}})^L(\Gamma_i^{UPD})^{N-1}$. In this realm, the surface coverage could be expressed by:

$$\theta_{UPD} = (1 + K \cdot t)^{\frac{1}{1-N}} \tag{2-13}$$

Where K is the reaction rate constant, $K = k''(N-1)$, possess the unit of $[s^{-1}]$. Note that this equation is not applied to situations when $N = 0$ and $N = 1$.

In case of 1st order reaction kinetics in terms of θ_{UPD},

$$\theta_{UPD} = \exp(-k''t) \tag{2-14}$$

the above Equation (2-14) and (2-15) are used to simulate the experimentally obtained open circuit potential transients.

2.2 Construction of *in-situ* XAFS systems

2.2.1 Conventional XAFS measurements

[Transmission mode and Fluorescence mode]

The most frequently used XAFS measurement methods are transmission mode and fluorescence mode. As introduced in Equation (1-5), the transmission mode measures the incident X-ray intensity (I_0) and transmitted X-ray intensity (I_t) by ion chambers. At most X-ray energies, the absorption coefficient is a function of energy, which greatly depends on several parameters as expressed by:

$$\mu \approx \frac{\rho Z^4}{AE^3} \tag{2-15}$$

Due to the strong dependence of absorption coefficient on Z, different atoms may have very different values, varied in several orders of magnitude. Figure 2-2 shows the energy-dependence of μ/ρ for O, Fe, Cd, and Pb. This method works well with standard foils and typical supported catalysts with metal loading of about 1 wt % or more.

In case of the target elements within sample is in a very low concentration, usually lower than ppm level, fluorescence detection is more advantageous. In typical fluorescence mode, the X-rays emitted from the sample include the fluorescence line of interest, fluorescence lines from other elements in the sample, as well as the elastic scatterings and inelastic scattered X-rays. Figure 2-3 shows a typical fluorescence spectrum for Fe K_α and K_β fluorescence lines along with the scattered peak. To improve the target fluorescence signal yield, suppressing the scatter peak and other fluorescence lines and only collecting the intensity of interest is crucial. Energy

discrimination via either physically removed by filtering out blocking emissions before detection or electronically after it is detected is necessary. For example, the practical use of "Z-1" filter can effectively absorb most of the scatter peak and improve the signal-to-background (S/B) level.

However, the filter itself would also emit undesired scattering signals at the same time. Therefore, a set of *Soller* slits equipped after filter and before detector can perfectly solve this problem. Figure 2-4 shows the schematic picture of fluorescence detection with filter and *Soller* slits sets. In addition, suitable detector with high energy resolution around 200 eV or better, like solid state Si or Ge detector can measure the full X-ray fluorescence spectra, which is able to identify and quantify the concentration of other elements in the sample and effectively reject the undesired portion of the fluorescence spectra.

Figure 2-5 shows the schematic of transmission mode measurement. Synchrotron radiation provides a wide range of X-ray energies, monochromators are necessarily applied to extract the desired energy range. Single crystal mirrors are used to focus the X-ray beams. Finally, the X-ray go through the ion chamber before the sample, go through and absorbed by sample, and go through ion chamber after the sample, respectively, I_0 and I are measured at the same time.

Figure 2-6 shows the schematic of fluorescence mode measurement. The X-ray incidents in the sample similar to that in transmission until the measurement of I_0. Then, the X-ray goes through or absorbed by the sample. Finally, the intensity of fluorescence X-ray which comes from sample is measured as I_f. The detector is usually placed perpendicular to the direction of incident X-ray. The absorption coefficient in fluorescence mode is approximated as:

$$\mu t = \frac{I_f}{I_0}$$

(2-16)

[Beamline Configuration]

A typical beamline is arranged as Figure 2-7.

The synchrotron radiation facilities provide X-ray source, where the electrons are accelerated by electromagnetic fields to reach the speed of light. The X-ray is generated when the electron beams are bent by the bending magnet. In this dissertation, the experiment was carried out in SPring-8 and Photon Factory (High Energy Accelerators Research Organization, Tsukuba).

The generated white X-ray which covers a wide range of energy need to be selected accordingly by using monochromators, where single crystals are frequently used. According to the Bragg's law, the angle of incidence θ_B is decided by:

$$2dsin\theta_B = n\lambda$$

(2-17)

where d[Å] is the lattice spacing, λ[Å] is the wavelength of incident X-ray. The wavelength is further determined by:

$$\lambda = \frac{hc}{E} = \frac{12398.52}{E}$$

(2-18)

Where is h the Planck constant, c is the speed of light, the E is the incident X-ray energy.

A parallel double crystal monochromator is widely applied to increase the intensity of X-rays, where silicon single crystal is mostly applied in monochromators. The energy resolution of a monochromator depends on the characteristic of monochromator. Si(111) is used for normal XAFS

measurement. However, if higher energy resolution are needed, Si(220) or Si(311) with higher reflection order are applied.

X-ray is focused using mirrors. The critical angle of total reflection is defined as:

$$\theta_c = (\frac{r_0 N_A Z \rho}{\pi A})^{1/2} \lambda \tag{2-19}$$

where r_0 is the radius of an electron, N_A is the Avogadro's constant, Z is the number of elements of material on mirror, ρ is the density of material, and A is the molar mass. The critical angle is given in unit of mrad. For high energy X-rays that cannot satisfy the above equation is removed.

Ionization chambers are used for detection of X-ray intensities. In transmission mode, the X-ray go through the ionization chamber to ionize the filling gas. Within ionization chamber, a strong electric field exists between the electrodes, the traveling ionized gas and electrons can be captured by electrodes. Therefore, X-rays are counted as the current at the electrodes and further amplified by the amplifier to give voltage as the output. Finally, the signal is converted to the pulses by Voltage to Frequency (V/F) converter and counted by the counter. The filling gas and high voltage application are important for ionization chambers. In fluorescence mode, the scintillation counter is used for fluorescence X-rays detection. When the ionization radiation travels through the scintillator, sparks are generated and amplified by the photomultiplier or the phototube. Scintillators counter doesn't have the energy resolution, all the signals including background arising from scattered X-rays are detected. Therefore, filters and *Soller* slits are necessary to be equipped with to remove the undesired signals.

2.2.2 Developments in the in-situ BCLA+BI/HERFD-XAFS apparatus

For traditional XAFS methodology such as transmission mode and fluorescence mode used for powder catalyst characterizations, the obtained structure information is usually averaged structure, not exact detailed local structures. In addition, those modes are not easy to be applied under the *in-situ* characterization within electrolyte because of severe scatterings coming from solution which deteriorate the signal to the background (S/B) ratio, as well as the weak XAFS signals because of limited surface area when applying to the well-defined flat surfaces.

For structure investigation of flat HOPG supported Pt ML model catalyst system, a back-illuminated (BI)-XAFS method was developed to meet the measurement requirements under *in-situ* conditions within electrolyte as shown in Figure 2-8. In this method, HOPG is used as an X-ray window as well as a substrate for Pt NPs. The X-ray travels through the HOPG window, which is thin enough and composed of a low Z element (carbon) so that the X-ray absorption by the incident window is small. This configuration allows the HOPG sample irradiation from the backside. Thus, no X-rays are absorbed by the electrolyte that is present in front of the surface. The Pt L_3 edge fluorescence signals passing through the HOPG window can be collected for further analysis. Nevertheless, elastic X-ray scattering from the liquid is not negligible. The incident X-rays can penetrate the solution and create the scattered X-rays from the solution, which are much stronger than the fluorescence XAFS signals and hinders the latter to deteriorates S/B[6]. The energy difference between elastic scatterings and fluorescence X-rays is about 2000 eV at the Pt L_3 edge. A solid-state detector (SSD) or silicon drift detector (SDD) possesses enough energy resolution to separate two types of X-rays, but the counting loss of the detectors becomes a serious problem when strong elastic scattering X-rays are detected. Thus, it is necessary to separate the fluorescence X-rays from the scattering X-rays in other ways. One way is to use a crystal

monochromator that can effectively separate the fluorescence signal from the elastic scattering X-rays signal because a crystal monochromator does not have a counting loss issue. Here, two types of monochromators were used to select the Pt fluorescence signals from scattering X-rays arising from electrolytes. The first one is the bent crystal *laue* analyzer (BCLA). The second one is a Bragg type bent crystal analyzer using a Johann or Johansson type monochromator. In the BCLA, a thin single Si(100) crystal is bent in a log spiral manner where all lines from the focal points cross the log spiral surface with a constant angle. This angle is set to the Bragg angle specific to the fluorescence X-rays energy so that only the fluorescence X-rays are diffracted and selected by the *Soller* slits[7]. The energy resolution of BCLA is usually a few tens electron volts (eV), which is larger than the L_3 edge life-time energy broadening. Consequently, XAFS signals obtained in the fluorescence mode should be compatible to that in the transmission mode, and XAFS spectra measured in the conventional transmission mode can be used as a reference. On the other hand, the second Bragg type bent crystal analyzer has a high energy resolution of about 1 eV. The energy resolution is good enough to obtain a higher energy resolution spectrum than conventional transmission XAFS[8]. In particular, a clearer and sharper fine structure can be obtained in the X-ray absorption near edge (XANES) region. This method is called high energy resolution fluorescence detection (HERFD) XANES.

2.2.3 Developments in the in-situ PTRF-XAFS apparatus

To precisely investigate the structure-activity relationship for Pt-based bimetallic catalyst systems, the application of *in-situ* electrochemical polarization dependent total reflection fluorescence XAFS (*in-situ* EC-PTRF-XAFS) method for Pt_{subML}/Au(111) model catalyst system is introduced, which is surface sensitive and suitable for structure investigation with low concentrations (as low as 10^{13} atoms/cm^2) of target elements. For Pt_{subML}/Au (111) structure investigation with a thin

solution layer appears condition, the fluorescence mode effectively increases the sensitivity of XAFS measurements. The principle of PTRF-XAFS follows when the total reflection condition allows the X-ray penetrates only in tens of nanometers, which eliminates the affect from the Au bulk and scatterings from electrolyte to effectively improve S/B ratio. When the polarization vector is parallel to the sample surface (s-polarization), bonds parallel to the surface are investigated, while bonds perpendicular to the surface are investigated when the polarization vector is vertical to the surface (p-polarization). Figure 2-9 shows the schematic description for polarization dependent XAFS measurement. Polarization dependent feature can provide three-dimensional (3D) structure information as expressed by the following equations:

$$\chi_{obs}(k) = \sum_i 3cos^2\theta_i\chi_i(k) \text{ at K and } L_1 \text{ absorption edge} \quad (2\text{-}20)$$

$$\chi_{obs}(k) = \frac{1}{2}\sum_i(1.2 + 2.4\,cos^2\theta_i)\chi_i(k) \text{ at } L_2 \text{ and } L_3 \text{ absorption edge} \quad (2\text{-}21)$$

where $\chi_{obs}(k)$, θ_i, and $\chi_i(k)$ are the total EXAFS oscillation, the angle between the electric filed vector of the incident X-ray and the ith bonding direction, and partial EXAFS contribution from the ith bond, respectively, which is shown in the Figure 2-10.

2.3 XAFS analysis methods

2.3.1 Curve Fitting by REX2000

For typical XAFS analysis, the raw oscillation would be used for several steps processing: energy correction, background removal, normalization, Fourier transform and curve fitting procedures. Several parameters are modified accordingly in the curve fitting procedure, for example,

coordination numbers (CN), correction of the original kinetic energy zero (ΔE_0), bond distance (r), and Debye Waller factors (σ^2). In this dissertation, all curve fitting works were carried out by REX2000 (REX2000, Rigaku Co., Japan).

For data processing, the first step is to carry out the background removal and data normalization as follows:

$$\chi(k) = \frac{\mu - \mu_s}{\mu_0} = \frac{(\mu - \mu_{pre}) - \mu_{post}}{\mu_0} \tag{2-22}$$

where the μ_{pre}, μ_{post} and μ_0 are absorption coefficient for pre-edge region, post-edge region, and edge jump between the previous two items, respectively. In addition, $\mu_s = \mu_{pre} + \mu_{post}$. The background of pre-edge region is calculated using least-square approximation using Victoreen equation:

$$\mu_{pre}(\lambda) = C\lambda^3 - D\lambda^4 + A \tag{2-23}$$

A, C, and D are constant. The μ_{post} is estimated by smoothing the oscillatory part of the data using Spline smoothing method. The Cook-Sayers evaluation is used in here, which introduces three parameters for automatic background removal:

H_R: the residual background determined by average value of Fourier transform magnitude between 0.00 and 0.25 Å.

H_M: the height of main peak expressed by maximum value in the Fourier transform magnitude between 1.00 and 5.00 Å.

H_N: the height of noise expressed by the average value of Fourier transform magnitude between 9.00 and 10.00 Å.

where $H_R - H_N \geq 0.05\, H_M$ should be satisfied. In addition, if $H_N > 0.1H_M$ established, which means the noise level is quite high, then $H_R > 0.1H_M$ should be satisfied.

Figure 2-11 shows the background removal baselines.

For XANES analysis, the normalized spectra can be used for WL region comparison to study the electronic structure. REX2000 provides a quantitative analysis to determine the valence state. In this method, the XANES part was divided into a sum of absorption peak by a Gaussian distribution or Lorentz distribution and transmission to the continuous states by arctangent term, which are expressed in the following equations, respectively:

For absorption peak

$$A \cdot exp\left\{\frac{-2(E - E_w)^2}{W_w^2}\right\}(Gaussian\ Distribution) \tag{2-24}$$

$$(A/\pi) \cdot \frac{W_W}{4(E - E_W)^2 + W_w^2}(Lorentz\ Distribution) \tag{2-25}$$

where A, E, E_w and W_w are peak height, energy, absorption peak position, and peak width respectively.

For continuous state (arctangent term)

$$(B/\pi) \cdot tan^{-1}(E - E_w - \Delta E)$$

(2-26)

where B and ΔE represent continuity term height and continuity term offset respectively.

In peak separation analysis for each potential condition, continuous term is fixed, with only Gaussian distribution peak fitting parameters varied. Using the position, height, or the full width at the half maximum height (FWHM) of Gaussian or Lorentz peak, it is possible to predict the relationship between the valence state of target element and measurement conditions.

For EXAFS analysis, it is necessary to convert the oscillation from E space to k space according to the Equation (1-6), where k is in unit of Å^{-1}, E_0 is the X-ray incident energy, which is necessary to emit the core level electrons as a free photoelectron. In practical analysis, E_0 value is usually taking the position of inflection point of the absorption edge. Then, EXAFS oscillation is extracted by a spline smoothing method and normalized as introduced in XANES processing. k^n is selectively multiplied to the $\chi(k)$ oscillation to emphasize the signals at desired k regions, where $k = 0, 1, 2$ or 3. However, the noise might be enlarged at the same time. Thus, the choice of n should be carefully manipulated. The bond distance between the X-ray absorbing atom and the neighboring atoms are directly observed from the Fourier transform of $\chi(k)$ in k space. The sinusoidal-like EXAFS oscillation gives a pseudo-radial distribution function following:

$$FT = \int_{k_{min}}^{k_{max}} k^n \cdot \chi(k) \cdot w(k) \cdot e^{2ikr} dk$$

(2-27)

where $w(k)$ is the window function used for Fourier transform. k range should be as large as possible, where k_{min} usually starts from 2.0 ~ 3.0 Å^{-1} to avoid multiple scattering effect around absorption edge, k_{max} value should be carefully picked up to obtain large enough value on the one

hand and ensure the noise level should not be dominated in the high k region on the other hand. The Hanning window defined as following equation is used:

$$w = \left[1 - \frac{\cos\{\pi(k - k_{min})\}}{2d}\right], \qquad k_{min} < k < k_{min} + d$$

$$= 1, \qquad k_{min} + d < k < k_{max} - d$$

$$= \left[1 - \frac{\cos\{\pi(k_{min} - k)\}}{2d}\right], \qquad k_{max} - d < k < k_{max}$$

(2-28)

where d is preferred between 5 ~ 10 % of the whole Fourier transformed range.

Then, curve fitting is carried out to obtain fitting parameters by non-linear least square methods. Finally, the residual of EXAFS oscillation between the experimental data and calculated data is compared and the fitting degree is evaluated by R-factor as follows:

$$R\text{-}factor = \frac{\sum_i \{k^n \cdot \chi_{exp,i}(k) - k^n \cdot \chi_{cal,i}(k)\}^2}{\sum_i \{k^n \cdot \chi_{exp,i}(k)\}^2}$$

(2-29)

where the $\chi_{exp}(k)$ and $\chi_{cal}(k)$ are experimental EXAFS oscillations and calculated oscillations, respectively. Note that the R-factor was evaluated using the k-range chosen for Fourier transform. Minimum R-factor value is searched in CF analysis.

Though CF analysis is widely used in XAFS analysis, there's several nonnegligible limitations that arises from degree of freedom.

The degree of freedom is derived from Nyquist theory by:

$$M = \frac{2\Delta k \Delta r}{\pi} + \alpha \ (\alpha = 0, 1, 2)$$

(2-30)

Where Δk and Δr are the range for experimental data in Fourier transform and inverse Fourier transform. Degree of freedom determines how many parameters can be modified from an EXAFS spectrum. In other words, the number of fitting parameters cannot exceed this value. Otherwise, unreliable results are expected. To allow higher values in degree of freedom, one way is to extend the experimental k range in EXAFS measurement. However, EXAFS oscillation damps at higher k region, which can be explained by a. the item $1/k$ in the EXAFS equation (1-6); b. the scattering ability of the surrounding atom for the electron with high k wave numbers becomes small; c. the Debye Waller factor in EXAFS equation (1-6) is decided by thermal and static disorder. The former one is reduced by the low temperature measurement. The limitation of degree might also be a serious problem in complex *in-situ* XAFS systems, the poor quality of raw data greatly limit the number of free parameters.

2.3.2 Feff Simulation

Feff is a program that calculates EXAFS and XANES spectra by varying fitting parameters at a time, for example, Debye Waller factor, reduction factor (S_0^2), bond distance, etc. The calculated spectrum based on a certain known structure model is fitted to the experimental data, the fitting degree is usually evaluated by χ^2 test. To avoid confusion between the EXAFS oscillation $\chi(k)$ and χ^2 test, R^2 is used instead of χ^2 symbol.

$$R^2 = \frac{1}{N} \sum_i \frac{\chi_{\exp}(k_i) - \chi_{cal}(k_i)}{\varepsilon_i^2}$$

(2-31)

Where ε_i^2 is the error estimated from the experimental spectrum. A good model is expected when the R^2 approaches and lower than the unity at the same time.

2.3.3 Constrained Thorough Search Method

It should be noted that pursuing global minimum R-factor without thinking about the estimation of errors, correlations between the fitting parameters, or evaluation whole parameter space is meaningless. A more considerate analysis method called constrained thorough search (CTS) is applied to search every parameter space and pick up all candidates which can reproduce the experimental data well with their statistical probability[9] significant parameters are extracted from EXAFS spectrum and meaningful structures consistent with experimental or theoretical results are selected. If all local minimum of parameters are selected and evaluated, the arbitrariness which can be included by the selection of initial parameters should be removed. This method plays an essential role in analyzing complex systems.

2.4 Application of Typical Surface Science Techniques

The development of surface science techniques enables the investigation of catalyst surface studies at atomic level and establish the relationship between the surface properties and catalytic activities. Several typically used surface science techniques will be introduced as follows:

2.4.1 X-ray Photoelectron Spectroscopy

XPS is a surface sensitive technique, which is frequently used in the field of material science and catalysis. The property of surface sensitive makes it possible to be applied in qualitative and quantitative analysis of arbitrary phase. It qualitatively provides information on elemental composition and distinguish oxidation state for specific element, which is caused by chemical shift. For heterogeneous samples, it is also possible to calculate coverage of one phase over another

quantitatively. In most cases, XPS yields the surface consumption information in depth of 5 nm approximately.

The basic principle of XPS is based on photoelectron effect: when an atom is irradiated by soft X-ray (energies lower than ~ 6 keV) with energy of $h\nu$, the valence electron with binding energy of E_b with respect to the Fermi level is escaped and ejected with kinetic energy of E_k. Figure 2-12 shows the photoelectron ejection process, and this process can be expressed as follows:

$$E_b = h\nu - E_k - \varphi \tag{2-32}$$

where h is Planck constant, ν is the frequency of exciting radiation, φ is the working function of spectrometer, which depends on the sample environment and spectrometer working condition.

Routinely used X-ray sources are Al K_α (1486.3 eV) and Mg K_α (1253.6 eV). In XPS, the relationship between the photoelectron intensity versus kinetic energy of photoelectrons are measured, and then converted to the relationship between the photoelectron intensity and binding energy of photoelectrons. Binding energy are element- and orbital-specific. For the binding of energy of a specific element and specific orbital, it may differ because of chemical environment and bonding state.

For XPS sources, standard mode utilizing either Mg or Al source, or monochromator mode applying Al source are chosen accordingly. In monochromator mode, a quartz crystal placed at a specific angle to allow only Al K_α to diffract, other Al X-ray lines and bremsstrahlung radiation are filtered out. Figure 2-13 shows the schematic diagrams of major components of the monochromator. There are several advantages of using the monochromator. Firstly, the monochromator eliminates the undesired excitations arising from X-ray lines. For instance,

standard mode applying Mg source will irradiate Mg $K_{\alpha 3}$ line expect for the most intense Mg $K_{\alpha 1,2}$ lines. Consequently, additional peaks due to the excitation with multiple X-ray energies appear in the spectrum, termed as satellite peaks. This phenomenon can be avoided in monochromator mode. Figure 2-14 shows the shows the spectra of Ag investigated by standard mode and monochromator mode, respectively[10]. The second advantage is the X-ray linewidth reduced from 0.9 eV to 0.25 eV when applying monochromator. Figure 2-15 shows the different resolution for Ag 3d peak obtained via different X-ray sources. A higher resolution with smaller line width showed a smaller full width half maximum (FWHM).

2.4.2 Atomic Force Microscopy

AFM was applied for the purpose of acquiring sample surface images of both conductive and nonconductive samples in micro- and nanoscales, and even on atomic and molecular scales. The principle of AFM is to detect the force between the sample surface and the probe. The main components of AFM are a thin cantilever, a 3D piezo-electric scanner and an optical system to measure deflection of the cantilever. The thin cantilever has a very sharp probing tip, 1-10 nm in radius. These basic components are depicted in Figure 2-16.

The laser beam firstly comes from the diode and focused on the cantilever. When the tip approaches the surface, or contacting and tapping the surface, it is being affected by surface forces (attractive ones or repulsive ones). These forces drive the tip to bend continuously. In the meanwhile, the reflected laser beam from the cantilever goes to a mirror where laser beam is reflected and transported to a four-point photodetector. Any deflection coming from the laser beam as the sample is scanned (cantilever moves) is detected by photodetector. As a result, the photodetector produces signals because of deflections. Detected signals are recorded on the computer during scanning. Therefore, both lateral and vertical surface information can be obtained.

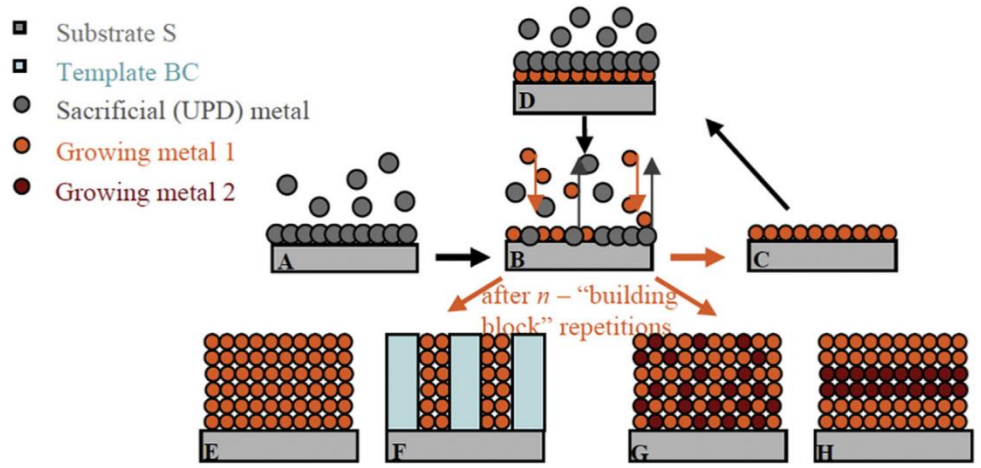

Figure 2-1. Schematic illustration of the growth strategy intended for different final structures resulting from growth based on SLRR reaction[3].

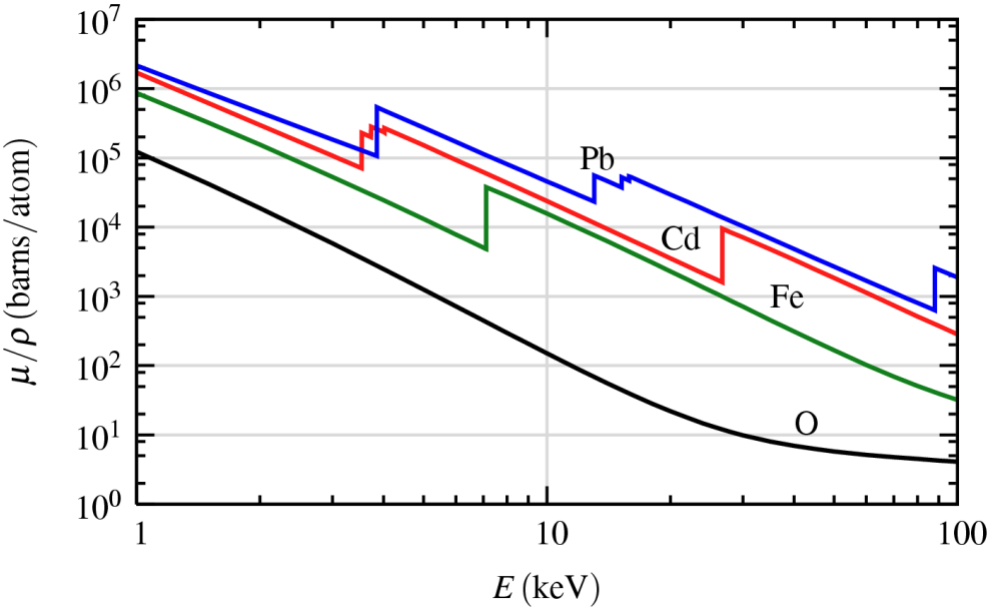

Figure 2-2. The absorption cross-section μ/ρ for several elements over the x-ray energy range of 1 to 100 keV. Notice that there are at least 5 orders of magnitude in variation in μ/ρ, and that in addition to the strong energy dependence, there are also sharp rises corresponding to the core-level binding energies of the atoms.

Newville, M. Fundamentals of XAFS. Consortium for Advanced Radiation Sources, University of Chicago (USA) [http://xafs. org] 2004, 78. https://doi.org/10.2138/rmg.2014.78.2.

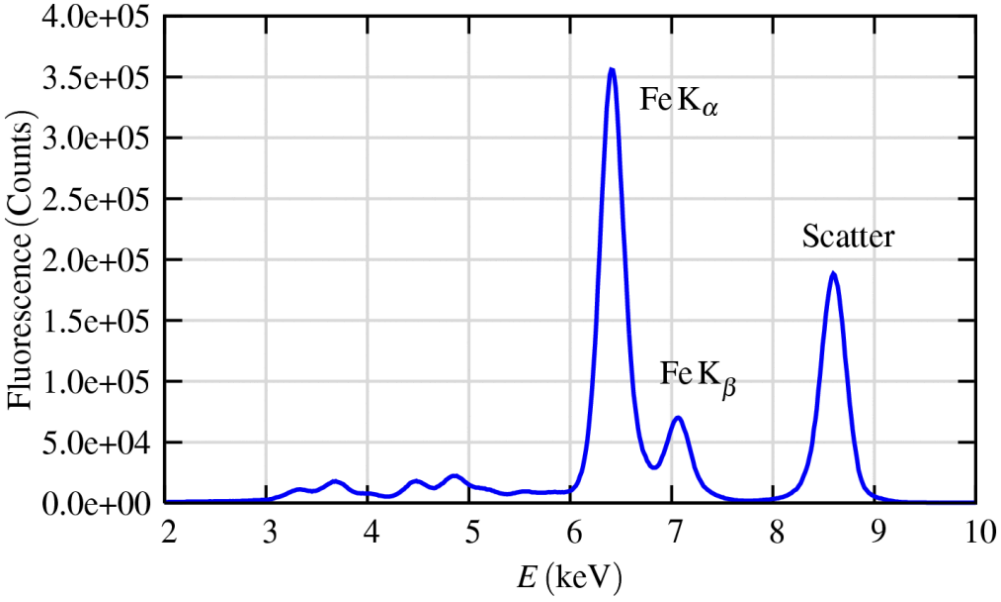

Figure 2-3. X-ray fluorescence spectra from an Fe-rich mineral (an olivine), showing the Fe Kα and Kβ emission lines, and the elastically (and nearly elastically) scattered peaks. At lower energies, Ca, Ti, and V peaks can be seen.

Newville, M. Fundamentals of XAFS. Consortium for Advanced Radiation Sources, University of Chicago (USA)[http://xafs. org] 2004, 78. https://doi.org/10.2138/rmg.2014.78.2.

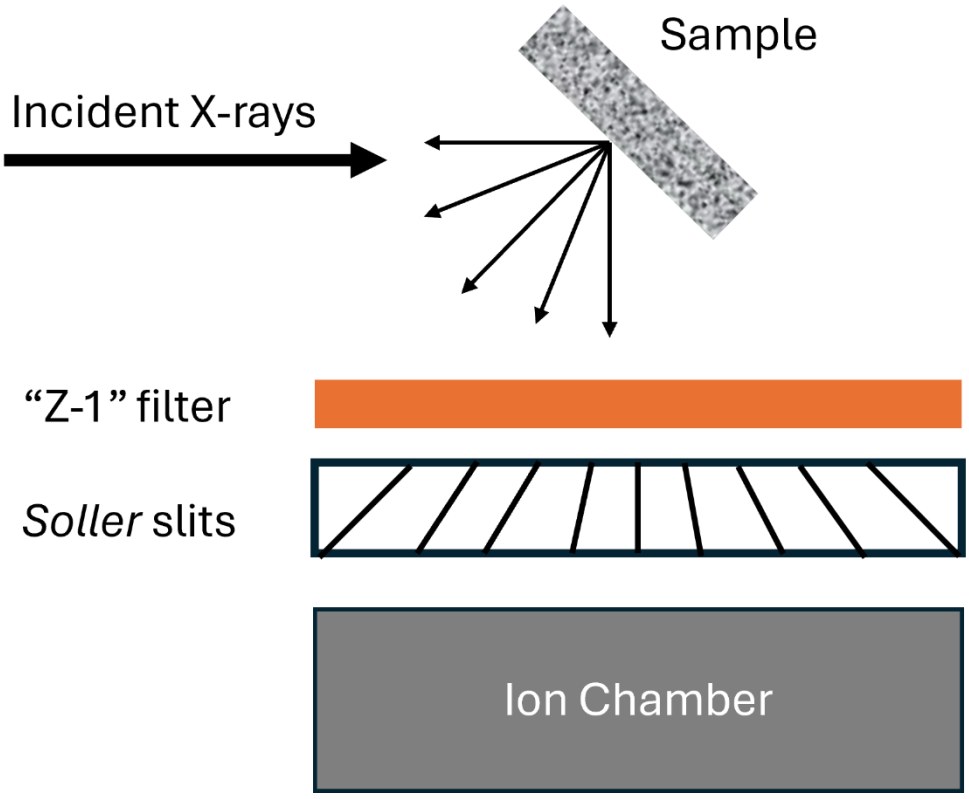

Figure 2-4. Fluorescence mode detection with application of filter and *Soller* slits.

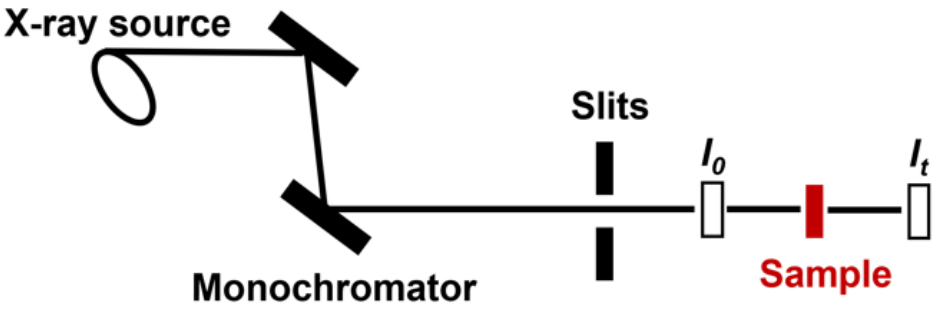

Figure 2-5. Transmission mode in XAFS measurement.

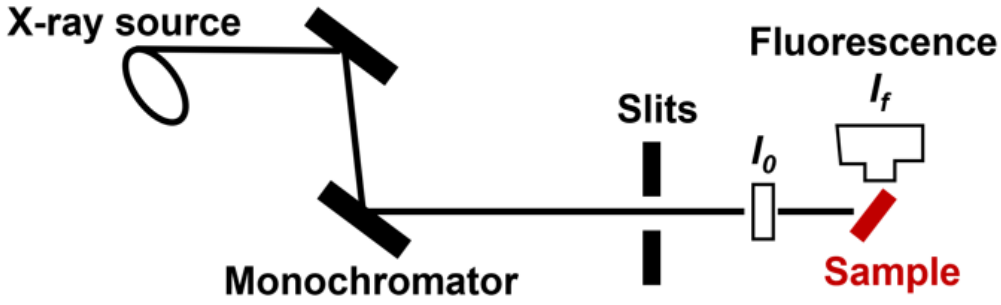

Figure 2-6. Fluorescence mode in XAFS measurement.

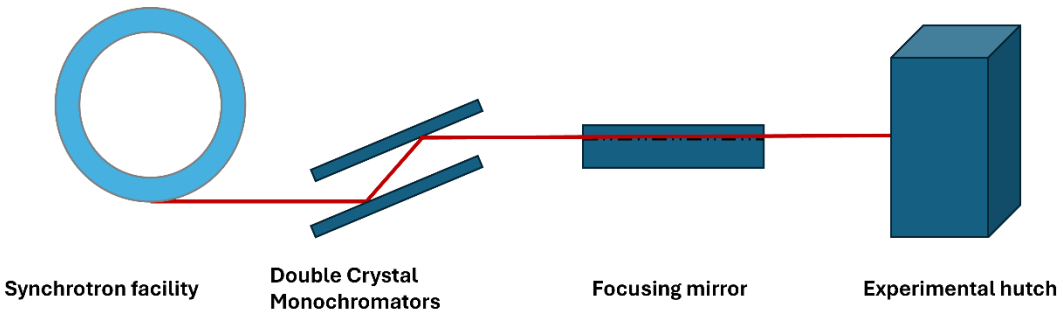

Figure 2-7. Beamline configurations

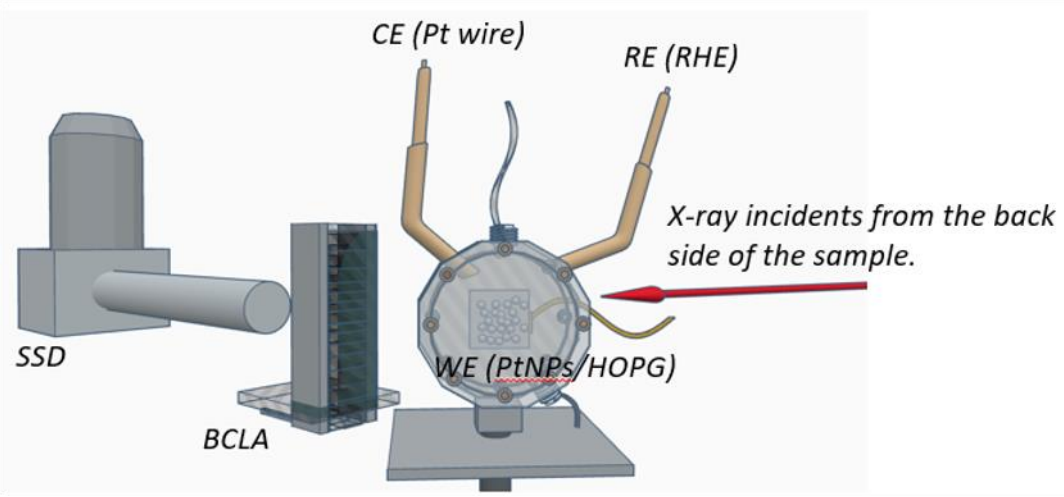

Figure 2-8. In-situ BCLA enhanced EC-BI-XAFS apparatus.

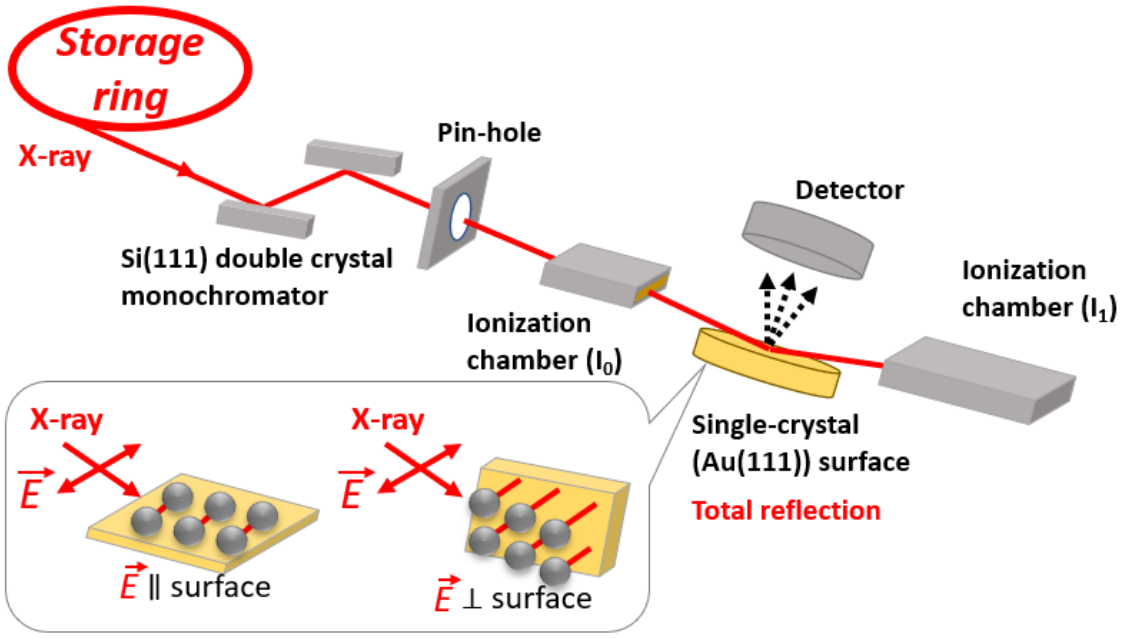

Figure 2-9. Schematic diagram for polarization dependent XAFS measurement when polarization vector is parallel and perpendicular to surface, respectively.

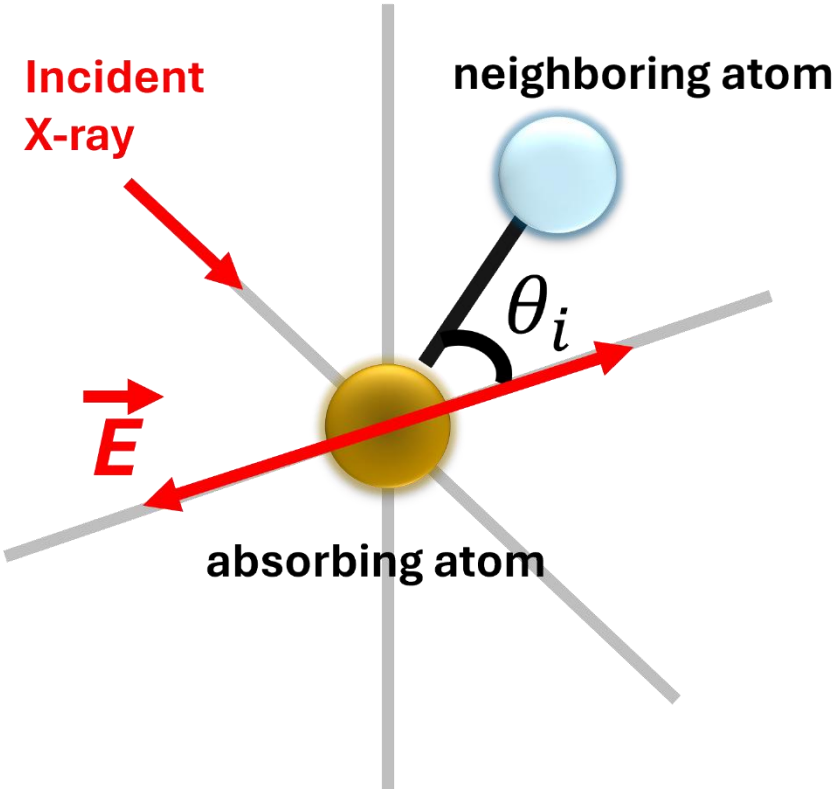

Figure 2-10. Schematic diagram for polarization dependent feature between the absorbing atom and the neighboring atom.

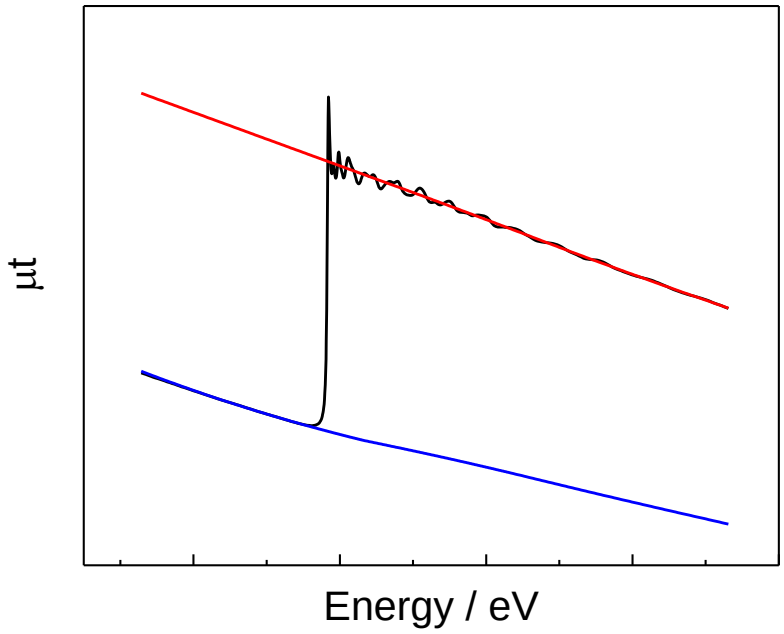

Figure 2-11. EXAFS spectrum and extrapolation or interpolation line for background removal. The blue line shows the pre-edge region (μ_{pre}) and the red line shows post-edge region (μ_{post}).

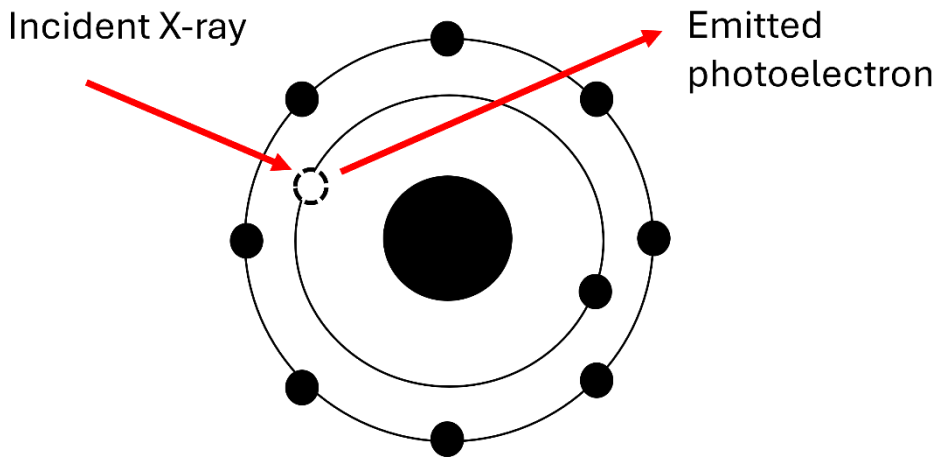

Figure 2-12. Schematic illustration for photoelectron generation process.

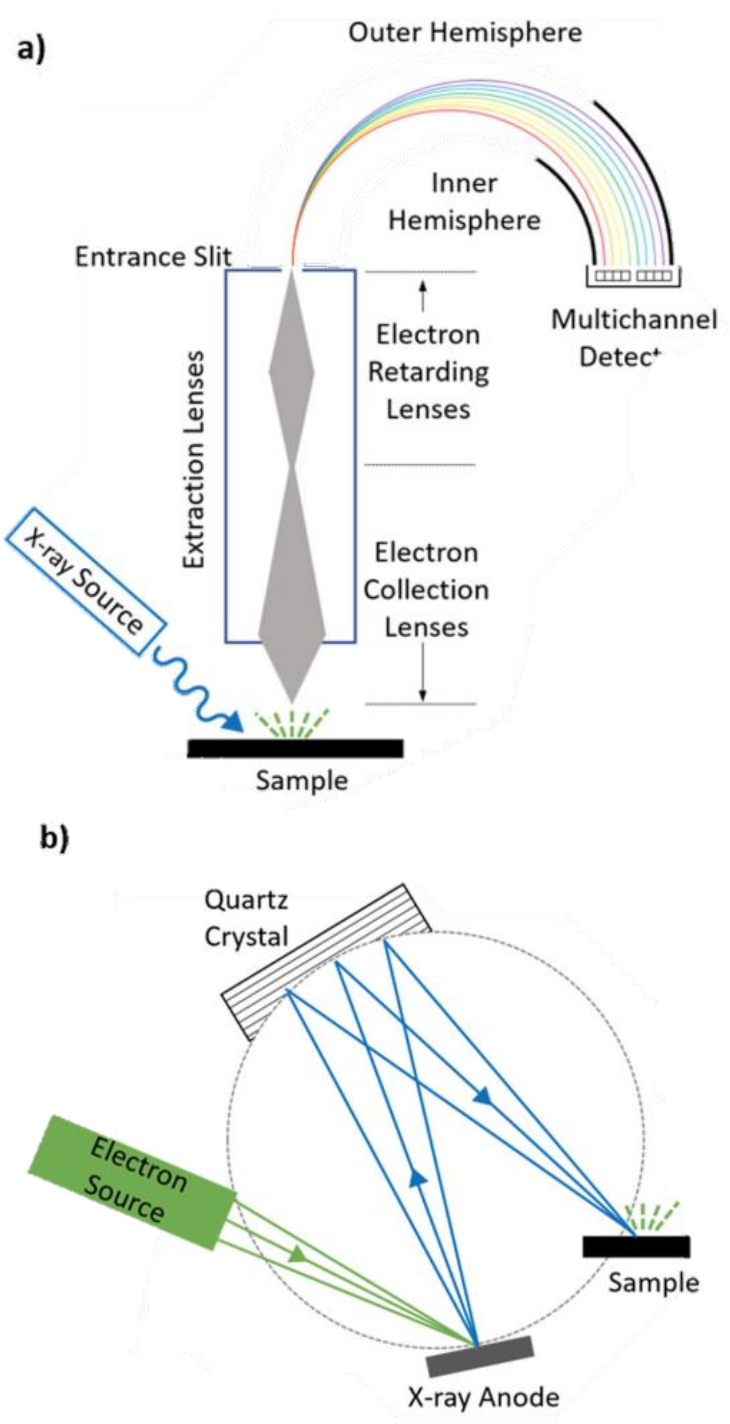

Figure 2-13 (a) XPS components and (b)monochromator configuration[10].

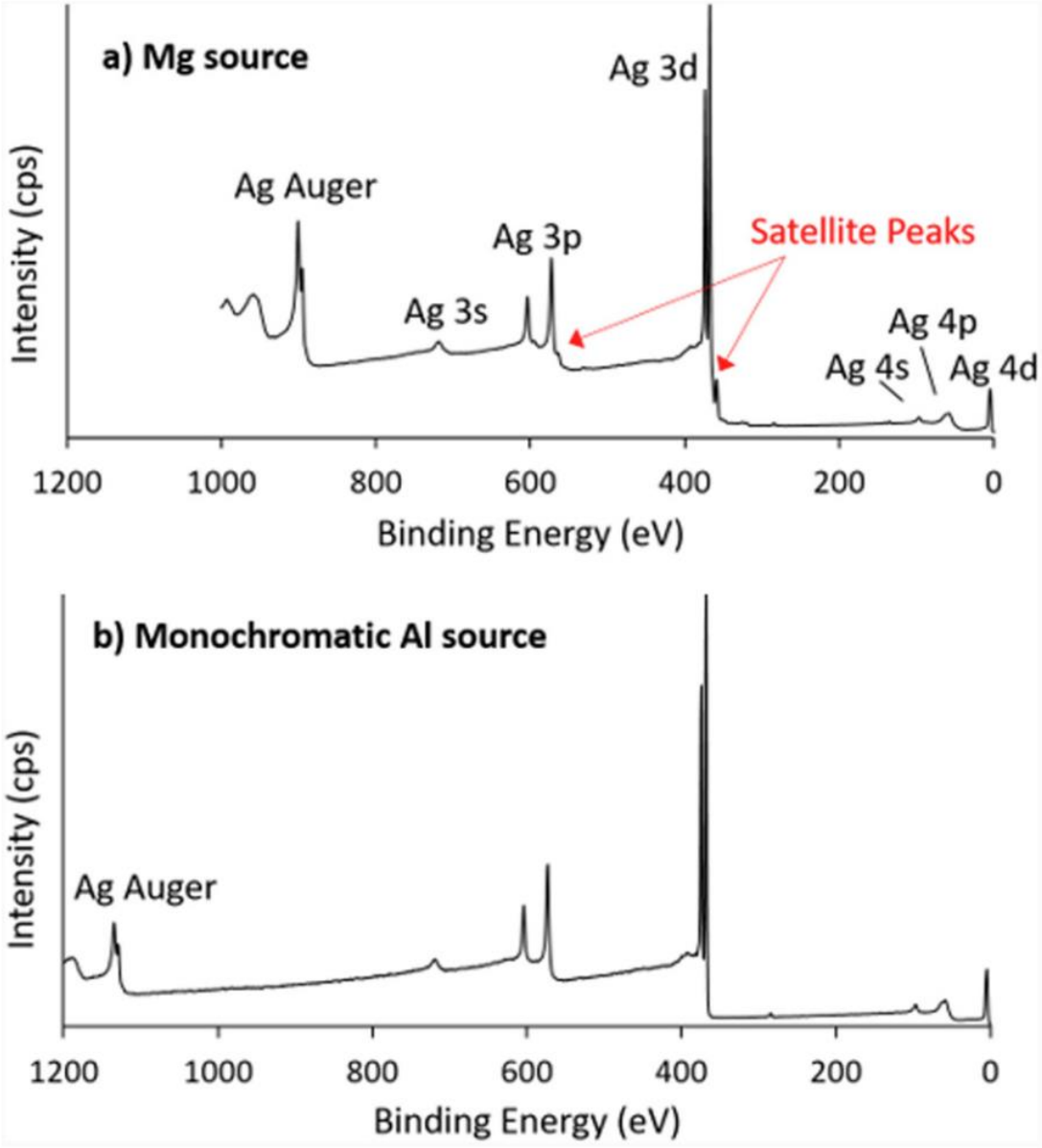

Figure 2-14. Survey spectra for silver with (a) nonmonochromatic Mg and (b) monochromatic Al sources show how the photoelectron peaks are at the same binding energies but the Auger peaks shift with the use of different sources[10].

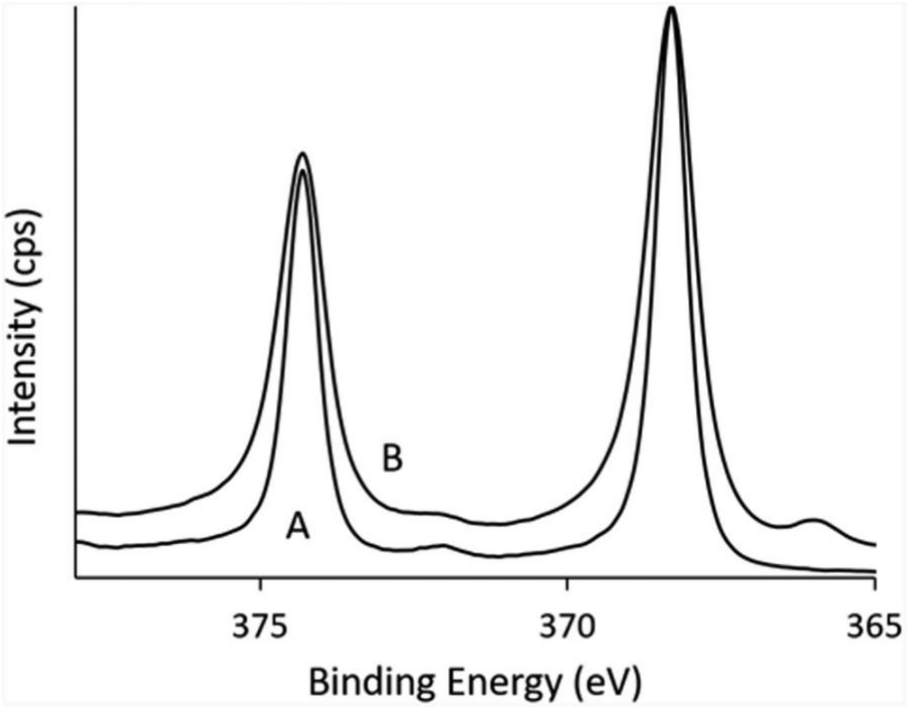

Figure 2-15. XPS high-resolution spectra from a silver sample show the reduction in Ag 3d linewidth obtained from a monochromatic source (a) compared with a nonmonochromatic Mg source (b)[10].

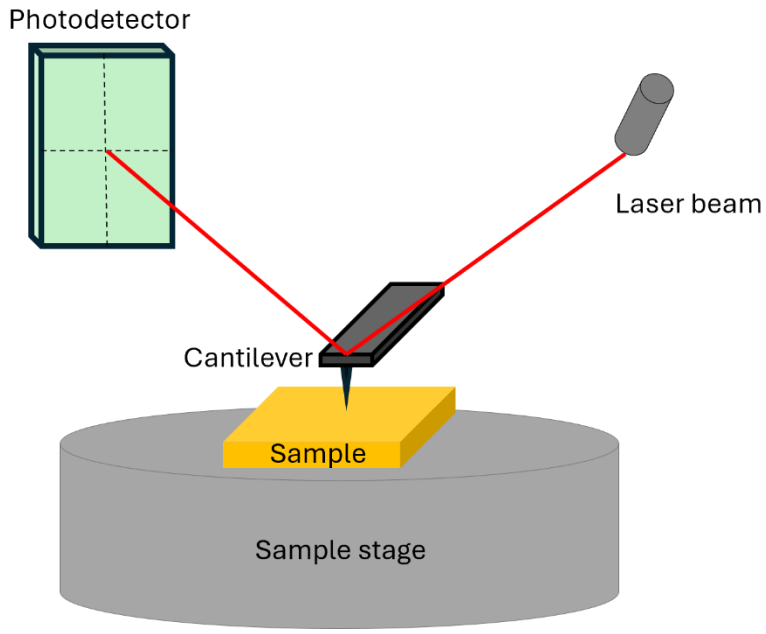

Figure 2-16. Basic configurations in AFM.

Reference

[1] N. Umezawa, S. Sano, N. Aoki, G. Friedbacher, T. Kondo, Electrochemistry 82 (2014) 346–350.

[2] S. Ambrozik, N. Dimitrov, Electrochimica Acta 169 (2015) 248–255.

[3] N. Dimitrov, Electrochimica Acta 209 (2016) 599–622.

[4] D. Gokcen, S.-E. Bae, S.R. Brankovic, Electrochimica Acta 56 (2011) 5545–5553.

[5] S.R. Brankovic, J.X. Wang, R.R. Adžić, Surface Science 474 (2001) L173–L179.

[6] Y. Wakisaka, D. Kido, H. Uehara, Q. Yuan, F.E. Feiten, S. Mukai, S. Takakusagi, Y. Uemura, T. Yokoyama, T. Wada, M. Uo, O. Sekizawa, T. Uruga, Y. Iwasawa, K. Asakura, The Chemical Record 19 (2019) 1157–1165.

[7] N. Tamura, Reviews in Mineralogy and Geochemistry (2002).

[8] D. Friebel, V. Viswanathan, D.J. Miller, T. Anniyev, H. Ogasawara, A.H. Larsen, C.P. O'Grady, J.K. Nørskov, A. Nilsson, J. Am. Chem. Soc. 134 (2012) 9664–9671.

[9] D. Kido, Y. Uemura, Y. Wakisaka, H. Ariga-Miwa, S. Takakuasgi, K. Asakura, E-Journal of Surface Science and Nanotechnology 18 (2020) 249–261.

[10] F. Stevie, C. Donley, Journal of Vacuum Science & Technology A 38 (2020) 063204.

CHAPTER 3 Development of *in-situ* BCLA enhanced BI/HERFD-XAFS for structure investigation of monometallic Platinum catalyst system

The oxygen reduction reaction (ORR) at the cathode side of PEMFC is the crucial rate determining step where a porous carbon supported Pt species is mainly used[1–5]. The conventional *in-situ* XAFS technique revealed the geometrical and electronic structures of heterogeneous powders Pt/C catalysts. However, porous powder systems usually show inhomogeneous and ill-defined surfaces[6,7]. A flat surface is preferred because surface science techniques such as AFM and XPS are easily applied to define the surface more clearly. HOPG is a suitable candidate, which possesses a flat and well-defined surface to make the characterization of Pt NPs easier under ORR conditions[8]. The main challenge in preparing model catalysts was to obtain monodisperse Pt NPs. Miyabayashi et al.[9] reported the Pt nanocluster with a sharp distribution prepared by two phase liquid reduction method. The combination of the well-defined HOPG surface and monodisperse Pt NPs makes it possible to investigate the structure of NPs more precisely by the *in-situ* XAFS technique.

In this chapter, the structure as well as the surface adsorbates of the well-dispersed Pt NPs in a few MLs deposited on a flat HOPG, a model system for fuel cell catalysts, was characterized by *in-situ* BCLA + BI-XAFS and HERFD + BI-XANES methods. The developed method overcame the limitation of conventional transmission mode, where small target element amount and existence electrolyte greatly inhibited the fluorescence signal detections.

3.1 Limitation of existed XAFS apparatus and Development of *in-situ* electrochemical Bent Crystal Laue Analyzer + Back illuminated / High Energy Resolution Fluorescence Detection XAFS

XAFS has a low sensitivity when applied to nanoparticles on a flat surface. The edge height is estimated to be 1×10^{-4} order in transmission mode, considering exposure of 1.5×10^{15} Pt atoms cm^{-2}, which is used to define one monolayer (ML) throughout this dissertation. The fluorescence XAFS method can be applied to the diluted system. However, it is still difficult to detect the surface species due to the X-ray scattering from the bulk. The polarization dependent total reflection fluorescence XAFS (PTRF-XAFS) [10–13] has been applied to investigate the metal species on a flat surface under *in-situ* conditions. However, this technique is not applicable to the Pt/HOPG system for the following reasons[14].

1. The critical angle for the total reflection becomes smaller since carbon is a low Z element. For example, at 10 keV the critical angle for C is 2.8 mrad as shown in Figure 3-1, while that of Au is 7 mrad.
2. HOPG is a mosaic crystal, which gives less reflectivity. In addition, the flatness of HOPG at the macro level is low; ripples are observed on the HOPG surface by naked eyes.
3. The coexisting electrolyte greatly absorbs the incident X-rays, leading to a large reduction in the incident X-rays intensity and a tremendous increase in scattering X-rays. As a result, S/B (signal to background ratio) becomes worse even under total reflection conditions. Thus, it is necessary to make the solution layer thickness as small as possible, for example a few micrometers, which in turns diminishes the material diffusion of reactants and products to the catalyst surface compared to the thick solution case [15].

Therefore, an alternative type of high sensitivity XAFS is developed for metal species on the HOPG surface, termed *in-situ* back-illuminated (BI)-XAFS as shown in Figure 3-2(a). The apparatus configuration details has been discussed in Chapter 2. *In-situ* BCLA+BI-XAFS and HERFD+BI-XANES were carried out in the BL36XU at SPring-8 (Super Photon ring-8 GeV, JASRI, Japan)[16–19]. Figure 3-2 shows the *in-situ* BI-XAFS cell. The cell body was made of polychlorotrifluoroethylene (PCTFE), which exhibited sufficient chemical stability against strong acid in addition to mechanical strength. The cell body was equipped with two electrodes, where a reversible hydrogen electrode (RHE) was used as the reference electrode (RE) and the Pt wire was as the counter electrode (CE). All potentials are reported with respect to RHE. The backside of the cell was covered with transparent plastics (acrylic plastic plate) for internal observations. The thin HOPG window was placed at the hole on the center of the frontside of the cell body and was held on with a cover plate and sealed with a Teflon O-ring. The sample surface with the deposited Pt NPs was mounted toward electrolyte while the other side of the HOPG was exposed to air. Here, the HOPG had three roles:

1. Pt NPs support;
2. incident and fluorescence X-rays window;
3. working electrode (WE).

Note that the frontside of HOPG was defined to be the side containing Pt NPs and contacting electrolyte, while its backside was the air-exposed side. After depositing the NPs, the backside of the HOPG was peeled to ensure no Pt NPs were deposited on it. The X-ray incident angle was set approximately at a magic angle (54.7º) with respect to the HOPG surface, because little polarization-dependence of the Pt NPs was found due to its spherical shape. The emitted fluorescence signal was monochromatized by the BCLA. A thin Si (100) (Sharan Instrument Co;

diffraction plane = Si (111); χ (asymmetry angle) =17.5°) was bent log-spirally using the log spirally shaped metal frame. The front and backward beams were made by technique division of home institute[16]. The height and distance of the BCLA to the sample were precisely adjusted to fit the focal points of BCLA and the incident X-rays. Both focal points were set on the HOPG surface. The fluorescence X-rays were finally collected by a 25-element Ge solid-state detector (SSD, Canberra, USA). In the HERFD+BI-XANES measurements, the BCLA was replaced with eight sets of Johann-type Ge (660) bent crystals to select Pt L_3 edge fluorescence signal (9442 eV) with high energy resolution. The signal was further accumulated by a pixel array detector (Merlin Quad, Quantum Detector). Approximately 1 eV energy resolution was attained[19].

An *in-situ* electrochemistry measurement was carried out in the above-mentioned BI-XAFS cell during XAFS measurements in 0.1 M $HClO_4$ (60%, Wako company, Japan). The electrolyte was purged by N_2 during the experiment, and electrolyte was circulated between the reservoir and *in-situ* XAFS cell by a bimorph pump (BPF-465P, Nitto Kohki) throughout the XAFS measurement. Before XAFS measurement started, several cycles of cyclic voltammetry (CV) scanning in 0.1 M $HClO_4$ solution (scan rate = 50 mV s^{-1}) were conducted between 0 V_{RHE} to + 1.45 V_{RHE} to remove the surface organic layer and expose the Pt NPs. The XAFS measurement was carried out at several potentials between 0 V_{RHE} to + 1.00 V_{RHE}. XAFS measurements were started after a certain potential was applied to WE for several minutes to reach electrochemical equilibrium.

3.2 Sample preparation and Surface characterizations

3.2.1 Sample preparations and surface characterizations

All Chemicals were purchased and used without any further purifications. A thin HOPG (ZYA Grade, mosaic spread (MS)=3.5˚ ± 1.5˚) of 1×1 cm^2 with a thickness of tens of micrometers was used as a flat substrate, which was obtained by the peel-off method with Scotch tape. The obtained

surface was cleaned under ultrasonic power in 18.2 MΩ cm ultrapure water (UPW; Milli-Q, Merck Millipore Co.) several times.

Monodispersed Pt NPs were prepared by a two-phase liquid reduction method[9]. The Pt NPs redispersed in benzene solvent were deposited on HOPG several times via a spin-coating method at 3000 rpm for 3 min. Then, the sample was left in a fume hood for 10 min to confirm the evaporation of benzene solvent. Finally, the obtained sample was washed with UPW.

The Pt loading was checked by XPS (JPC-9010MC, JEOL, Japan) equipped with a Mg Kα (1253.6 eV) X-ray source, operated under 10^{-6} Pa at 10 kV and 10 mA. The binding energies (B.E.) was calibrated using the C 1s peak set at 284.6 eV[20]. XPS analysis was carried out by XPSPEAK41 software. The Pt 4f peak fitting using Lorentzian-Gaussian curves was carried out after background removal by the Shirley method. The Pt NPs size was characterized by transmission electron microscopy (TEM) operated at 200 kV (JEM-2100F, JEOL, Japan).

The XAFS analysis was performed by REX 2000 (Rigaku Co., Japan) packages for XANES normalization and EXAFS background subtraction and oscillation extraction[21]. The theoretical simulation was conducted by FEFF8 code[22].

3.2.2 Pt/HOPG Surface Investigation

Figure 3-3 shows the TEM image of Pt NPs and their corresponding size histogram. The estimated average particle diameter was 2.4 ± 0.3 nm. Figure 3-4 shows the XPS narrow scan in the C 1s and Pt 4f regions for Pt/HOPG samples used for *in-situ* XAFS measurement. XPS calculation details were summarized as follows. Here, a layer-by-layer growth model on HOPG was assumed, which gave a total Pt atom amount as $(2.3 \pm 0.4) \times 10^{15}$ Pt atoms cm^{-2}.

As mentioned in main text, the definition of one monolayer is explained as Pt atom density, that is, the number of Pt atoms (n_{0Pt} arranged in fcc (1 × 1) cm^2 unit cell, which is calculated as 1.5× 10^{15} Pt atoms cm^{-2}.

The relationship between atom numbers and peak intensity obtained from XPS measurement is described as:

$$I = I_0 \cdot \sigma \cdot n \cdot \gamma \tag{3-1}$$

where I is the measured intensity for target element, I_0 is the incident X-ray intensity, σ is the cross section for specific species, and n is the number of the target atom, γ is the correction factor for the escape depth. For Pt and C species, the incident X-ray intensity is the same, while the cross sections are $\sigma_{Pt\ 4f\ 7/2}$= 8.65 and $\sigma_{C\ 1s}$= 1.00. As photoelectrons travelling within materials go through an inelastic scattering process, it is necessary to consider the γ.

For $C\ 1s$ peak,

$$\gamma_C = \left(1 + e^{-\frac{d_C}{\lambda_C}} + e^{-\frac{2d_C}{\lambda_C}} + \cdots + e^{-\frac{nd_C}{\lambda_C}}\right) = \frac{1}{1 - e^{-\frac{d_C}{\lambda_C}}} \tag{3-2}$$

d_C and λ_c are layer distance and photoelectron mean free path, determined as 3.35 Å and 30.52 Å, respectively. Thus, $\gamma_C = 9.62$. The HOPG possess a honeycomb configuration with a C-C bond distance of 1.42 Å, the number of carbon atoms in unit cell of 1 × 1 cm^2 is n_{0C} = 3.82 × 10^{15} C atoms cm^{-2}.

The ratio of measured peak intensity between $Pt\ 4f\ 7/2$ peaks and $C\ 1s$ peak is given by:

$$\frac{I_{Pt\,4f\frac{7}{2}}}{I_{C\,1s}} = \frac{I_0 \cdot \sigma_{Pt} \cdot n_{Pt} \cdot \gamma_{Pt}}{I_0 \cdot \sigma_C \cdot n_{0C} \cdot \gamma_C} = \frac{8.65 \times n_{Pt} \times \gamma_{Pt}}{9.62 \times 3.82 \times 10^{15}} = 2.35 \times 10^{-16}\, n_{Pt}\gamma_{Pt}$$

(3-3)

The ratio between measured peak intensities of $\frac{I_{Pt\,4f\,7/2}}{I\,C1s}$ is given as 0.52. Consequently, $n_{Pt}\gamma_{Pt} = 2.21 \times 10^{15}$ Pt atoms cm^{-2}. As

$$\gamma_{Pt} = \frac{n_{0,Pt}\left(1 + e^{-\frac{d_{Pt}}{\lambda_{Pt}}} + e^{-\frac{2d_{Pt}}{\lambda_{Pt}}} + \cdots + e^{-\frac{nd_{Pt}}{\lambda_{Pt}}}\right)}{n_{Pt}}$$

(3-4)

which greatly depends on the layer distance and photoelectron mean free path, determined as $d_{Pt} = 2.29$ Å, $\lambda_{Pt} = 14.78$ Å, respectively, as well as morphology, Here, a layer by layer growing mode was assumed for Pt loading calculation.

For Pt amount less than 1 ML, $\gamma_{Pt} = 1$. Since 1 ML Pt corresponds to n_{0Pt} =1.49 × 10^{15} Pt atoms cm^{-2}, 2.21×10^{15} Pt atoms cm^{-2} means more than 1 ML coverage was appeared on HOPG surface.

For real Pt coverage given between 1 ML and 2 ML. Considering the θ is coverage of second layer or $\theta = \frac{n_{Pt}}{n_{0Pt}} - 1$.

$n_{Pt}\gamma_{Pt} = 2.21 \times 10^{15}$ Pt atoms cm^{-2} $= (1 + 0.86\,\theta) n_{0,Pt}$

(3-5)

Therefore, θ = 0.56, $n_{Pt} = n_{0Pt}(1 + 0.56) = 2.32 \times 10^{15}$ Pt atoms cm^{-2}, $\gamma_{Pt} = 0.96$.

Figure 3-5 shows the CV curve just before the XAFS measurements. Hydrogen adsorption and desorption were found below 0.35 V_{RHE}, which gave an exposed electrochemical surface area (ECSA) of Pt that corresponding to $(1.4 \pm 0.3) \times 10^{15}$ Pt atoms cm^{-2}. Therefore, the ratio between surface Pt atom to total Pt atom was (60 ± 20) %. A small double-layer region window was found around 0.4 V_{RHE}, which was usually considered to be clean surface or free from adsorbates[23]. Consequently, 0.4 V_{RHE} was taken as a reference potential in XAFS measurement. In the anodic scan, the current gradually increases from 0.6 V_{RHE} and surface oxidation occurs after 1.2 V_{RHE}. In the cathodic scan, the surface oxide reduction peak appears at 0.7 V_{RHE}.

3.3 *In-situ* structure determination of Pt Nanoparticles

Figure 3-6 shows the EXAFS $\chi(k)$ oscillations at 0.4 V_{RHE} and 0.1 V_{RHE} as well as that for Pt foil. The $\chi(k)$ oscillation for 0.4 V_{RHE} and 0.1 V_{RHE} resembled that for Pt foil, suggesting that the Pt local structures in Pt NPs was analogous to that for Pt foil or face centered cubic (fcc) like structure. The wavelength for $\chi(k)$ oscillations was in good agreement with that for Pt foil, indicating the bond distance was the same as that for Pt foil. The bond length contractions occurred in nanoparticles less than a few nm and H adsorption lifted the bond length contraction under the He flow and/or under vacuum[24]. In this work, bond contraction phenomenon was not observed. The amplitudes were reduced and damped more quickly when compared to Pt foil. The preliminary curve fitting analysis showed that the Pt-Pt distance was 2.76 Å.

Figure 3-7 shows the $\chi(k)$ oscillations from 0.4 V_{RHE} to 1.0 V_{RHE}. The experimental $\chi(k)$ oscillation at more positive potentials showed features comparable to those for 0.4 V_{RHE} and Pt foil, indicating that Pt NPs on the HOPG system possessed a fcc like structure, though the $\chi(k)$ oscillations underwent a slight change around 5.7 $Å^{-1}$ found at 1.0 V_{RHE}. The small dependence of

XAFS oscillations on potential indicated that the Pt NPs in the Pt/HOPG system had a stable framework.

Taking the above observations into account, Pt nanoparticle model structure was constructed, and a real-space simulation was performed by FEFF. Simulation was carried out for the Pt NPs at 0.4 V_{RHE} and assumed to have an adsorbate-free surface. The Pt NPs had several frameworks such as cuboctahedron and icosahedron[10,25,26]. The octahedron had the same fcc structure as the Pt foil. On the other hand, the icosahedron model possessed two kinds of Pt-Pt bond distances and the icosahedron structure was reported to be stable for the Pt nanoparticle smaller than 1 nm[25,26]. Considering the similarity of the $\chi(k)$ oscillation for Pt NPs at 0.4 V_{RHE} and Pt foil, the cuboctahedron structure was created on the HOPG. FEFF simulation was carried out using cuboctahedron model. Judging from average size (2.4 nm) derived from TEM and (60 ± 20) % surface atom fractions estimated from CV and XPS, a cuboctahedron model with 309 atoms, termed O_h-Pt_{309}, was assumed, which had the particle size of about 2.4 nm and 52% (162 surface Pt atoms/309 overall Pt atoms = 52 %) surface coverage. The Pt-Pt bond distances and Debye-Waller (DW) factors were optimized. The goodness of fit between the experimental $\chi_{exp}(k)$ and calculated $\chi_{cal}(k)$ was evaluated by χ^2 test using the following equation:

$$R^2 = \frac{1}{N}\sum_{k}\frac{\{\chi_{exp}(k) - \chi_{cal}(k)\}^2}{\varepsilon(k)^2} \qquad (3\text{-}7)$$

where N and $\varepsilon(k)$ are the number of the data points and the error estimated from experimental data, respectively. The criteria of the goodness of fitting were less than the unity.

Figure 3-8 shows the FEFF simulation result with the first shell Pt-Pt distance at 2.76 Å and s^2 at 0.0081 $Å^2$. The Debye-Waller factor was larger than that of Pt foil (0.0036 $Å^2$) as shown in Table 3-1 with the uncertainties derived from χ^2 test. This structure framework was maintained over a wide range of potentials from 0.1 V_{RHE} to 1.0 V_{RHE}. Fittings at other potentials using the same model are shown in Figure 3-9.

The EXAFS results suggested that Pt NPs possess a cuboctahedron model O_h-Pt_{309} with an average bond distance of 2.76 ± 0.06 Å. Based on the Pt NPs with an average size of 2.4 nm, we recalculated the Pt loading from XPS intensity by assuming a simplified cubic structure. The calculation details is described follows:

If the cuboctahedron model with 309 Pt atoms was simplified as a cubic model with 9 layers thickness,

$$n_{Pt}\gamma_{Pt} = 2.2 \times 10^{15} = \left(1 + e^{-\frac{d_{Pt}}{\lambda_{Pt}}} + e^{-\frac{2d_{Pt}}{\lambda_{Pt}}} + \cdots + e^{-\frac{8d_{Pt}}{\lambda_{Pt}}}\right) n_{1,pt} \quad (3\text{-}6)$$

where $n_{1,Pt}$ is number of Pt atoms in each layer of a cubic model. Therefore, $n_{Pt} = 9 \times n_{1Pt}$, $n_{Pt} = 3.70 \times 10^{15}$ Pt atoms cm^{-2}.

This model gave a Pt atom density as $(3.7 \pm 0.4) \times 10^{15}$ Pt atoms cm^{-2}, while layer by layer model gave the minimum value $(2.3 \pm 0.4) \times 10^{15}$ Pt atoms cm^{-2}). Therefore, the real Pt loading could be assumed as $(3.0 \pm 0.6) \times 10^{15}$ Pt atoms cm^{-2}. Thus, the ratio of surface Pt atoms to total Pt atoms in NP was (50 ± 30) % (estimated from both CV and XPS results), which is comparable to the ratio between surface Pt atoms and total Pt atoms in O_h-Pt_{309} (50 %). Consequently, the O_h-Pt_{309} was the most plausible model for the Pt on HOPG determined by BI+BCLA-XAFS. The first shell Pt-

Pt bond distance 2.76 Å at 0.4 V_{RHE}. The framework of Pt NPs on HOPG was stable during the potential range of 0.1 V_{RHE} to 1.0 V_{RHE}. In the previous group research, PtAu alloy particles[18] on HOPG prepared by arc plasma deposition (APD) method changed in size during the repeated CV scanning, probably because of the presence of adatoms on the surface or ill-shaped NPs, which were reactive and further induced changes in NPs structures. The Pt NPs synthesized by the APD method were dissolved at the more positive potential (1.0 V_{RHE}) and reduced again at more negative potential, which induced aggregation of the particles[18].

It can be concluded that Pt NPs have an O_h-Pt_{309} structure and are stable against the electrochemical conditions even at 1.0 V_{RHE}.

3.4 Surface Adsorbates Investigation

Figure 3-10 shows XANES spectra collected at 0.4 V_{RHE} and 0.1 V_{RHE} by the BCLA+BI-XAFS method. Clear peak broadening feature was found after white line peak at 0.1 V_{RHE} compared to 0.4 V_{RHE}. Figure 3-11 shows the difference spectrum between 0.1 V_{RHE} and 0.4 V_{RHE} obtained by subtracting 0.4 V_{RHE} spectrum as the reference, where a negative peak at the edge and a positive peak at 8 eV higher than the edge appeared. These features well corresponded to the difference spectra after the hydrogen adsorption on Pt surface[27–29].

Since little difference was found in each difference spectrum at potentials higher than 0.4 V_{RHE} when using BI-XAFS, we carried out HERFD+BI-XANES to clarify the difference. Figure 3-12 shows the normalized Pt L_3 edge XANES spectra collected by HERFD+BI-XANES under more positive potentials. Sharper white line (WL) intensities were observed in HERFD spectra though there were barely substantial changes in WL features. However, the difference spectra between the XANES spectra of the specific potentials and 0.4 V_{RHE} showed significant difference as seen in Figure 3-13. For spectra from 0.6 V_{RHE} to 1.0 V_{RHE}, the peak shifted from 11565.34 eV to 11567.31

eV as the applied potential increased. The peak positions corresponded well to the reported ones, where a difference peak at 11565 eV appeared near 0.6 V_{RHE} and the peak shifted to 11567 eV with the potential increased to 1.0 V_{RHE}[30]. In the literature, the peak position at 11565 eV was assigned to the surface adsorption of OH species, while that at 11567 eV was related to surface oxygen adsorption or oxide formation[31–33]. The XANES difference spectrum was calculated by FEFF. The spectrum at 11565 eV was reproduced by adsorbed OH at hexagonal close-packed (hcp) three-fold sites, while the spectrum at 11568 eV was reproduced by adsorbed oxygen on bridge site. The gradual change between the two potentials might be explained by the gradual change of the OH/O ratio on the surface. If this is correct, the spectrum could be reproduced at intermediate potentials by a linear combination of two spectra at 0.6 V_{RHE} and 1.0 V_{RHE}. However, the spectrum cannot be simply reproduced by the linear combination, meaning that there is some interaction between the adsorbates of OH and O. Since the adsorbates-induced XANES structure was caused by multiple scattering, the peak position relative to the edge (ΔE) was related to the distance between the Pt and adsorbate species (r) as $\Delta E \propto \frac{1}{r}$ based on multiple scattering theory of XANES[34]. The Pt-OH bond was longer than the Pt-O bond, so the peak position, ΔE, for Pt-OH is expected to be smaller than that for Pt-O. If the adsorbed OH and O interact with each other to modify the bond length between OH/O and Pt, the gradual change of the peak position shown in Figure 3-14 could be explained. It can be assumed the interaction between OH and O was through hydrogen bonds where OH and O were not clearly distinguished and formed an OH/O network cluster interacting with the Pt surface. The OH/O network cluster formed through hydrogen bond could have different bond length with Pt depending on the ratio of OH/ O, which is affected by the applied potential. Consequently, the peak position was continuously shifted with the potential. This proposal will be further confirmed by other investigations.

In summary, HERFD-XANES provides a better XANES shape definition and signal gain, which can solve the problem regarding the poor features of pre-edge and post-edge features that exist with the conventional method. HERFD-XANES is also more sensitive to the surface adsorbates, for example, -OH and -O species. With these merits, surface adsorbates on noble metals can be distinguished.

3.5 Conclusion

An *in-situ* BCLA/HERFD + BI-XAFS method was used to investigate the monometallic Pt structure in a model catalyst system. The system consisted of a well-defined HOPG surface covered by a limited amount ($\sim 10^{15}\ Pt\ atoms\ cm^{-2}$) of Pt particles with a narrow size distribution. Pt L_3 edge EXAFS spectra was successfully obtained up to 11 $Å^{-1}$ in k space under *in-situ* conditions. EXAFS analysis suggested that a stable Pt structure framework, O_h-Pt_{309} with 2.76 ± 0.06 Å, was formed. The framework was maintained over the potentials from 0.1 V_{RHE} to 1.0 V_{RHE}. *In-situ* HERFD+BI-XANES results established that there is a potential dependent surface adsorbate feature. This developed *in-situ* XAFS measurement method overcomes the limitation of conventional XAFS measurement in transmission mode, where the low sensitivity is usually observed, as well as the limitations exists in the typical fluorescence mode, where the scatterings coming from the electrolyte greatly inhibited the target element signals. BCLA plays an essential role in selecting the specific fluorescence signals if placed in a suitable focal point, which can be further applied in XAFS measurement for other model catalyst systems. This method is also suitable for the investigation of Pt structure on HOPG and surface adsorbates studies, which can be further applied to fundamental research toward fuel cell catalysts.

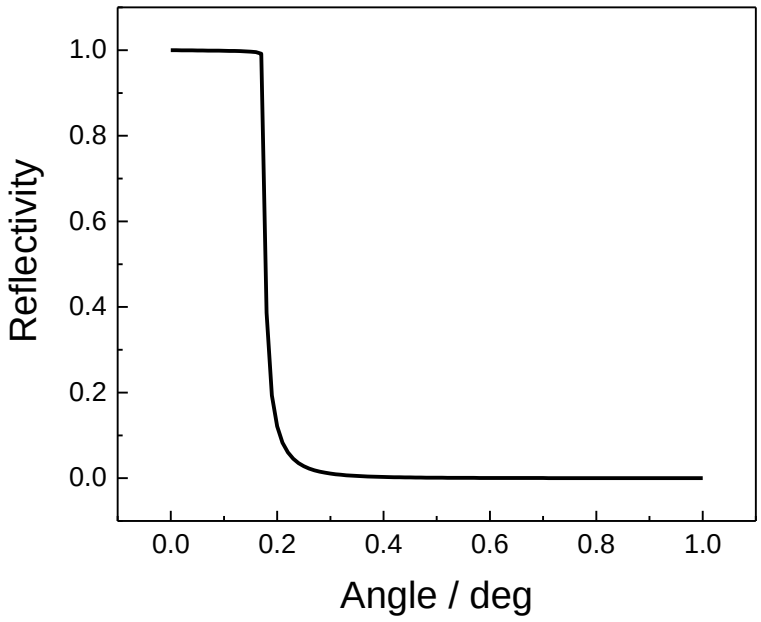

Figure 3-1. The critical angle for HOPG at energy of 10 keV.

The critical angle for HOPG is calculated as 0.16 degree, corresponding to 2.8 mrad. The data were calculated using the following homepage of Center of X-ray optics, Lawrence Berkeley National Laboratory's (LBNL) Materials Sciences Division (MSD).

https://henke.lbl.gov/optical_constants/mirror2.html

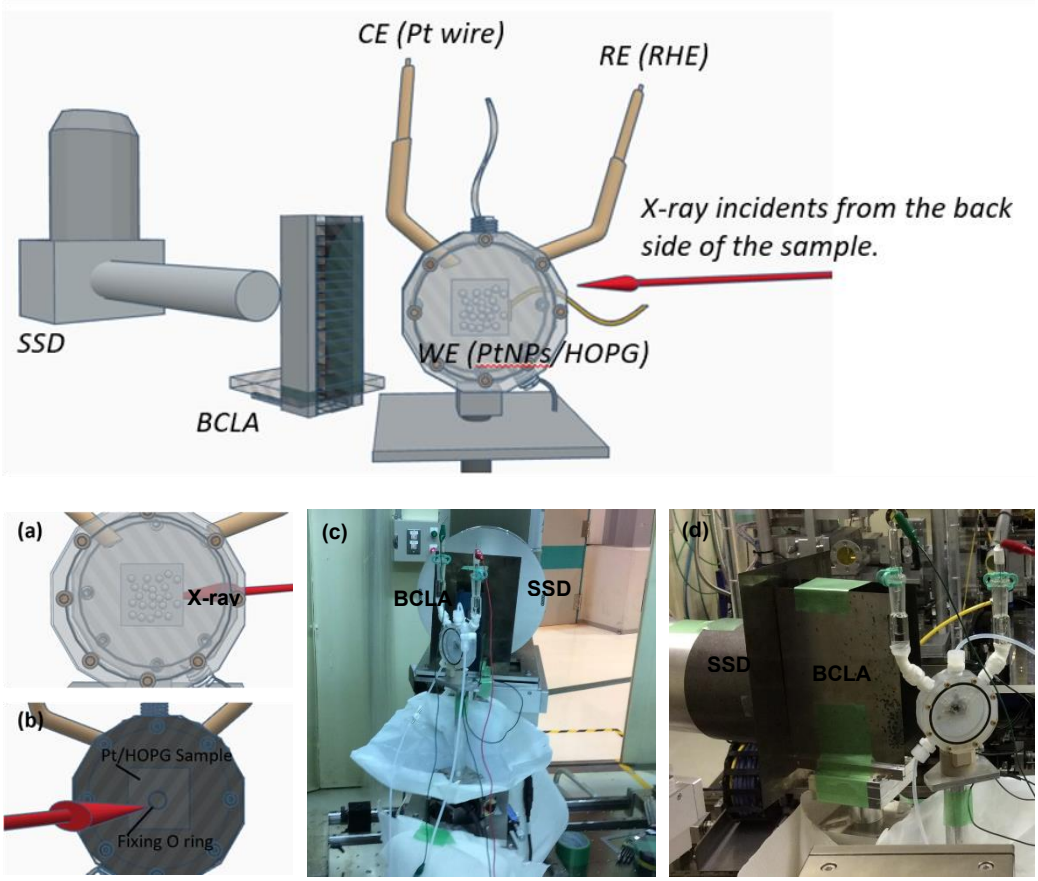

Figure 3-2. *In-situ* BCLA+BI-XAFS apparatus. The insert figures (a) is the back view and (b) is the front view (c) side view picture (d) back view picture

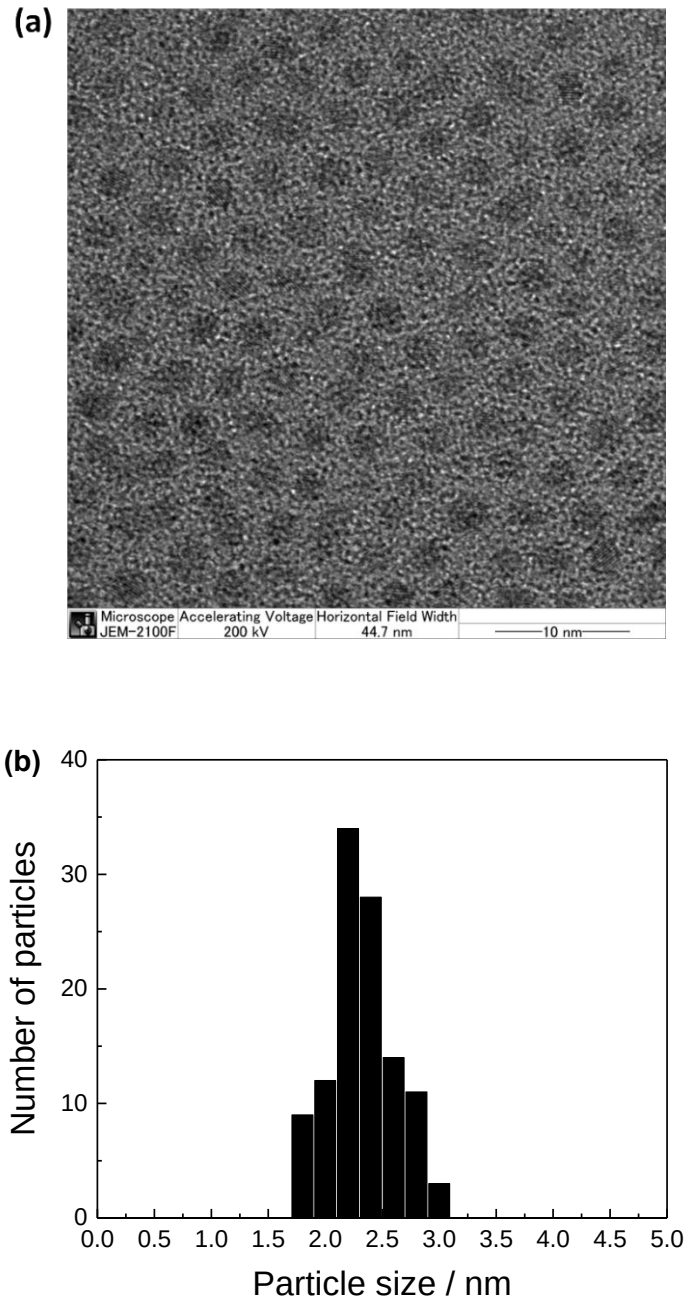

Figure 3-3. (a) TEM image of Pt NPs prepared via a two-phase liquid reduction method, (b) size histogram for Pt NPs in (a).

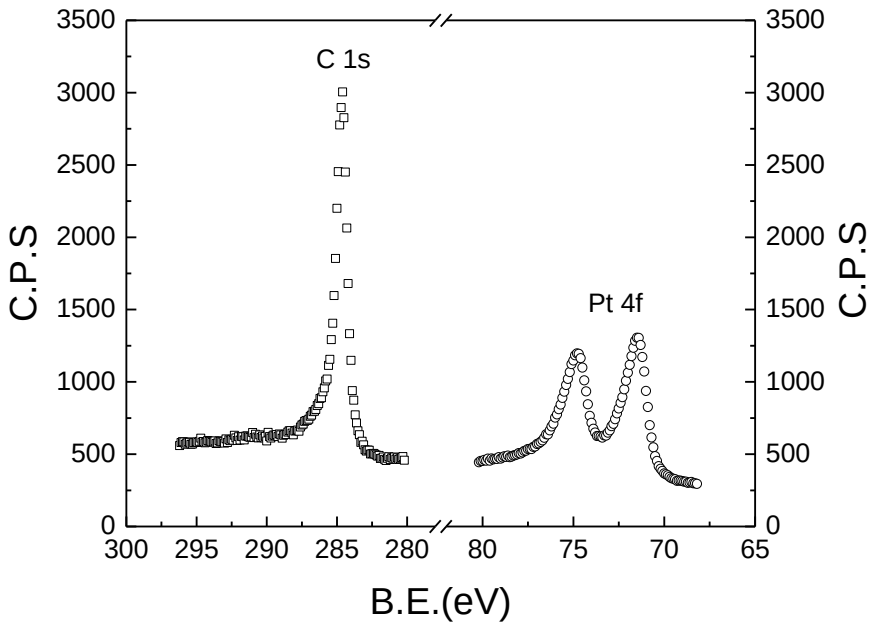

Figure 3-4. XPS C 1s (square) and Pt 4f (circle) of Pt NPs/HOPG used for BCLA+BI-XAFS measurement.

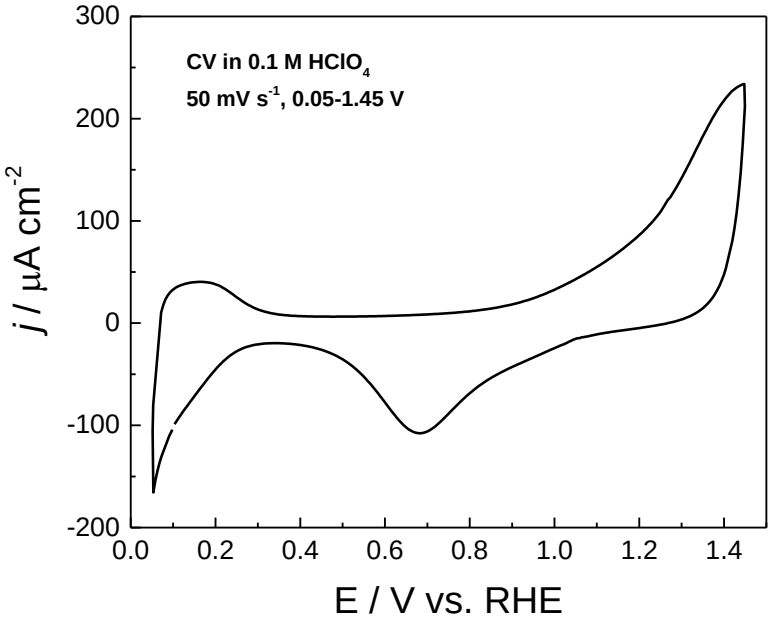

Figure 3-5. Cyclic voltammetry (CV) after several cycles just before the XAFS measurements starts.

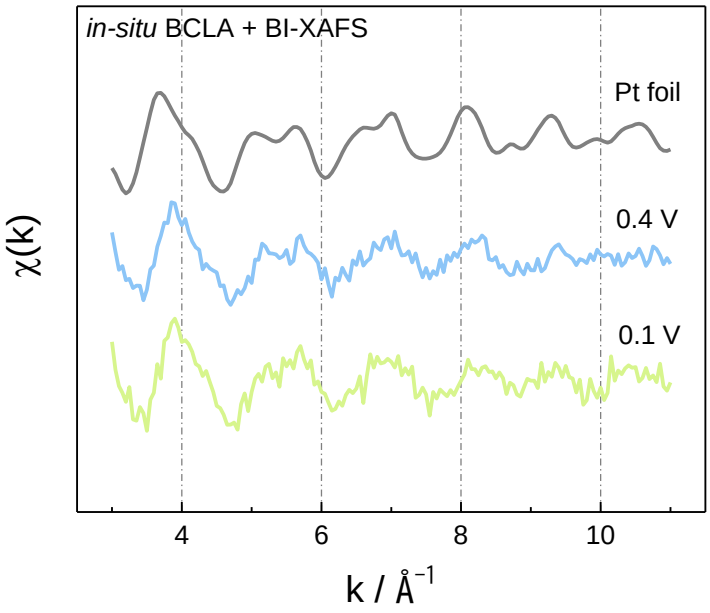

Figure 3-6. *In-situ* EXAFS χ(k) spectra for Pt NPs/HOPG collected under 0.4 V_{RHE} and 0.1 V_{RHE} as well as Pt foil.

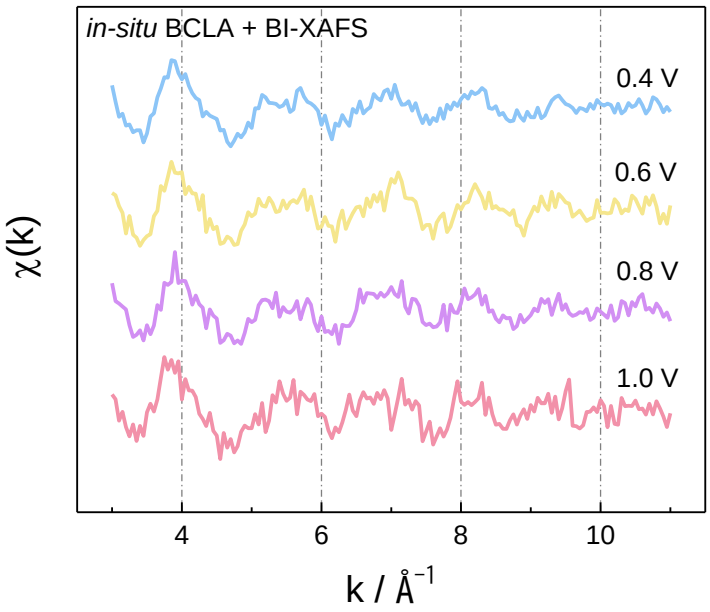

Figure 3-7 *In-situ* EXAFS χ(k) spectra for Pt NPs/HOPG collected under 0.4 V_{RHE}, 0.6 V_{RHE}, 0.8 V_{RHE}, and 1.0 V_{RHE}.

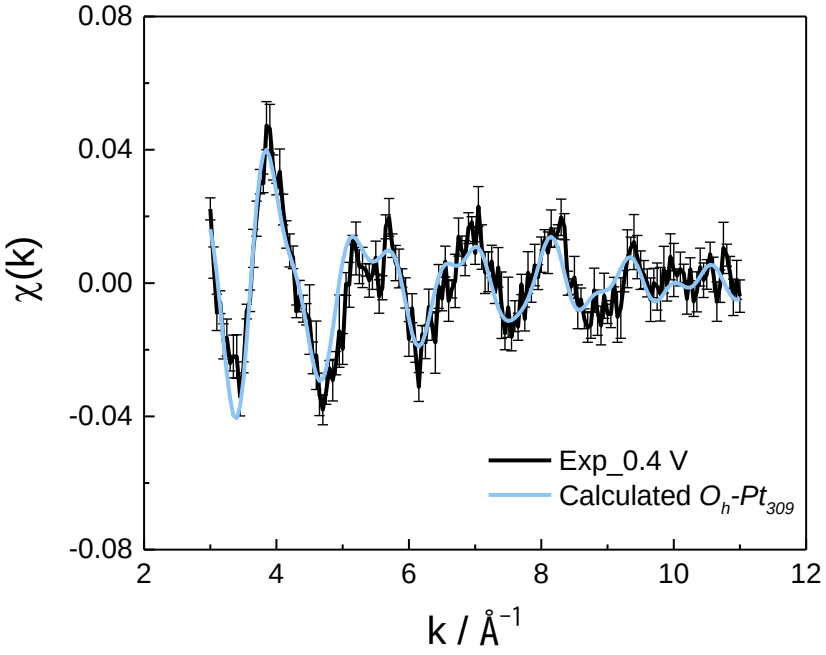

Figure 3-8. Fitting spectra based on O_h-Pt_{309} model for simulation at 0.4 V_{RHE}. Pt-Pt bond length is set as 2.76 Å, DW=-0.09 Å, S_0^2 = 1.0, CN = 9.6. The colored solid lines are observed EXAFS spectra with error bars, and the black solid line is the calculated EXAFS spectrum for the Pt NPs/HOPG model catalyst system.

Table 3-1. Fitting result based on O_h-Pt_{309} model for theoretical simulation at 0.4 V_{RHE}

	CN	Pt-Pt distance / Å	Debye-Waller factor/ $Å^2$
Pt foil	(12)	2.76 ± 0.01	0.0036 ± 0.0004
O_h-Pt_{309}	(9.6)	2.76 ± 0.06	0.0080± 0.0050

Numeral in () are the fixed values.

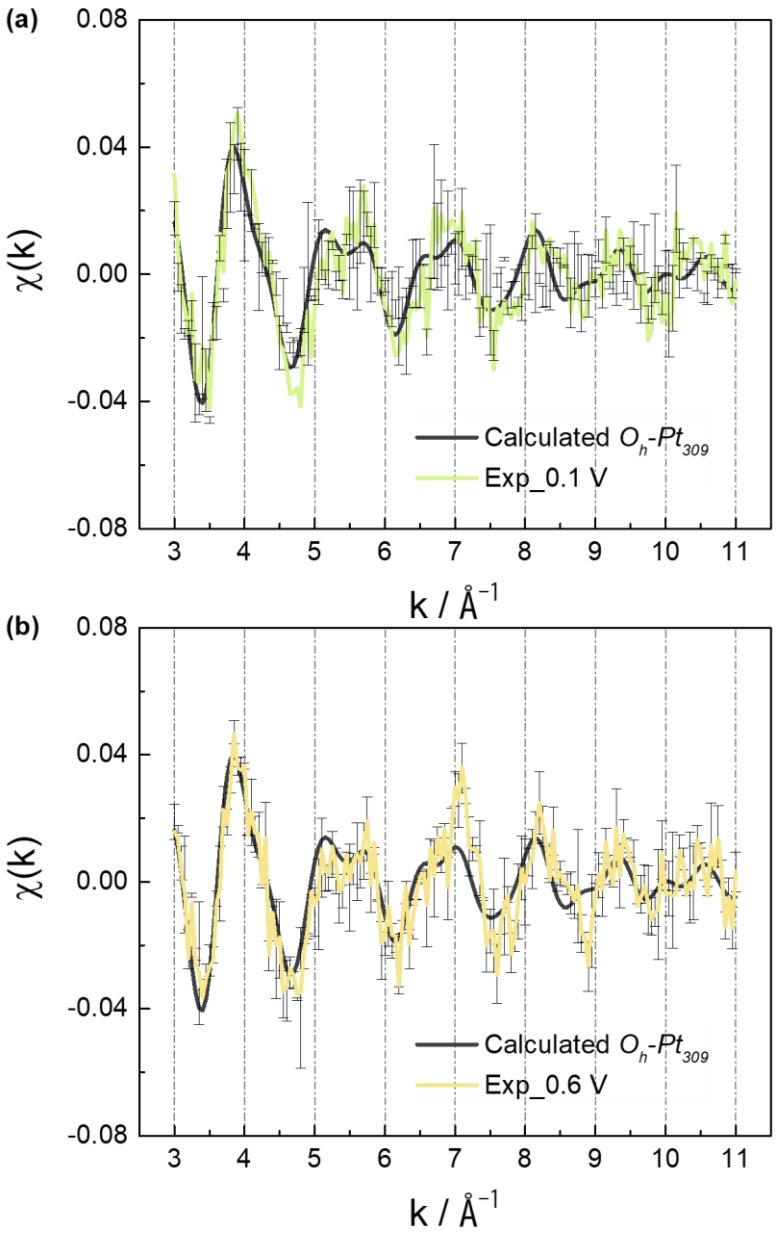
(a)
0.08
0.04
0.00
-0.04
-0.08
χ(k)
3
4
5
6
7
8
9
10
11
k / Å^{-1}
Calculated O_h-Pt_{309}
Exp_0.1 V
(b)
0.08
0.04
0.00
-0.04
-0.08
χ(k)
3
4
5
6
7
8
9
10
11
k / Å^{-1}
Calculated O_h-Pt_{309}
Exp_0.6 V

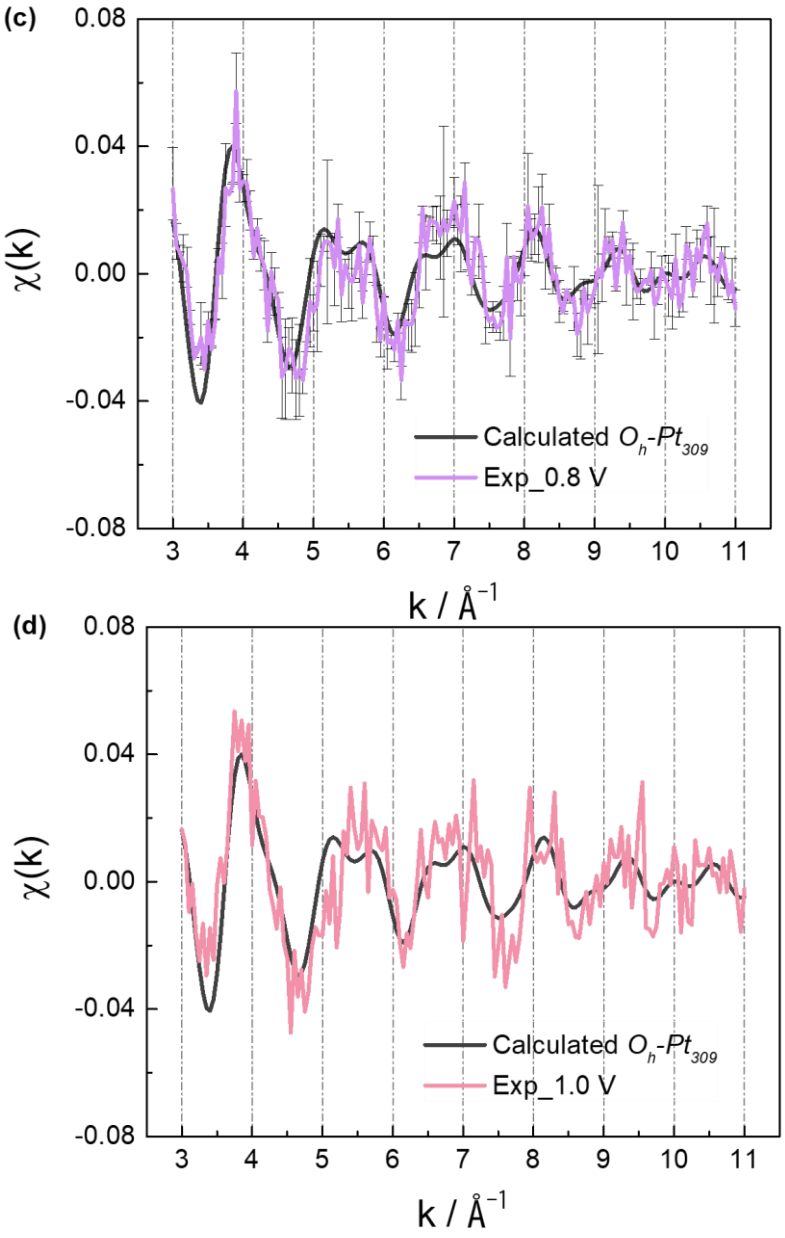

Figure 3-9. The fitting spectra based on Oh-Pt309 model for simulation potentials. Pt-Pt bond distance is set as 2.76 Å, DW=0.09 Å, S_0^2 = 1.0, CN = 9.6. Colored solid lines are observed EXAFS spectra with error, the black solid line is the calculated EXAFS spectra for Pt/HOPG model catalyst.

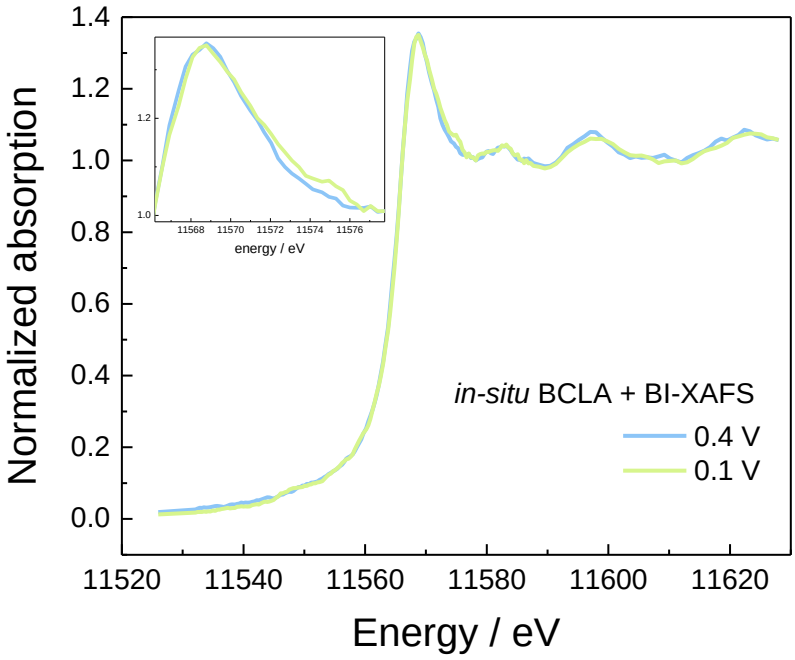

Figure 3-10. *In-situ* XANES spectra for Pt NPs/HOPG at 0.4 V_{RHE} and 0.1 V_{RHE}. Inserted picture is enlarged picture near absorption peak.

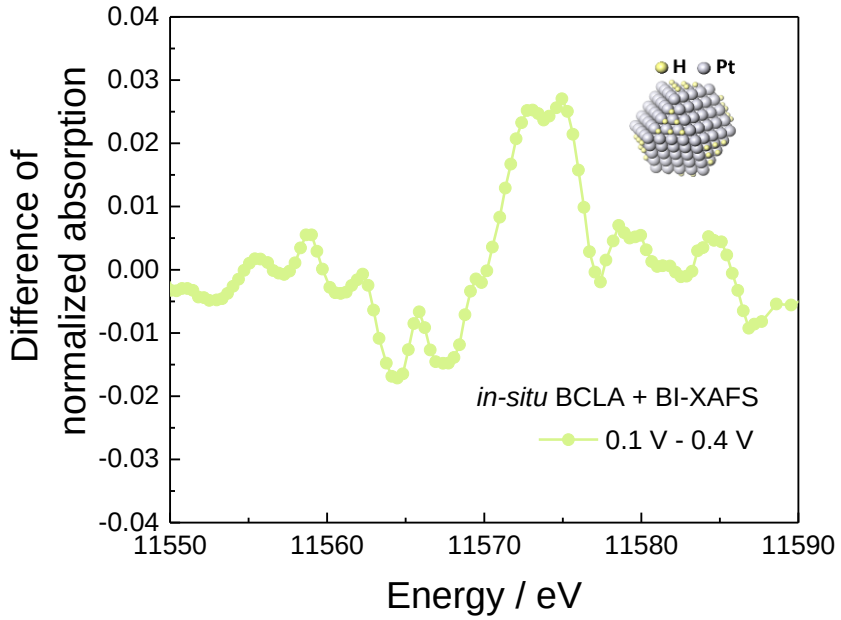

Figure 3-11. Difference spectra at 0.1 V_{RHE}. 0.4 V_{RHE} was used as reference potential. Insert picture is H adsorption on Pt fcc sites.

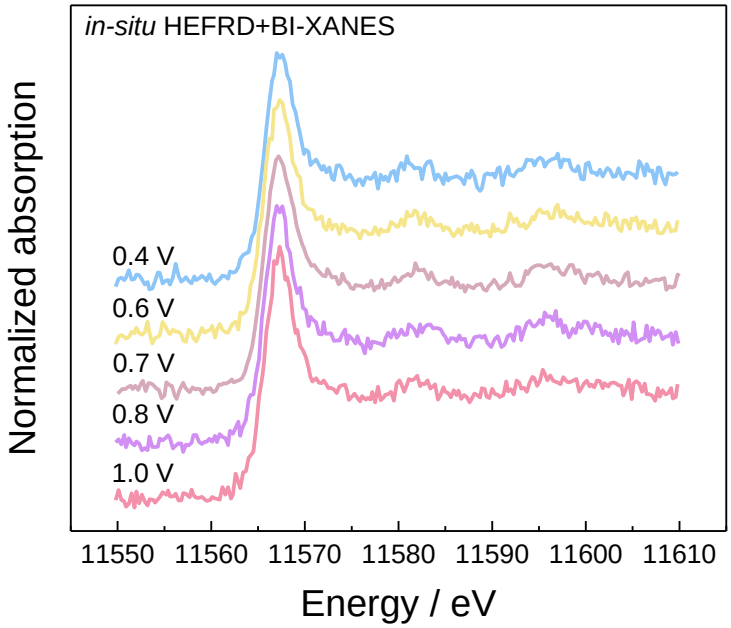

Figure 3-12. *In-situ* HERFD-BI-XANES spectra for Pt NPs/HOPG model catalyst at potentials.

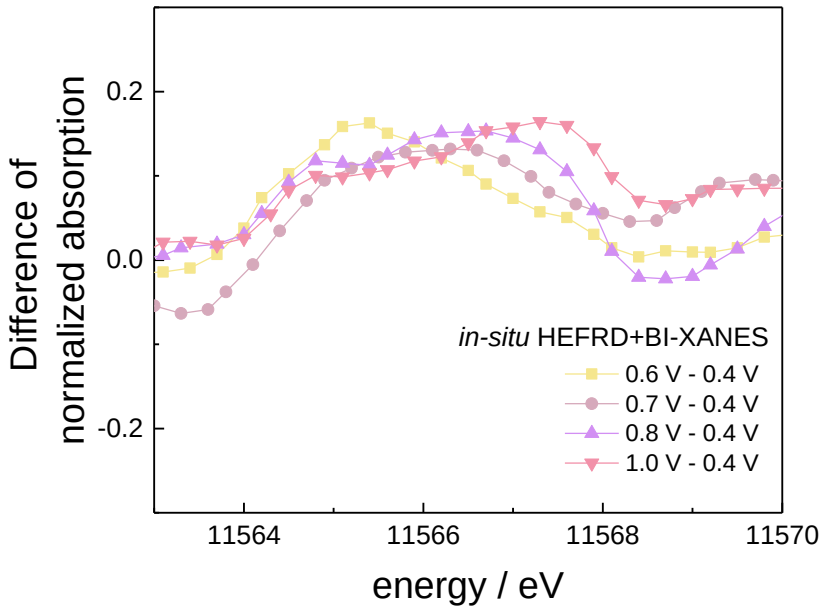

Figure 3-13. Difference HERFD-BI-XANES spectra for Pt NPs/HOPG at more positive potentials. 0.4 V_{RHE} is chosen as reference potential.

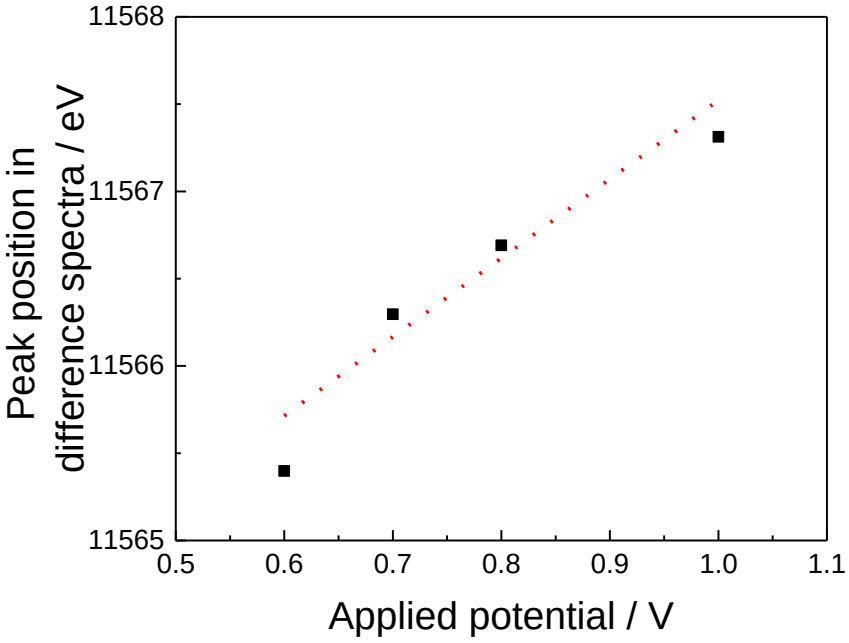

Figure 3-14. Peak position for difference spectra under potentials.

Reference

[1] H. Liu, M. Chen, F. Sun, S. Zaman, M. Wang, H. Wang, ACS Appl. Mater. Interfaces 14 (2022) 13891–13903.

[2] X. Liu, X. Wan, X. Tan, H. Yang, Y. Yang, J. Shui, X. Wang, J. Mater. Chem. A 9 (2021) 21051–21056.

[3] A.S. Nair, B. Pathak, J. Phys. Chem. C 123 (2019) 3634–3644.

[4] Y. Xiao, W. Zhang, Electrocatalysis 11 (2020) 393–404.

[5] Y. Xiao, W. Zhang, SN Appl. Sci. 2 (2020) 194.

[6] S. Takao, O. Sekizawa, G. Samjeské, T. Kaneko, K. Higashi, Y. Yoshida, X. Zhao, T. Sakata, T. Yamamoto, T. Gunji, T. Uruga, Y. Iwasawa, ACS Applied Materials & Interfaces 10 (2018) 27734–27744.

[7] K. Higashi, G. Samjeské, S. Takao, T. Kaneko, O. Sekizawa, T. Uruga, Y. Iwasawa, Journal of Physical Chemistry C 121 (2017) 22164–22177.

[8] P.L.J. Gunter, J.W. Niemantsverdriet, F.H. Ribeiro, G.A. Somorjai, Catalysis Reviews-Science and Engineering 39 (1997) 77–168.

[9] A. Singh, K. Miyabayashi, RSC Advances 10 (2020) 362–366.

[10] B. Lu, D. Kido, Y. Sato, H. Xu, W.-J. Chun, K. Asakura, S. Takakusagi, Journal of Physical Chemistry C 125 (2021) 12424–12432.

[11] Q. Yuan, S. Takakusagi, Y. Wakisaka, Y. Uemura, T. Wada, H. Ariga, K. Asakura, Chemistry Letters 46 (2017) 1250–1253.

[12] Y. Tanizawa, T. Shido, W.-J. Chun, K. Asakura, M. Nomura, Y. Iwasawa, Journal of Physical Chemistry B 107 (2003) 12917–12929.

[13] K. Asakura, W.-J. Chun, M. Shirai, K. Tomishige, Y. Iwasawa, Journal of Physical Chemistry B 101 (1997) 5549–5556.

[14] H. Uehara, Y. Uemura, T. Ogawa, K. Kono, R. Ueno, Y. Niwa, H. Nitani, H. Abe, S. Takakusagi, M. Nomura, Y. Iwasawa, K. Asakura, Physical Chemistry Chemical Physics 16 (2014) 13748–13754.

[15] Y. Zhang, F. Lu, S. Liu, D. Lu, M. Liu, Y. Zhang, P. Liu, J.X. Wang, R.R. Adzic, O. Gang, 85 (2018) 93–110.

[16] Y. Wakisaka, D. Kido, H. Uehara, Q. Yuan, F.E. Feiten, S. Mukai, S. Takakusagi, Y. Uemura, T. Yokoyama, T. Wada, M. Uo, O. Sekizawa, T. Uruga, Y. Iwasawa, K. Asakura, Chemical Record 19 (2019) 1157–1165.

[17] Y. Wakisaka, B. Hu, D. Kido, H.A. Rashid, W. Chen, K. Dong, T. Wada, B. Bharate, Q. Yuan, S. Mukai, Y. Takeichi, S. Takakusagi, K. Asakura, Journal of Synchrotron Radiation 27 (2020) 1618–1625.

[18] F.E. Feiten, S. Takahashi, O. Sekizawa, Y. Wakisaka, T. Sakata, N. Todoroki, T. Uruga, T. Wadayama, Y. Iwasawa, K. Asakura, Physical Chemistry Chemical Physics 22 (2020) 18815–18823.

[19] B. Hu, B. Bharate, Juan D. Jimenez, J.A. Lauterbach, N. Todoroki, T. Wadayama, K. Higashi, T. Uruga, Y. Iwasawa, Hiroko Ariga-Miwa, S. Takakusagi, K. Asakura, Journal of Physical Chemistry C (2022).

[20] Z. Paál, R. Schlögl, G. Ertl, Faraday Transactions 88 (1992) 1179–1189.

[21] Y. Iwasawa, X-Ray Absorption Fine Structure for Catalysts and Surfaces, (1996).

[22] J.J. Rehr, R.C. Albers, Rev. Mod. Phys. 72 (2000) 621–654.

[23] S. Rudi, L. Gan, C. Cui, M. Gliech, P. Strasser, Journal of The Electrochemical Society 162 (2015) F403.

[24] Y. Kang, J.B. Pyo, X. Ye, R.E. Diaz, T.R. Gordon, E.A. Stach, C.B. Murray, ACS Nano 7 (2013) 645–653.

[25] N. Watari, S. Ohnishi, Phys. Rev. B 58 (1998) 1665–1677.

[26] F. Baletto, R. Ferrando, Rev. Mod. Phys. 77 (2005) 371–423.

[27] K. Asakura, T. Kubota, N. Ichikuni, Y. Iwasawa, Studies in Surface Science and Catalysis 101 (1996) 911–919.

[28] K. Asakura, T. Kubota, W.-J. Chun, Y. Iwasawa, K. Ohtani, T. Fujikawa, Journal of Synchrotron Radiation 6 (1999) 439–441.

[29] T. Kubota, K. Asakura, N. Ichikuni, Y. Iwasawa, Chemical Physics Letters 256 (1996) 445–448.

[30] E.M. Erickson, M.S. Thorum, R. Vasić, N. Marinkovic, A.I. Frenkel, A.A. Gewirth, R.G. Nuzzo, Journal of the American Chemical Society 134 (2012) 197–200.

[31] D. Friebel, D. Miller, C.P. O'Grady, T. Anniyev, J.R. Bargar, U. Bergmann, H. Ogasawara, K.T. Wikfeldt, L.G.M. Pettersson, A. Nilsson, Physical Chemistry Chemical Physics 13 (2011) 262–266.

[32] M. Teliska, W.E. O'grady, D.E. Ramaker, Journal of Physical Chemistry B 109 (2005) 8076–8084.

[33] S. Mukerjee, S. Srinivasan, M.P. Soriaga, J. McBreen, Journal of The Electrochemical Society 142 (1995) 1409–1422.

[34] A. Bianconi, M. Dell'Ariccia, A. Gargano, C.R. Natoli, (1983) 57–61.

CHAPTER 4 Development of *in-situ* (P)TRF-XAFS and Feasibility of BCLA for Bimetallic Pt_{subML}/Au(111) Model Catalyst System Structure Investigation

The monometallic noble metal containing catalysts, such as Pt, Pd or Ru, etc. showed good catalyzing performance. However, the scarcity and high price of the noble metals greatly limited the large-scale commercial application of the fuel cells system. In addition, harsh operation conditions for real working conditions of fuel cells leads to the deactivation by poisoning, migration and aggregation, or the loss of monometallic noble metals during the carbon supports corrosion processes, which eventually cause the irreversible degradation of the entire battery. Therefore, attention turns to seeking low-cost, easy access, high-performance and good tolerance catalysts. In the past two decades, the tendency in fuel cell catalysts filed became the development of bimetallic catalysts with two different metal elements or compounds as active ingredients. This research trend showed a superior catalytic performance and durability than monometallic catalysts systems because of synergistic effects between the bimetallic species, which contributes to the binding strength of the reactant molecules on the surface-active sites though the synthesis of bimetallic catalysts are often more complex than that of monometallic catalysts[1]. For example, several kinds of PtAu nanostructures were explored, including core@shell particles[2–4], nanowires/nanorods/nanodendrites[5–7], star-or flower-shaped ones[8], superlattice arrays[9] and so on. With such diverse structures, varied performance were expected accordingly. It was reported that appropriate Au modification increased the oxidation potential of Pt, protected the surface-active sites from corrosion, and modulated the oxygenate intermediates adsorption processes. For example, Au was assumed to be more stable than Pt species from aspect of electronegativity or electrochemical potential[10,11], which was expected to assist Pt by improving the stability against oxidation in acidic media at high potentials. To the contrary, some researchers proposed that Au

possess a lower surface energy than Pt[12], therefore, Au atoms tend to segregate onto the electrocatalyst surface to occupy the Pt active sites, which further decrease the PtAu bimetallic system catalytic activity[13]. In addition, due to the lattice difference between Pt and Au, epitaxial growth of Pt onto Au surfaces lead to a tensile strain for Pt, which can cause stronger binding strength for surface Pt and adsorbed OH and O[10], while Kaito and co-workers [14] reported PtAu core-shell structures showed an enhanced ORR activity with a decreased Pt-Pt bond distance. The latter result agreed with the experimental results of Adzic[15], Mukerjee[16], and Shao's[17] works. In summary, the real mechanism of PtAu bimetallic electrocatalysts toward ORR are still under discussion. A rational discussion on PtAu electrocatalysts structures at molecular level or atomic scale and corresponding activity are necessary.

As with any catalysts, it is crucial to observe the catalyst surface structure variation under real reaction conditions, which allows to follow the dynamics of the structures to further understand the catalytic performance by applying *in-situ* structure investigation techniques. *In-situ* XAFS measurement under real operating conditions helps in distinguishing individual roles in bimetallic catalysts, particularly when combined with Density Function Theory (DFT). As mentioned in Chapter 3, one of the most significant issues concerning the *in-situ* EC-XAFS measurement is the scattering from the solution, which inhibited the fluorescence signals greatly. The successful application of the BCLA effectively remove the electrolyte induced undesired scattering signals which further increases the S/B ratio. In addition, the PtM alloy catalysts supported by carbon are usually in an inhomogeneous state or an possess ill-defined surface, which gives an averaged structure information instead of showing detailed structure like interactions between Pt and M metal, or the adsorbates effect on a specific metal. Model catalyst systems containing well-defined surface can solve this problem by applying flat substrates. Within this, new challenges comes to

the fore, how to prepare a homogeneously dispersed Pt-containing bimetallic model catalyst? How to practically apply XAFS technique to obtain the structure information for PtM bimetallic model catalyst systems under *in-situ* conditions?

The combination of application of a well-defined single crystal Au (111) and electrochemical deposition method of UPD+SLRR made it possible to obtain 2D Pt species on Au (111) and used as model catalysts for PtAu bimetallic catalyst structure investigation, especially for the discussion about the Pt-Pt bond distance variation after Pt subML directly deposited on Au(111). Furthermore, given the successful experience in applying BCLA in *in-situ* BI-XAFS measurement, this chapter focus on illustrating the feasibility of BCLA in structure investigation for Pt_{subML}/Au(111) model catalyst system with combination of *in-situ* EC-PTRF-XAFS techniques.

4.1 Limitation of existing XAFS Apparatus and Development of *in-situ* Electrochemical Bent-crystal *Laue* Analyzer assisted Total Reflection Fluorescence XAFS

For *in-situ* structure investigation of bimetallic Pt-based model catalyst systems using well-defined single crystals, the sample possess several properties:

1. As a well-defined flat substrate of single crystal is used, the surface area for target element deposition is very limited, usually only in 1 ML.
2. A single crystal with a certain thickness is necessary for sample fixing on the EC-XAFS cell, which inhibited the application of traditional transmission XAFS application because the X-ray cannot penetrate the sample. In this realm, the BCLA+BI-XAFS method introduced in Chapter 3 cannot be applied either because the X-ray cannot be detected from the backside of the sample due to the thickness limitation.

Fluorescence XAFS detection can be applied to the diluted system to increase the sensitivity of XAFS measurement, while a special setup configuration should be considered to overcome the above-mentioned problems. Considering the limited target element amount and flat surface properties, a total reflection detection mode was adopted. When the incident angle is less than the critical angle, the total reflection occurs, where the X-ray doesn't have to penetrate the bulk deeply. For BCLA assisted EC-XAFS apparatus development applied for *in-situ* bimetallic catalyst system structure investigation, several concepts should be followed:

1. The *in-situ* structure investigation requires acidic electrolyte appearance and allows potential controls corresponding to the real ORR reaction conditions.
2. To avoid the possibilities of sample oxidation, the solution and whole cell should be protected from air contamination by inert gas.
3. To apply total reflection measurement condition and challenge XAFS measurement, a multi-axis goniometer for fine position adjustment of *in-situ* EC-XAFS cell is necessary. In addition, the cell should be flexible to adjust the solution thickness for different circumstances. For example, thick solution layer for effective mass transportation and ultrathin solution layer for eliminating the electrolyte caused scatterings during XAFS measurement.

Figure 4-1 shows the schematic diagram of the *in-situ* BCLA assisted EC-TRF-XAFS system set in BL15A1, Photon Factory in KEK, Japan. The X-ray emitted from undulator was monochromated by a Si (111) double crystal monochromator, which was further focused by a bent mirror, with a spot size of 0.1 mm in the vertical direction. The X-ray intensity was monitored by an I_0 ionization chamber filled with N_2. The fluorescence signal was detected by a 7-element SDD (Techno-Ap, Tsukuba, Japan). The *in-situ* EC-XAFS cell was placed right in front of the detector.

A home-made BCLA with an energy resolution estimated to be 30 eV was placed between the EC-XAFS cell and the detector. A schematic of home-made BCLA is shown in Figure 4-2. The design principle of BCLA follows: the thin Silicon crystal is bent to the logarithmic spiral shape by the side frame, the beams are also positioned with a logarithmic spiral configuration. To reduce the diffraction loss by the beams, the beams are set at the Mo *Soller* slit positions. The BCLA can be expressed as $r = \rho_0 \cos(\chi - \theta_B) \exp(\tan(\chi - \theta_B)\,\theta)$ with the curvature of ρ_0 = 100 mm and χ (asymmetry angle) = 19.5 °, where r is the radial vector from the focal point on the sample, θ_B is the Bragg angle. Figure 4-3 shows the working principle of BCLA. To obtain maximum fluorescence signals, BCLA position should be carefully adjusted. Within this configuration, n is the normal vector to the crystal surface. The angle between the two vectors n and r is the same along the white curve on the crystal. The white curve is the intersectional curve of the BCLA crystal surface, and the plane created by n, r, and the focal point. The focal point of the BCLA crystal surface is shown as the blue line on the sample. When the X-ray footprint and focal line agree, the whole BCLA can accept X-rays with a constant wavelength. The placing of BCLA to sample can be considered as follows, as shown in Figure 4-4. When the BCLA is set parallel to the X-ray beams, in case of 45° incidence, BCLA can only accept a small amount of X-ray fluorescence coming from the long footprint (redline). However, once the BCLA is placed parallel to the sample surface, the BCLA receives the fluorescence X-rays more effectively if the BCLA focal line and X-ray footprint agrees.

The EC-TRF-XAFS cell is fixed to a 6-axis goniometer ($x, y, z, \theta, \phi, \psi$) placed in the hutch of the beamline, which enables the optimization of the total reflection condition for the incident X-rays. Figure 4-5 shows the configuration of goniometer for *in-situ* EC-XAFS measurement. Figure 4-6 shows the details of EC cell used for *in-situ* XAFS measurement. The cell body was made of

polychlorotrifluoroethylene (PCTFE), which possess high mechanical strength and anti-acid properties. The cell body was drilled for two pairs of holes, one pair for electrode, held by glassy holders, and the other pair for solution in-let and out-let, respectively. Pt foil was used as CE in in-situ XAFS measurement, RHE was used as reference electrode (RE). The sample was firmly fixed on a specific stage made of Au materials to ensure a well conduction between the sample and the cell body. After confirmed the connections, the cell body was sealed by the mylar film with a thickness of 2.5 μm, which has an extraordinary ductility, and a cell cover, which was made of Teflon materials and sealed with Kapton films. This construction can protect the sample from outside oxygen contamination. Before XAFS measurement starts, the sample is lowered down with a thick electrolyte layer appearing above the sample to ensure the effective mass transportation. A certain potential should be applied to the sample for corresponding chemical reactions occurring. During the XAFS measurement, the sample is lift, only left a thin electrolyte layer ~ a few micrometers. This thin electrolyte layer preserves the *in-situ* electrochemical conditions during XAFS measurement while avoid tremendous scattering signals created within the liquid phase at the same time, which effectively reduce the scattering effect to improve the S/B ratio.

4.2 Sample preparations, surface characterizations, and *in-situ* EC-TRF-XAFS measurement

4.2.1 Sample Preparations

A thin Pt layer was deposited on a 60 nm-thick polycrystalline Au thin film evaporated on a 10 mm × 20 mm Si(100) wafer by self-terminating electrodeposition method as described in the Wakisaka et al.[18] reported paper. The Pt coverage was estimated as 1 ML by XPS. This sample is termed as Pt/Au/Si. In addition, a self-deposition (SD) method prepared Pt_{subML}/Au(111) model catalyst system was also prepared for the BCLA feasibility investigation. Perchloric acid (60%), H_2SO_4 (98%), NaCl (99.98%) and $H_2PtCl_6 \cdot 6H_2O$ was purchased from Wako Pure Chemicals.

Ultrapure water (UPW, 18.2 MΩ, Milli-Q, Merck Millipore Co) was used for the preparation of aqueous solutions as well as for rinsing. The Au(111) single crystals used in this work were disks with a diameter of 15 mm and a thickness of 5 mm (SPL, The Netherlands). The treatment of Au(111) was described in Chapter 2. The well-treated sample as well as the N_2 purged solutions were transferred to the N_2 filled glovebox before the experiment. Figure 4-7 illustrates the SD process. The SD Pt on Au(111) was prepared by contacting the Au(111) surface with the 0.1 M $HClO_4$ + 1 mM H_2PtCl_6 solution to form a meniscus for 30 s at open circuit potential (OCP). Then, the Au(111) surface was quickly dipped into UPW and washed for 30 s to obtained the Pt-decorated Au(111), termed as SD-Pt/Au(111). The obtained SD-Pt_{subML}/Au(111)possess an homogeneously dispersed Pt species on Au(111) without aggregation, the Pt amount in SD-Pt_{subML}/Au(111) is estimated to be 0.1 ML.

4.2.2 In-situ BCLA+TRF-XAFS Measurement

The structure of the as-deposited SD-Pt/Au(111) was studied by EC-TRF-XAFS. The sample was loaded as the working electrode onto the stage of a home-made *in situ* EC-XAFS cell with 6 μm Mylar film (Chemplex Industries, Inc.) covered X-ray window. Ag/AgCl and Pt wires were used as RE and CE, respectively. Deaerated 0.1 M HClO4 was introduced into the cell via a piezoelectric pump (Bimor BPF, Nitto Kohki Co.). The cell was assembled in the N_2-filled glovebox and was mounted on a 5-axis goniometer which allowed to adjust polarization directions and total reflection conditions. The sample was always contacted to electrolyte and was kept at OCP. XAFS data analysis were performed using the REX 2000 program (Rigaku Co.)[19] and Feff8 simulation[20].

4.3 BCLA feasibility for Pt/Au/Si sample in BCLA+TRF-XAFS method

Due to the unique compositional property of bimetallic catalyst system of PtAu, where Pt and Au are neighboring atoms. The Pt Lα fluorescence is greatly hindered by the strong Au Lα_1 and Au Lα_2. Consequently, the selection of Pt Lα fluorescence signals from the strong Au Lα interference fluorescence signals is a crucial step for TRF-XAFS measurement at Pt L_3 edge. Figure 4-8 shows the energy analysis of the SDD output signals before and after the Au L_3 edge without vs with the BCLA for Pt/Au/Si sample without electrolyte. The red and black curve represent the incident X-ray energy before (11300 eV) and after (12100 eV) the Au edge. For incident X-ray energy before the Au edge, a clear peak with strong intensity locates around 9628 eV correspond to the Au Lα fluorescence signals. A small peak with weak intensity locates around 9442 eV is the Pt Lα fluorescence signal peak. However, when the BCLA is set between the sample and the SDD, Au Lα fluorescence signals could be removed as shown in the topmost inserted figure. In this realm, EXAFS spectrum could be obtained. Figure 4-9 shows the XAFS spectra measured without BCLA vs with BCLA and SDD. The Pt Lα fluorescence X-ray signal per second was reduced to 1/160 of that without the BCLA ($I_f/I_0 = 0.0024$ with BCLA, and $I_f/I_0 = 0.38$ without BCLA, respectively), while this level difference is reasonable because in case of BCLA application, the detector is pushed further away from the sample than case without BCLA application. In addition, the S/B ratio estimation by considering the background level at energy region around 11340 eV before the edge, and signal level at energy region around 11800 eV after the edge gave a value as 140 and 11000 in case of without vs with BCLA application. The background X-ray level was markedly reduced by the BCLA, which greatly reduced the detection limitation of TRF-XAFS.

In addition, the S/N ratio for TRF-XAFS measurement should be considered. Figure 4-10 shows the EXAFS oscillation for Pt/Au/Si sample with vs without BCLA application. The S/N ratio

without BCLA was comparable to that of with BCLA application. So far, it has been proved that the combination of BCLA and TRF-XAFS is possible.

4.4 BCLA feasibility for SD-Pt_{subML}/Au(111) model catalyst by *in-situ* BCLA+(P)TRF-XAFS method

To study the feasibility of BCLA under solution environment, *in-situ* EC-TRF-XAFS was carried out in the EC cell with a solution layer thickness of 1 mm and application of -0.16 $V_{Ag/AgCl}$ in 0.1 M $HClO_4$ solution. Figure 4-11 shows the collected XANES spectra. A clear edge jump and WL intensity were observed. In this regard, BCLA is applicable for diluted system structure investigation under *in-situ* condition. In addition, the application of *in-situ* EC-XAFS cell allows the CV scanning for SD-Pt_{subML}/Au(111) model catalyst, as shown in Figure 4-12, where the CV in EC-XAFS cell with a solution thickness ~ 1 mm was comparable to that in normal electrochemical treatment a thicker solution layer. Effective mass transportation is ensured for BCLA assisted *in-situ* TRF-XANES under electrochemical conditions.

The cell and goniometer configuration at p-polarization direction is as shown in Figure 4-5(b), which is used for interaction investigation between Pt planar layer structure and underlying Au(111) substrate. Figure 4-13 shows the EXAFS spectrum for SD-Pt_{subML}/Au(111) model catalyst system under solution environment. The data can be evaluated from the following three aspects:

1. The S/N ratio without BCLA application was comparable to that after BCLA application.
2. The bending feature at the post edge caused by the coming Au edge, was comparable without vs with BCLA application.
3. The S/B ratio at s-polarization direction can be estimated as the method described in Chapter 4.3. In case without BCLA application, the S/B ratio was estimated as 0.0025/0.00025=10. In case of BCLA applied, the S/B ratio gave a value of

0.00009/0.000001=90. The S/B ratio is not significantly differed as in Pt/Au/Si sample measurement without solution case, which means the BCLA didn't effectively reduce the negative effect cause by solution induced inelastic scatterings. The large inelastic scattering contributes too much for the background ratio, which cannot simply be eliminated or compensated by BCLA.

In short, despite the BCLA didn't improve the S/B or S/N effectively under the solution conditions for EXAFS measurement, the combination of BCLA and *in-situ* EC-PTRF-XAFS apparatus is possible. The investigation on Pt_{subML}/Au(111) electronic structure with 0.1 ML Pt under solution condition was successfully achieved.

4.4 Conclusion

It has been proven that the BCLA can also be applied in the model catalyst system structure investigation with combination of (P)TRF-XAFS method, where the application of BCLA helped markedly reduced the background signal and improved S/B ratio in model catalyst system with Pt concentration > 1 ML under no solution condition. In case of diluted system with Pt ~ 0.1 ML within solutions, BCLA didn't contribute so much as former case probably due to the far too strong inelastic scatterings coming from the solution layer that is hard to be eliminated effectively by BCLA. Further improvement should be considered to reduce the solution effect. In summary, this developed (P)TRF-XAFS method can be applied for bimetallic Pt-based model catalyst structure investigation even without BCLA application.

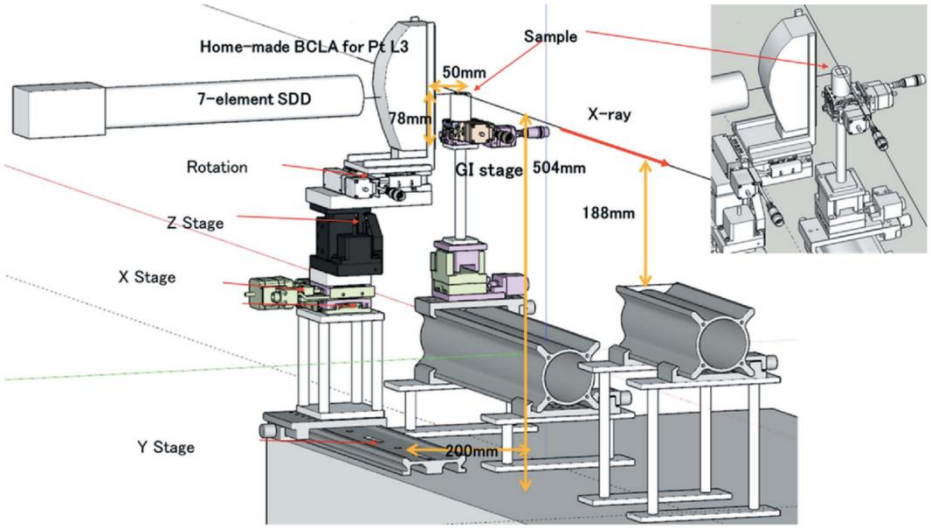

Figure 4-1. Schematic of the TRF-XAFS system. The incident X-rays come from the left side and the fluorescent X-rays are analyzed by BCLA. The BCLA is covered with a lead sheet, except for its entrance and exit windows. [18]

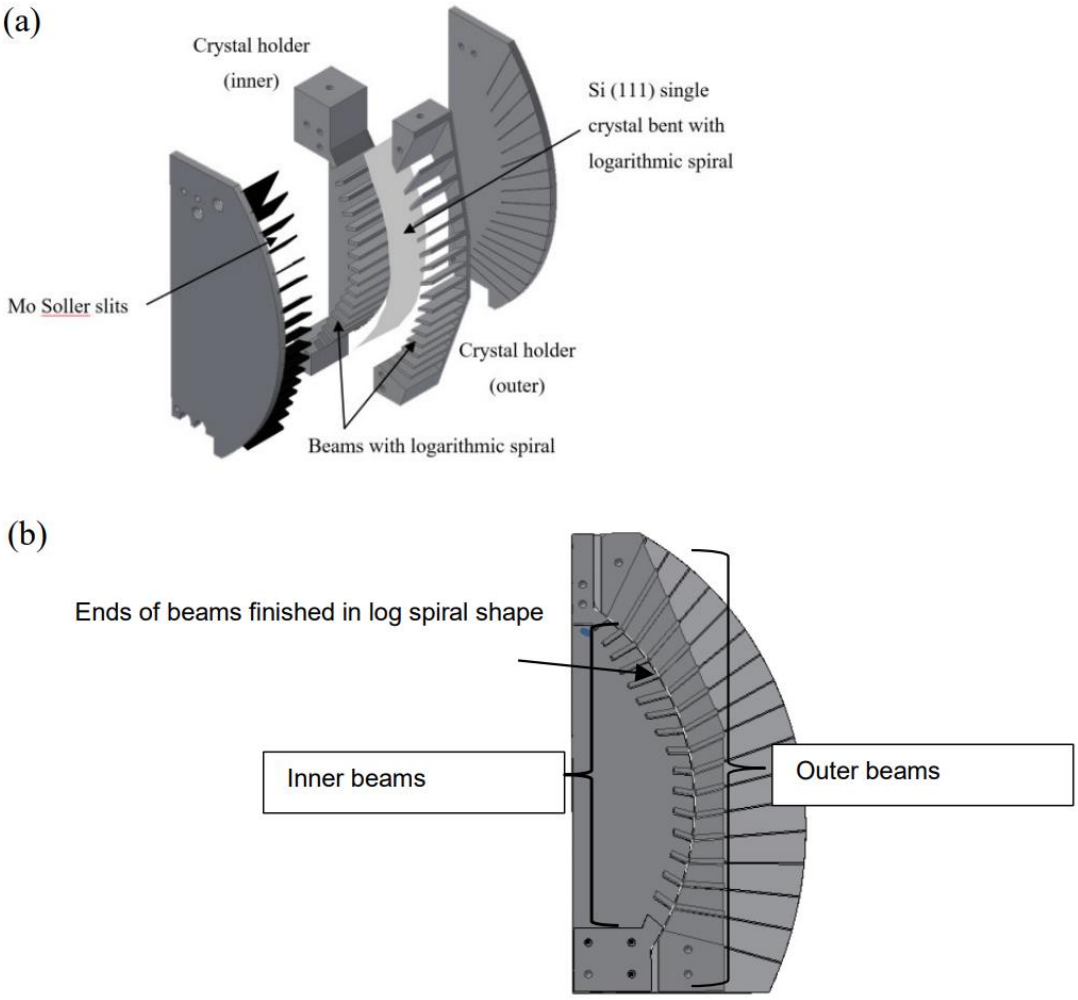

Figure 4-2. Home-made BCLA. (a) overall structures of home-made BCLA and (b)side view. The ends of the log-spirally shaped inner and outer beams sandwiched the thin Si crystal. [18]

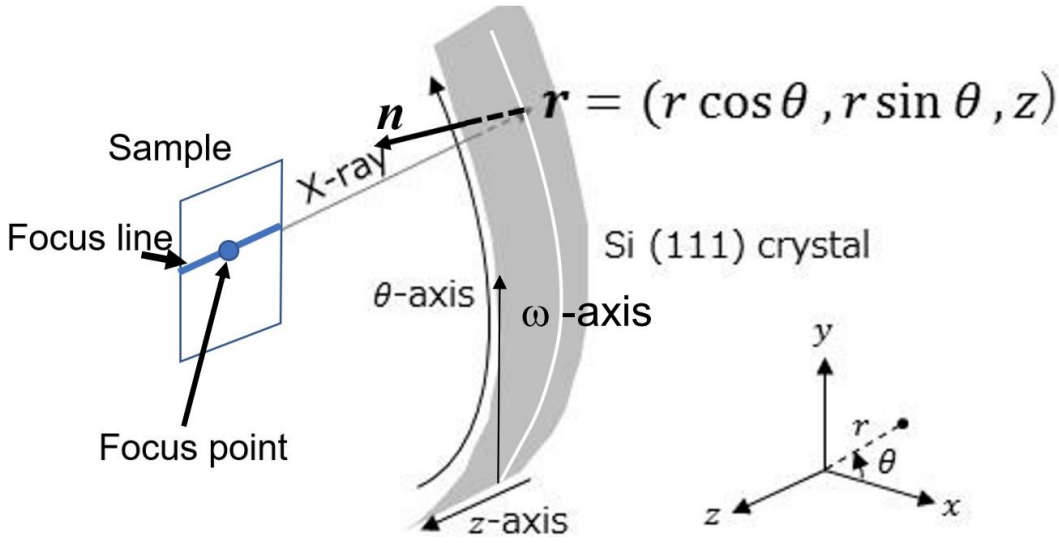

Figure 4-3. BCLA and focal point. [18]

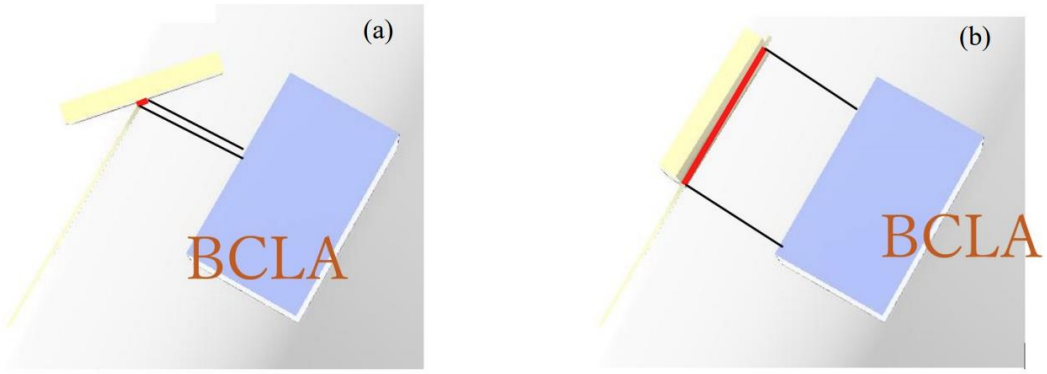

Figure 4-4. Relation between the sample and BCLA. (a) 45° incidence case. The BCLA is set parallel to the beam. (b) Grazing incident case. The BCLA is parallel to the surface. [18]

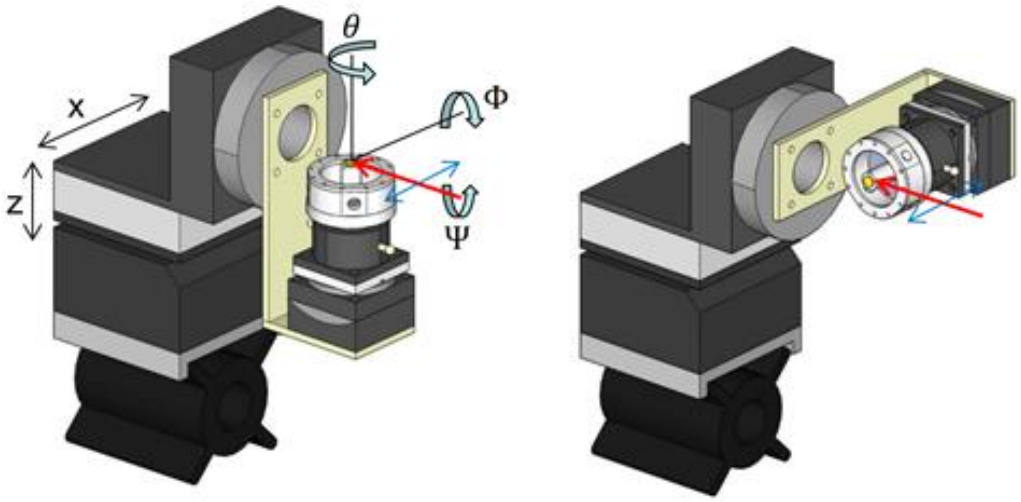

Figure 4-5. Schematic diagram for goniometer used in (P)TRF-XAFS cell position adjustment.

(a) s-polarization direction; (b) p-polarization direction.

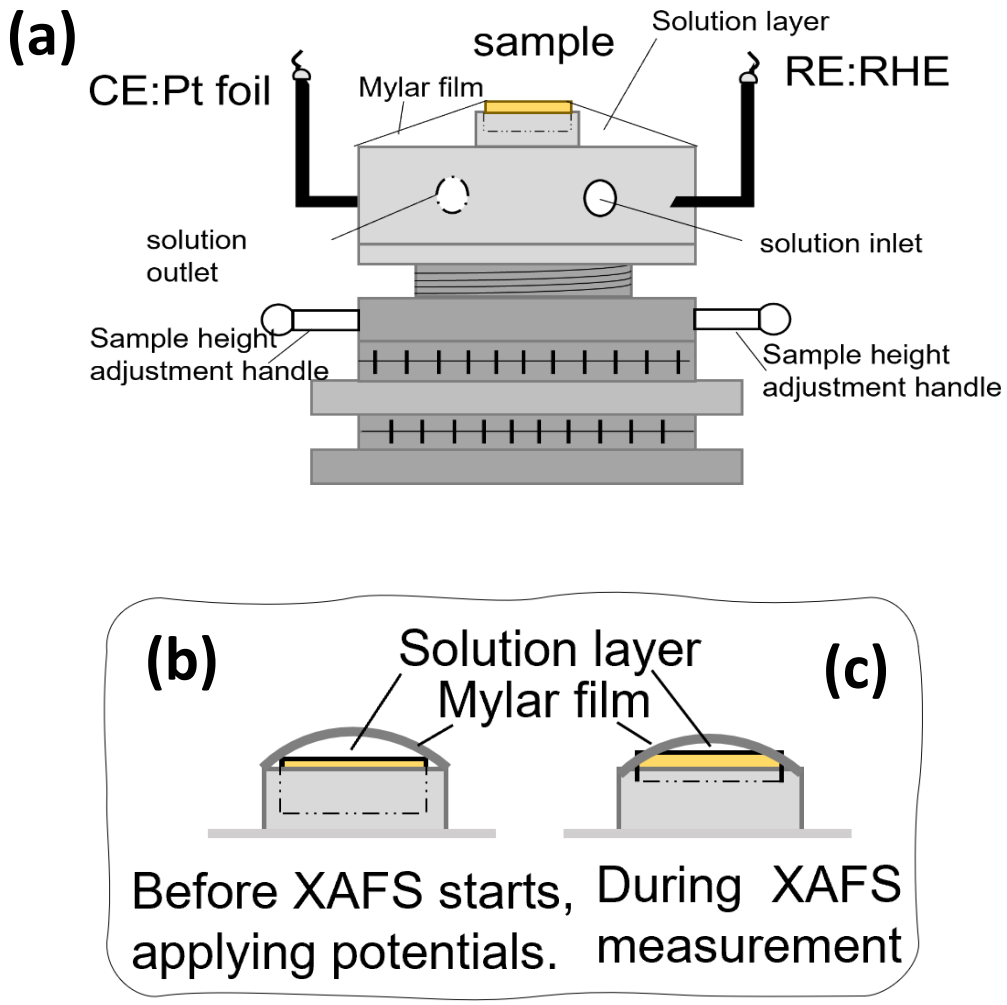

Figure 4-6. Schematic diagram for (a)EC-TRF-XAFS cell. (b) The sample is lowered down to have a thick solution layer for effective mass transportation. (c) The sample is pushed up to have a thin solution layer for in-situ EC-TRF-XAFS measurement.

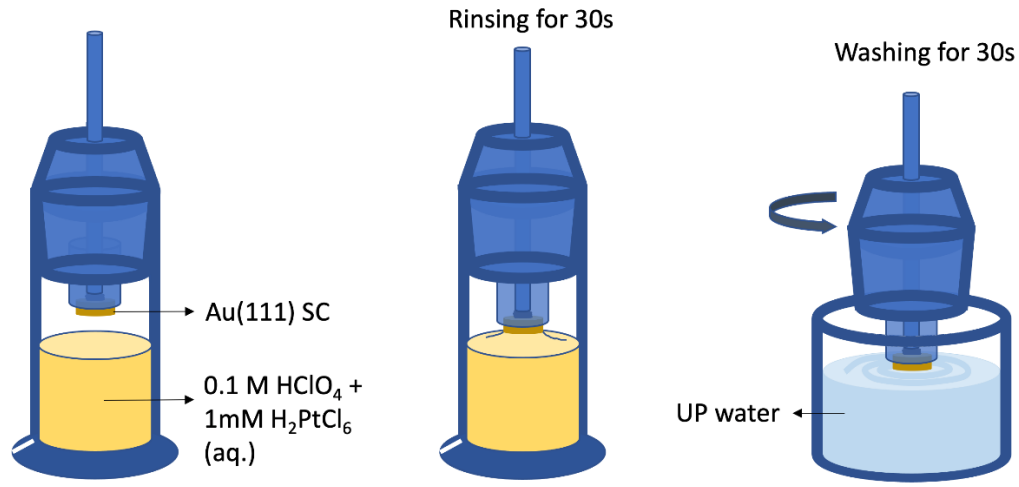

Figure 4-7. Schematic description of Pt spontaneous deposition (SD) process, carried out inside N_2-filled glovebox. Au(111) was first annealed by propane flame and induced into the glovebox. All solutions were deaerated before being put inside the glovebox.

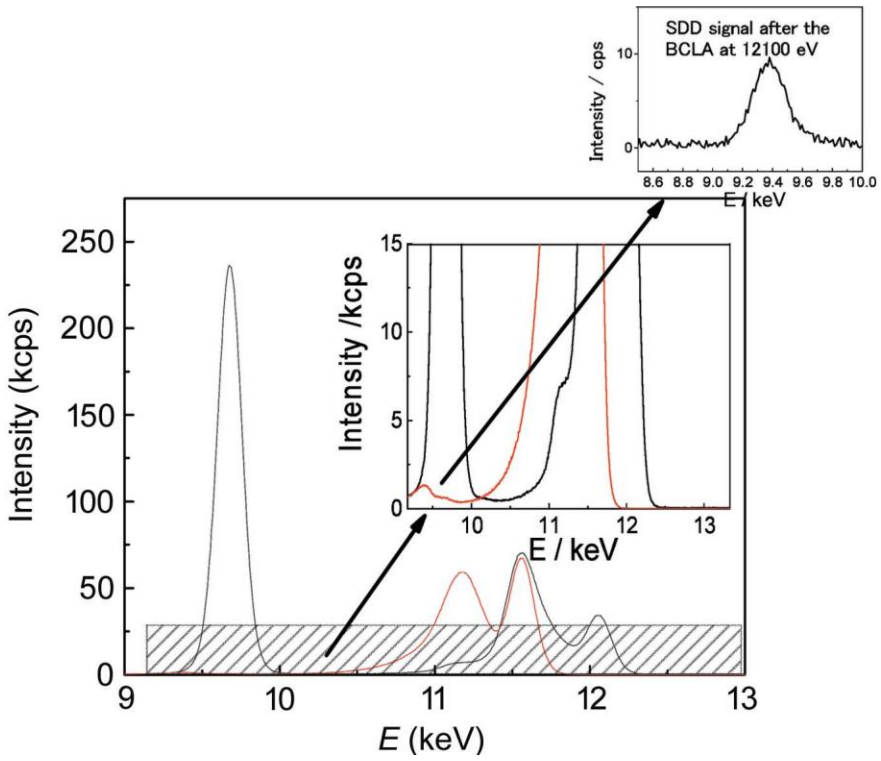

Figure 4-8. Spectra of X-rays detected by SDD. The red and black curves correspond to the incident X-ray energy before (11300 eV) and after (12100 eV) the Au edge, respectively. [18]

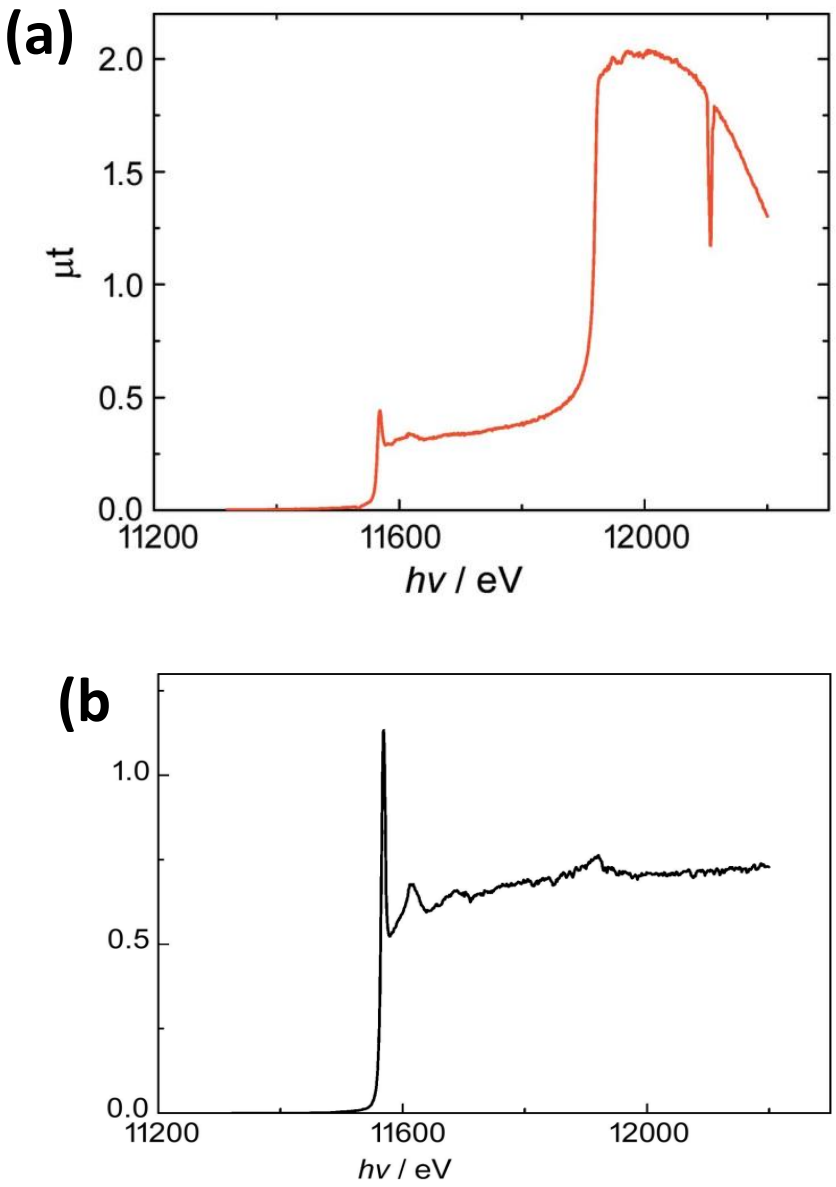

Figure 4-9. TRF-XAFS spectrum of Pt/Au/Si measured by SDD (a) without the BCLA vs (b) with the BCLA. The SDD energy window was set in the range 9.1–9.5 keV. For (a) 10s per points and (b) 60s per points accumulation for XAFS measurement. [18]

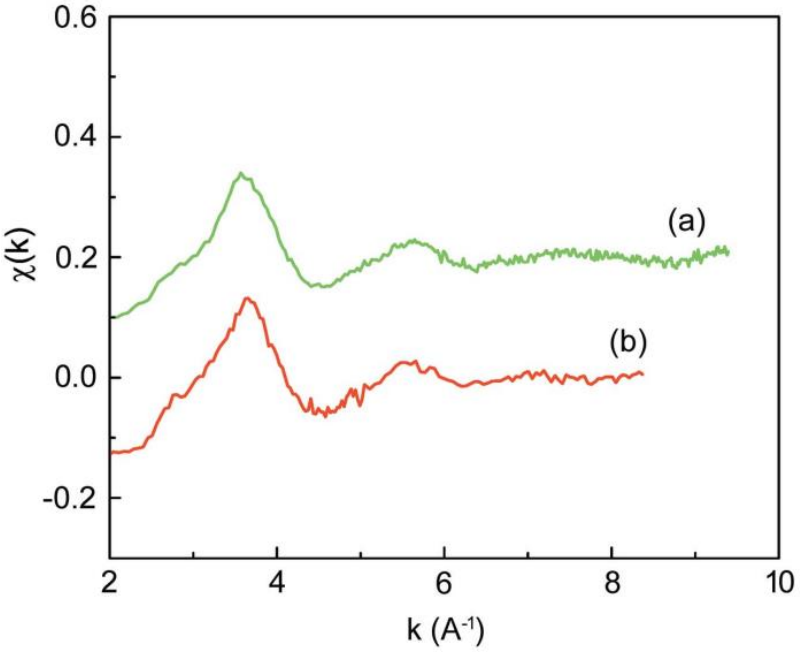

Figure 4-10. EXAFS oscillation for Pt/Au/Si (a) with and (b) without BCLA application. [18]

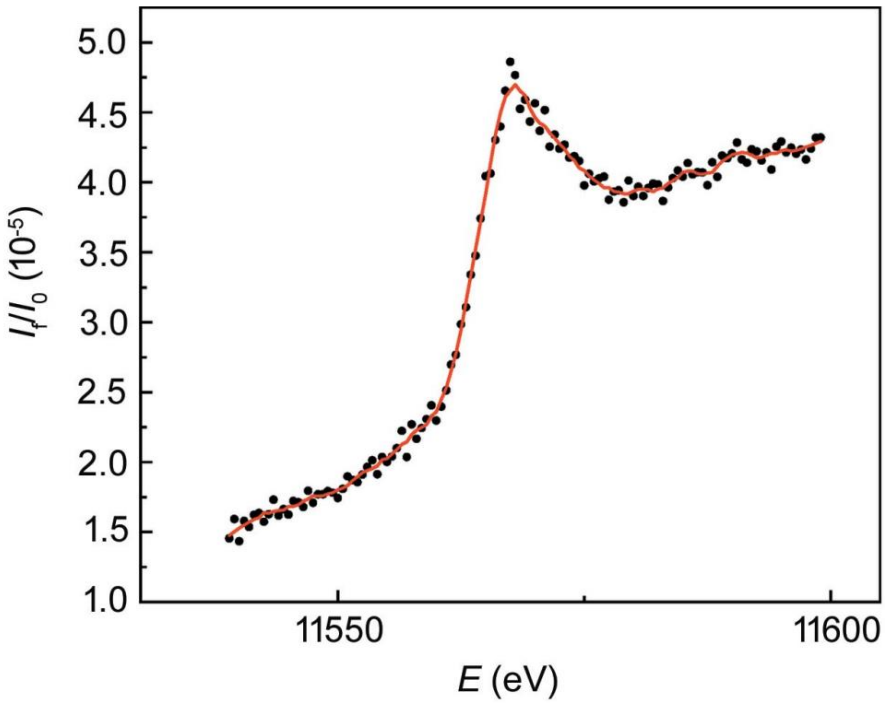

Figure 4-11. XANES spectra of 0.1 ML Pt on Au under -0.16 $V_{AgAg/Cl}$ in 0.1 M $HClO_4$. [18]

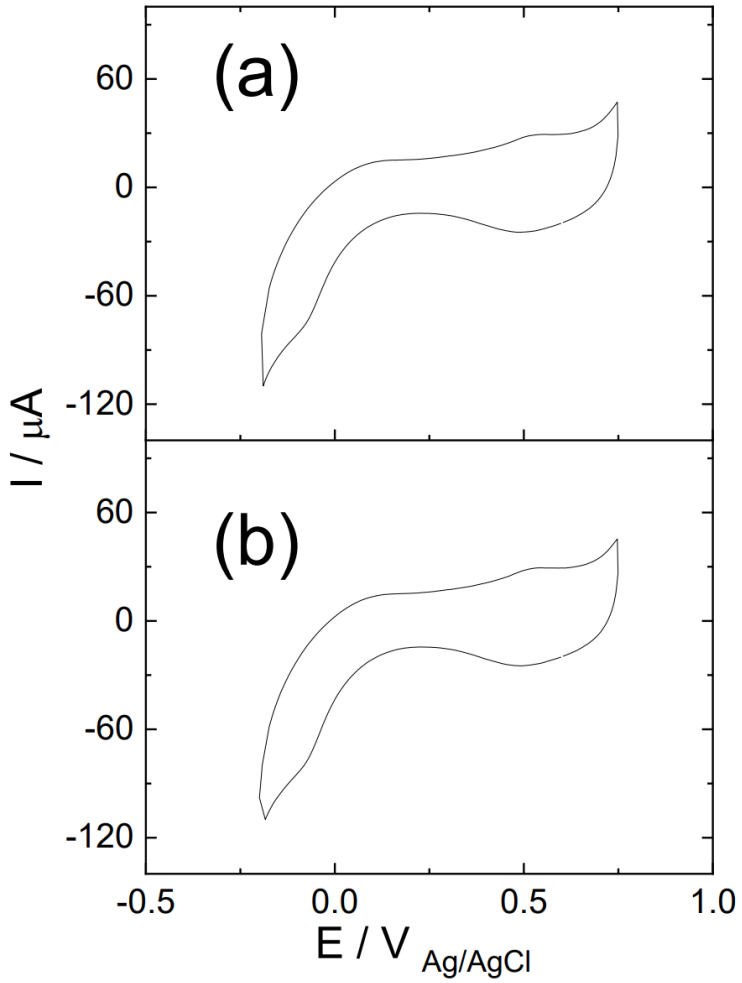

Figure 4-12. CV of SD-Pt_{subML}/Au(111) model catalyst in PTRF-XAFS cell. The distance between the sample surface and the mylar film is (a) 1 mm and (b) 3 mm. [18]

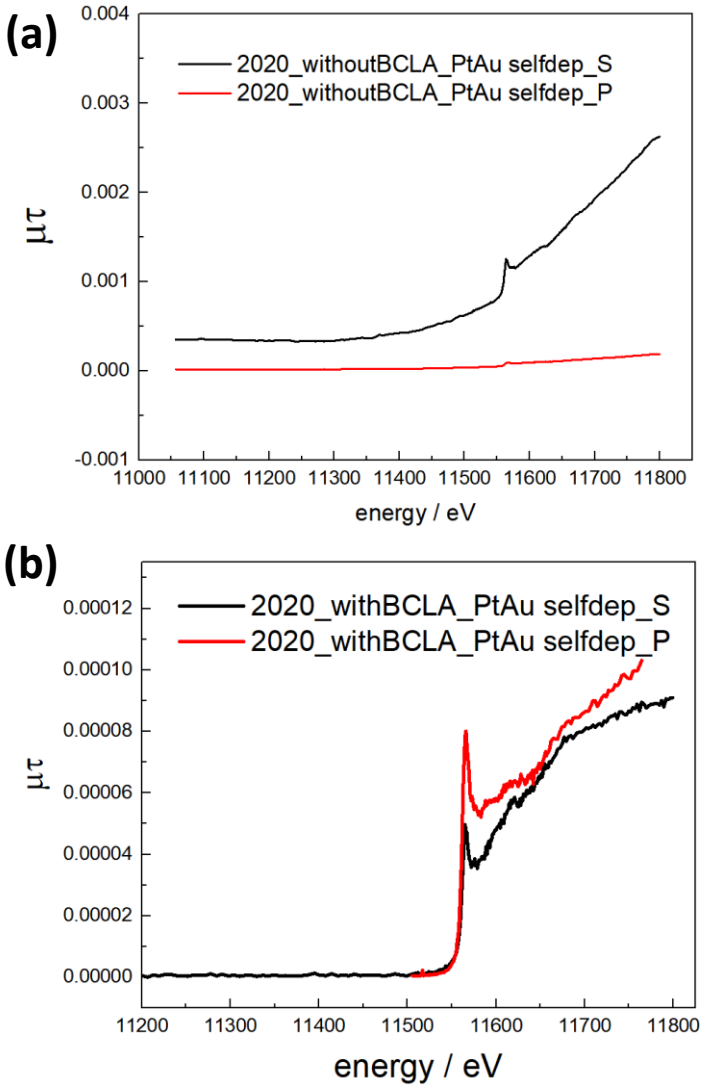

Figure 4-13. *In-situ* EC-PTRF-XAFS measurement for SD-Pt_{subML}/Au(111) sample (a) with and (b) without BCLA application, respectively. Black lines are raw data obtained at s-polarization, and p-polarization direction, respectively. Note that the XAFS spectrum without BCLA application and with BCLA was measured at BL15A, IMS-KEK-PF.

Reference

[1] K. Zhao, Y. Shu, F. Li, G. Peng, Green Energy & Environment 8 (2023) 1043–1070.

[2] L. Zhang, S. Yu, J. Zhang, J. Gong, Chemical Science 7 (2016) 3500–3505.

[3] Y. Dai, S. Chen, ACS Appl Mater Interfaces 7 (2015) 823–829.

[4] J. Hu, L. Wu, K.A. Kuttiyiel, K.R. Goodman, C. Zhang, Y. Zhu, M.B. Vukmirovic, M.G. White, K. Sasaki, R.R. Adzic, J. Am. Chem. Soc. 138 (2016) 9294–9300.

[5] L. Liu, L.-X. Chen, A.-J. Wang, J. Yuan, L. Shen, J.-J. Feng, International Journal of Hydrogen Energy 41 (2016) 8871–8880.

[6] Y.-T. Liang, S.-P. Lin, C.-W. Liu, S.-R. Chung, T.-Y. Chen, J.-H. Wang, K.-W. Wang, Chemical Communications 51 (2015) 6605–6608.

[7] X. Weng, Y. Liu, K.-K. Wang, J.-J. Feng, J. Yuan, A.-J. Wang, Q.-Q. Xu, International Journal of Hydrogen Energy 41 (2016) 18193–18202.

[8] T. Bian, H. Zhang, Y. Jiang, C. Jin, J. Wu, H. Yang, D. Yang, Nano Lett. 15 (2015) 7808–7815.

[9] J.-J. Feng, L.-L. He, R. Fang, Q.-L. Wang, J. Yuan, A.-J. Wang, Journal of Power Sources 330 (2016) 140–148.

[10] B. Hammer, J.K. Norskov, Nature 376 (1995) 238–240.

[11] A. Ruban, B. Hammer, P. Stoltze, H.L. Skriver, J.K. Nørskov, Journal of Molecular Catalysis A: Chemical 115 (1997) 421–429.

[12] L. Vitos, A.V. Ruban, H.L. Skriver, J. Kollár, Surface Science 411 (1998) 186–202.

[13] K. Sasaki, H. Naohara, Y. Choi, Y. Cai, W.-F. Chen, P. Liu, R.R. Adzic, Nat Commun 3 (2012) 1115.

[14] T. Kaito, H. Mitsumoto, S. Sugawara, K. Shinohara, H. Uehara, H. Ariga, S. Takakusagi, Y. Hatakeyama, K. Nishikawa, K. Asakura, J. Phys. Chem. C 118 (2014) 8481–8490.

[15] R.R. Adzic, J. Zhang, K. Sasaki, M.B. Vukmirovic, M. Shao, J.X. Wang, A.U. Nilekar, M. Mavrikakis, J.A. Valerio, F. Uribe, Top Catal 46 (2007) 249–262.

[16] S. Mukerjee, S. Srinivasan, M.P. Soriaga, J. McBreen, J. Phys. Chem. 99 (1995) 4577–4589.

[17] M. Shao, A. Peles, K. Shoemaker, M. Gummalla, P.N. Njoki, J. Luo, C.-J. Zhong, J. Phys. Chem. Lett. 2 (2011) 67–72.

[18] Y. Wakisaka, B. Hu, D. Kido, M.H. Al Rashid, W. Chen, K. Dong, T. Wada, B. Bharate, Q. Yuan, S. Mukai, Y. Takeichi, S. Takakusagi, K. Asakura, J Synchrotron Rad 27 (2020) 1618–1625.

[19] X-Ray Absorption Fine Structure for Catalysts and Surfaces, Series on Synchrotron Radiation Techniques and Applications.

[20] J.J. Rehr, R.C. Albers, Rev. Mod. Phys. 72 (2000) 621–654.

CHAPTER 5 Application of *in-situ* EC-PTRF-XAFS for the Structure and the Formation Mechanism Studies of Spontaneously Deposited Pt Chloride Species on the Au(111)

The decoration of a foreigner metal M into Pt NPs lead to a significant increase in ORR catalytic activity and stabilities. Among these PtM NPs, the PtM with a core@shell (M@Pt) structure or Pt skin nanoparticles draw much interest because it realizes the 100% utilization of Pt and enhance the specific activity as well as stability in acidic media compared to Pt metal alone. The specific activity can be explained by two bimetallic effects, ligand effect and strain effect. To further study the origin of Pt-M bimetallic effects experimentally, it is desired to use single crystals with well-defined surfaces. However, it is difficult to obtain a two-dimensional (2D) Pt surface monolayer owing to its large surface tension. The SLRR reaction is one of the most facile methods to fabricate Pt surface monolayer via firstly form a sacrificial metal monolayer (e.g., Pb or Cu) on the substrate metal (e.g., Au(111), Ag(111)) by an UPD method. Then, the galvanic replacement reaction between the pre-deposited sacrificial metal layer and Pt^{n+} contained electrolyte occurs to obtain Pt ML. Yuan et al.[1] reported SLRR process of Pt sub ML on Au(111) by means of PTRF-XAFS with other surface science characterizations. It was found that 0.34 ML Pt was deposited on Au (111) surface, where 60 % was Pt (II) chloride complex and only 40 % was metallic Pt species. It was postulated that the 60 % Pt (II) chloride complex was produced via SD of H_2PtCl_6 on bare Au (111) surface.

The SD processes have been reported though the as-formed Pt monolayer adsorbed species and their coverage after SD of H_2PtCl_6 have not reached a consensus, as different structures have been proposed such as $PtCl_6^{2-}$, $PtCl_4^{2-}$, or $Pt(OH)_2$. Uosaki et al. [2]reported well-ordered structure of PtCl62- $\sqrt{7} \times \sqrt{7}\ R19.1°$ during the electrochemical deposition process. Strbac et al. [3] claimed

the formation of $Pt(OH)_2$ by XPS observation, which they conjectured as a result of hydrolysis of pre-formed $PtCl_4^{2-}$. Gokcen et al.[4] determined the coverage of the 2D Pt layer from the SD process as 0.25 ML for their ex-situ STM measurement. Waibel et al.[5] proposed $[PtCl_4]^{2-}$ with their STM observation. Although Pt complex on Au(111) after the SD process is a well-known process, several questions are await to be answered:

As Yuan et al.[1] report, the Pt species prepared via Cu UPD and Pt SLRR method gave a constant amount of Pt(II) chloride complex. What is the as-prepared chemical structure of Pt species on Au(111) in the SD process from H_2PtCl_6 without Cu UPD sacrificial monolayer? If Pt(II) species are formed from the $PtCl_6^{2-}$ not via the redox replacement reaction of Cu, what kind of redox reaction takes place during this SD process and what is the source of electrons for the reduction of $PtCl_6^{2-}$?

Answering these fundamental questions will provide a deeper insight into the SLRR reaction mechanism studies. In this chapter, the *in-situ* PTRF-XAFS technique was applied to study SD process of Pt deposition on Au (111) process without galvanic replacement reaction interference. Related redox mechanisms were discussed based on the XAFS result.

5.1 Sample preparations, surface characterizations, and *in-situ* EC-PTRF-XAFS measurement

5.1.1 Sample Preparations

The Pt decorated Au (111) sample was prepared for the BCLA feasibility investigation. Perchloric acid (60%), H_2SO_4 (98%), NaCl (99.98%) and $H_2PtCl_6 \cdot 6H_2O$ was purchased from Wako Pure Chemicals. Ultrapure water (UPW, 18.2 MΩ, Milli-Q, Merck Millipore Co) was used for the preparation of aqueous solutions as well as for rinsing. In all electrochemical characterizations, RHE was used as the RE and Pt foil was used as the CE. The Au (111) single crystals used in this work were disks with a diameter of 10 mm or 15 mm and a thickness of 5 mm (SPL, The

Netherlands). The Au (111) substrate with a high-quality is necessarily prepared before experiment, as introduced in Chapter 2, where several treating processes were carried out. The surface quality of treated sample is investigated by CV and atomic force microscope (AFM, Cypher, Oxford Instrument). Figure 5-1 shows the first cycle of CV scan, where the typical Au (111) reconstruction peak appears in the anodic scan at 0.65 VRHE, SO_4^{2-} adsorption peak and its phase transition spike appeared at 0.6 V_{RHE}, 0.8 V_{RHE} and 1.1 V_{RHE}. Figure 5-2(a) shows the surface morphology of a well-treated Au (111) sample with several monoatomic height steps as indicated in Figure 5-2(b). These characterization results confirmed that a Au (111) with a high quality is obtained.

The model catalyst system preparation via SD process was basically the same as Chapter 4 described. The pretreated Au (111) disks were first flame annealed using the butane gas for both sides to uniformly heat the sample and then transferred into N_2 filled glovebox. All solutions were purged with Ar for 1 hour before they were transferred into the glovebox. The SD Pt on Au (111) was prepared by contacting the Au(111) surface with the 0.1 M $HClO_4$ + 1 mM H_2PtCl_6 solution to form a meniscus for 30 s at open circuit potential (OCP). Then, the Au (111) surface was quickly dipped into UPW and washed for 30 s to obtained the Pt decorated Au (111), the obtained sample was termed as SD-Pt/Au(111).

5.1.2 Surface Characterization

XPS (JPC-9010MC, JEOL, Japan) was measured with monochromatized Al $K\alpha$ with 10 kV and 30 mA at 5×10^{-7} Pa. an as-prepared SD-Pt/Au (111) just after SD as well as a reduced SD-Pt_{subML}/Au(111) sample were transferred into a load lock chamber where the samples were first evacuated and then transferred to a measurement chamber. The time exposed to air was less than 2 min. The binding energy calibration was carried out by aligning the Au 4f7/2 peak at 84.1 eV. The peak fitting analysis was carried out on the Shirley background by the Lorentzian-Gaussian

peak function with 4f doublet splitting and area ratio fixed. The quantity of surface Cl was calibrated by $PtCl_2$ powder directly. Since Pt 4f overlapped with Au 5p1/2 broad peak around 74 eV, a clean Au (111) sample was measured to provide background reference, and the Au 5p1/2 peak was fitted with a Pseudo-Voigt function. Then, the same full width at half max (FWHM) and the area ratio to that of Au 4f was used to subtract the effect of 5p1/2 from the spectrum of the SD-Pt_{subML}/Au(111) samples. The peak areas thus obtained were used to calculate the Pt amount on the surface. Figures 5-3 show the Pt 4f and Cl 2p XPS spectra for an as-prepared SD-Pt_{subML}/Au(111) sample and those of a Pt/Au(111) sample after CV scans and electrochemical reduction. The Pt 4f7/2 binding energy (BE) of the as-prepared sample lies at 72.4 eV, which is well corresponding to Pt(II) in PtO (72.2 eV), $Pt(OH)_2$ (72.6 eV)[6] or K_2PtCl_4 (72.9 eV). After the reduction of SD-Pt/Au(111), Pt 4f7/2 BE decreased to 71.0 eV[6], close to the reported value for Pt(0). Cl species was also observed on the surface of the as-prepared SD-Pt/Au(111), with the Cl 2p3/2 and Cl 2p1/2 peaks at 197.9 eV and 199.6 eV, respectively. After the CV scan and linear sweep, all Cl was removed as shown in Figure 5-3(b). The surface Pt coverage was calculated to be 0.22±0.01 ML (as prepared SD-Pt_{subML}/Au(111)) and 0.18 ± 0.01ML (reduced SD-Pt_{subML}/Au(111)) based on the method presented in Figure 5-4. In the Yuan's paper[1], nearly 0.33 ML Pt was deposited after the SLRR where 2/3 was in the SD Pt species and 1/3 was the metallic Pt as a result of Galvanic replacement reaction. Thus, the 0.22 ML was the Pt species deposited on the Au by the SD process, well corresponding to the present work.

$PtCl_2$ was used as the reference sample to calibrate the sensitivity factors used for Cl/Pt ratio calculation, as shown in Figure 5-3(c). The Cl/Pt ratio on the as-prepared SD-Pt_{subML}/Au(111) sample was calculated to be 3.9±0.8 as shown in Table 5-1. This was different from the previous results, where Cl/Pt was about 2[7].

Figure 5-5 shows the CV scans of the as-prepared SD-Pt_{subML}/Au(111) sample in 0.1 M $HClO_4$. A reduction peak appeared at 0.5 V_{RHE} only in the first cycle. The subsequent cathodic peak below 0.3 V_{RHE} was characteristic of hydrogen underpotential deposition (H_{UPD}) and the anodic peak at 0.1 V_{RHE} corresponded to H desorption. Peaks located at 0.7 V_{RHE} and 0.9 V_{RHE} in the anodic and cathodic scans corresponding to OH and O adsorption and desorption, respectively[8]. After the first cycle, no reduction peak was observed around 0.5 V_{RHE}. Integration of the reduction peak and the H_{UPD} peak in the first cycle gave 70 μC cm^{-2} and 35 μC cm^{-2}, as shown in Figure 5-6 respectively. For the reduced SD-Pt_{subML}/Au(111) sample, the H_{UPD} area of 35 μC cm^{-2} is equivalent to 0.17 ML of Pt, which was quite close to the coverage of (0.18±0.01) ML given by XPS. This means nearly all Pt atoms were exposed to the surface. The 70 μC was due to the reduction of the SD Pt, suggesting the Pt species was 2+ as a valence state that needs two electrons to reduce to the metallic state as follows:

$$\text{SD } Pt^{2+} + 2e^- \rightarrow Pt$$

$$Pt + H^+ + e^- \rightarrow Pt - H \qquad (5\text{-}1)$$

5.2 Local structure determination for SD-Pt_{subML}/Au(111) model catalyst

The XAFS measurement carried out in this chapter, including apparatus and related properties were described in Chapter 2 and Chapter 4. Several detailed points are summarized as follows:

1. The X-ray incident window was changed from 6 μm Mylar film into 2.5 μm Mylar film because of weak *in-situ* fluorescence signal when applying 6 μm Mylar film.
2. Given the fact that the application of BCLA cannot give a good S/N ratio in EXAFS measurement, BCLA was not further applied in this Chapter.

Figure 5-7 shows the polarization dependent Pt L_3 edge EXAFS oscillations of SD-Pt_{subML}/Au(111) with error bars for each data point. The oscillations in the two polarization directions had almost identical periodicity though the s-pol had almost twice as large amplitude as that of p-pol. According to the Equation (2-26), the model that the planar $PtCl_4^{2-}$ was laid parallel to the Au surface could explain the observed data where $\frac{\chi(k,0)}{\chi(k,90)} = 2$.

To confirm this point, the simulation for EXAFS oscillation in the two polarization directions was carried out based on the model of a planar $PtCl_4$ structure parallel to the surface assuming Pt-Cl bond length of 2.27 Å. Red curves in Figure 5-7 were the simulated results. The goodness of fitting, R^2 was defined by the following equation:

$$R^2 = \frac{N_{ind}}{N(N_{ind} - \nu)} \sum_{i}^{N} \frac{\left(\chi_{obs}(k_i, \Theta) - \chi_{cal}(k_i, \Theta)\right)^{'2}}{\epsilon^2},$$

(5-2)

where $N_{\square}$, ϵ^2, $\chi_{obs}(k_i, \Theta)$ and $\chi_{cal}(k_i, \Theta)$ were the number of data points, error for each data point, and observed and calculated EXAFS data, respectively. Θ was a polarization polar angle of electric vector against direction (s-pol or p-pol). N_{ind} was the number of the information defined by Nyquist theory$\left(= \frac{2\Delta\, k \cdot \Delta r}{\pi} + 2\right) = 6$ and ν is the number of optimized parameters=2 (Debye Waller factor, σ^2 and the shift of kinetic energy zero, ΔE_0). The fitting model is acceptable when $R^2 < 1$. The R^2 shown in Figure 5-7 were 0.9 and 0.39 for s-pol and p-pol respectively, indicating the $[PtCl_4]^{2-}$ structure parallel to the surface was valid. The *in situ* PTRF-EXAFS experiment confirmed the Pt species deposited on the Au(111) in the SD process was planar $PtCl_4^{2-}$ parallel to the Au(111) surface.

Figure 5-8 shows the polarization dependence X-ray Absorption Near Edge Structure (XANES) spectra. The L3 edge reveals the electron transfer from the 2p3/2 to 5d orbital and the first abrupt peak at about 11565 eV was called the white line (WL) peak, the latter indicated the amount of empty d states. The s-pol XANES showed a sharper and higher WL intensity than that of p-pol. Note that the peak top energy of p-pol was shifted to higher energy compared to that of s-pol. The strong polarization dependence suggested the anisotropic structure and orientation of Pt species on the surface. Figure 5-8(a) also shows the XANES of K_2PtCl_4 salt which had the intermediate intensity between those of s-pol and p-pol. Figure 5-9 shows the XANES of Pt foil and H_2PtCl_6. The experimental s- and p-pol XANES spectrum appeared between those two. The WL height had the following order: Pt foil (0) ≈ Pt p-pol < Pt (II) < Pt s-pol < Pt (IV), indicating the Pt valence state of as-prepared SD-Pt_{subML}/Au(111) sample could be 2+. Figure 5-8(b) shows the simulated XANES using FEFF8 program based on the model of planar $PtCl_4$ parallel to the surface. The peak intensities were well reproduced in the FEFF simulation. The shift of the WL peak energy towards higher energy in p-pol was also well reproduced in FEFF simulation. XANES data indicated the $[PtCl_4]^{2-}$ planar structure lying parallel to the Au (111) surface. XANES could be explained by the molecular orbital picture. The empty orbital for the Pt (II) adopting $5d_8$ was d_{x2-y2} orienting to the chloride. The $2p_x$ and $2p_y$ orbitals could be excited to d_{x2-y2} in s-pol while the p_z orbital to d_{x2-y2} excitation was not allowed[7]. Thus, the s-pol XANES gave stronger WL than the p-pol.

5.3 Discussion on reduction source for $PtCl_6^{2-}$

For SD-process, what was the reducing agency? Pt suffered a reduction from Pt (IV) to Pt(II) during the SD process. Unlike the SLRR process, there was no reducing reagents such as the sacrifice Cu layer. What if the surface Au atoms reacted with the $[PtCl_6]^{2-}$ to reduce it to $[PtCl_4]^{2-}$?

According to this assumption, the following reactions could be assumed:

Oxidation:

$$\mathrm{Au} + 4\mathrm{Cl}^- \rightarrow \mathrm{AuCl_4}^- + 3\mathrm{e}^-$$

$$E_{ox}{}^0 = -1.002V \text{ (5-3)}$$

Reduction:

$$\mathrm{PtCl_6^{2-}} + 2e^- \rightarrow \mathrm{PtCl_4^{2-}} + 2\mathrm{Cl}^-$$

$$E_{red}{}^0 = 0.680\ V \text{ (5-4)}$$

Hence, the overall reaction should be:

$$2\mathrm{Au} + 2\mathrm{Cl}^- + 3\mathrm{PtCl_6^{2-}} \rightarrow 2\mathrm{AuCl_4^-} + 3\mathrm{PtCl_4^-}$$

$$E_{overall}{}^0 = -0.32V \text{ (5-5)}$$

$$\Delta G^0 = -6 \times 96500 \times 0.32 = 180\ kJ \cdot mol^{-1}$$

$$\frac{[AuCl_4^-]^2[PtCl_4^-]^3}{[PtCl_6]^3[Cl^-]^2} = 1.8 \times 10^5 > 0$$

(5-6)

The ΔG>0 indicated that the assumed pathway is not thermodynamically favored. Therefore, The Au might not be the candidate for the reducing reagent. Reducing reagents are still a mystery.

5.4 Conclusion

In this work, the SD deposited Pt species onto Au(111) surface from a precursor of acidic $PtCl_6^{2-}$ solution was studied. By a combination of XPS, CV, and *in-situ* PTRF-XAFS techniques, it has

been determined that the as-deposited species was isolated $PtCl_4$ and the polarization-dependent XAFS experiment proved the parallel orientation of the planar $[PtCl_4]^{2-}$ to the Au (111) surface. However, the reducing agent for SD process remains unclear. The surface coverage of the monolayer species was around 0.2 ML both by ECSA and CV, well corresponding to the values estimated in the SLRR process.

The developed *in-situ* EC-PTRF-XAFS challenged to reveal the 3D structure information for extremely limited Pt ($\sim$ 0.2 ML) amount by changing the polarization directions. The total reflection condition and application of thin solution layer eliminated the solution induced inelastic scatterings effects contribution to background signals. The special design of the EC-PTRF-XAFS apparatus ensures structure investigation under electrolyte appeared condition without air contamination and allows the application of potentials corresponding to the real operating conditions. In addition, the SD reaction process are successfully tracked in this chapter, which will provide a deep understanding of SLRR and a new way to prepare the ML or subML Pt species on the Au (111). In summary, the EC-PTRF-XAFS contributes to the ORR chemical reaction mechanism studies.

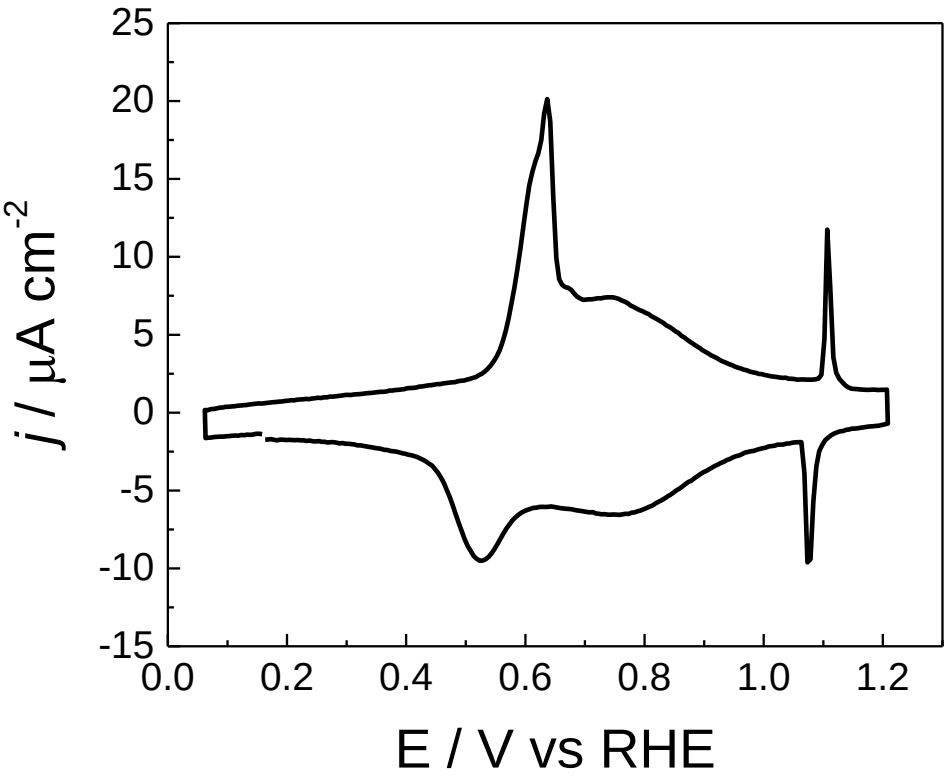

Figure 5-1. First cycle of cyclic voltammetry scan for well-treated Au (111) in 50 mM H2SO4, scan rate: 50 mV/s.

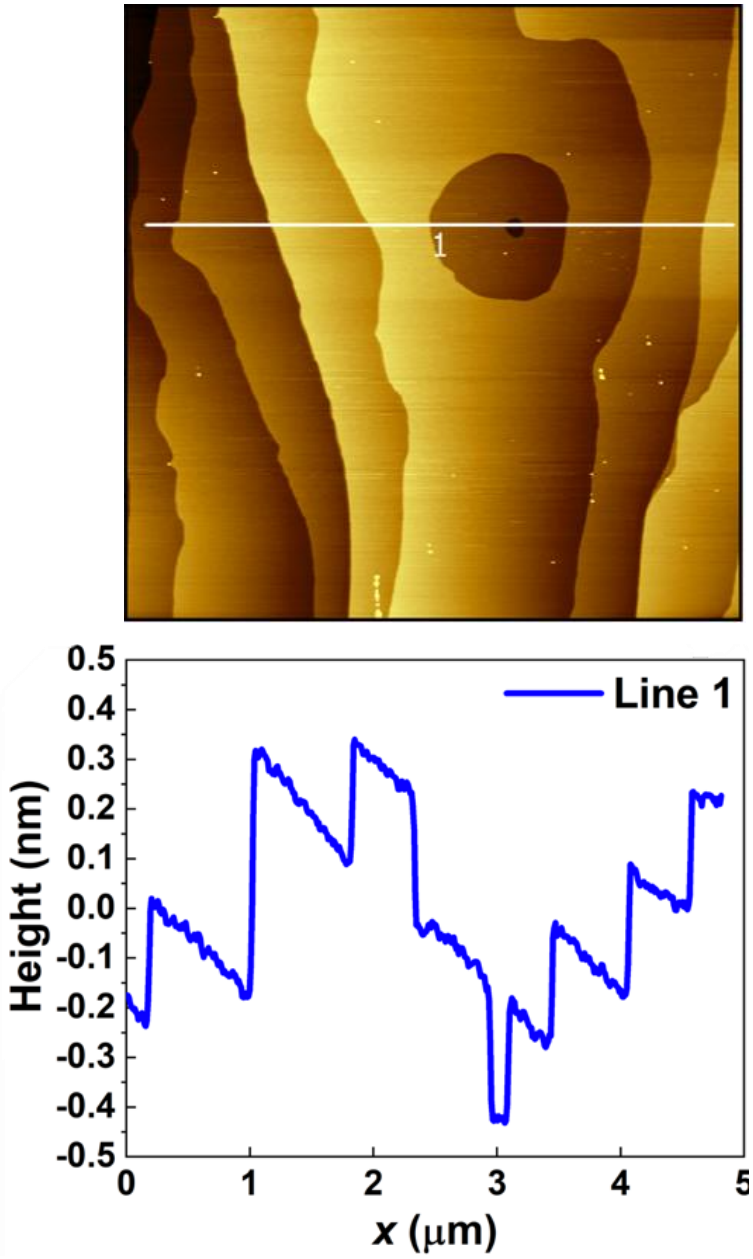

Figure 5-2. (a) AFM image of Au (111) with high quality. (b) monoatomic step height of Line 1 indicated in Figure 5-2(a).

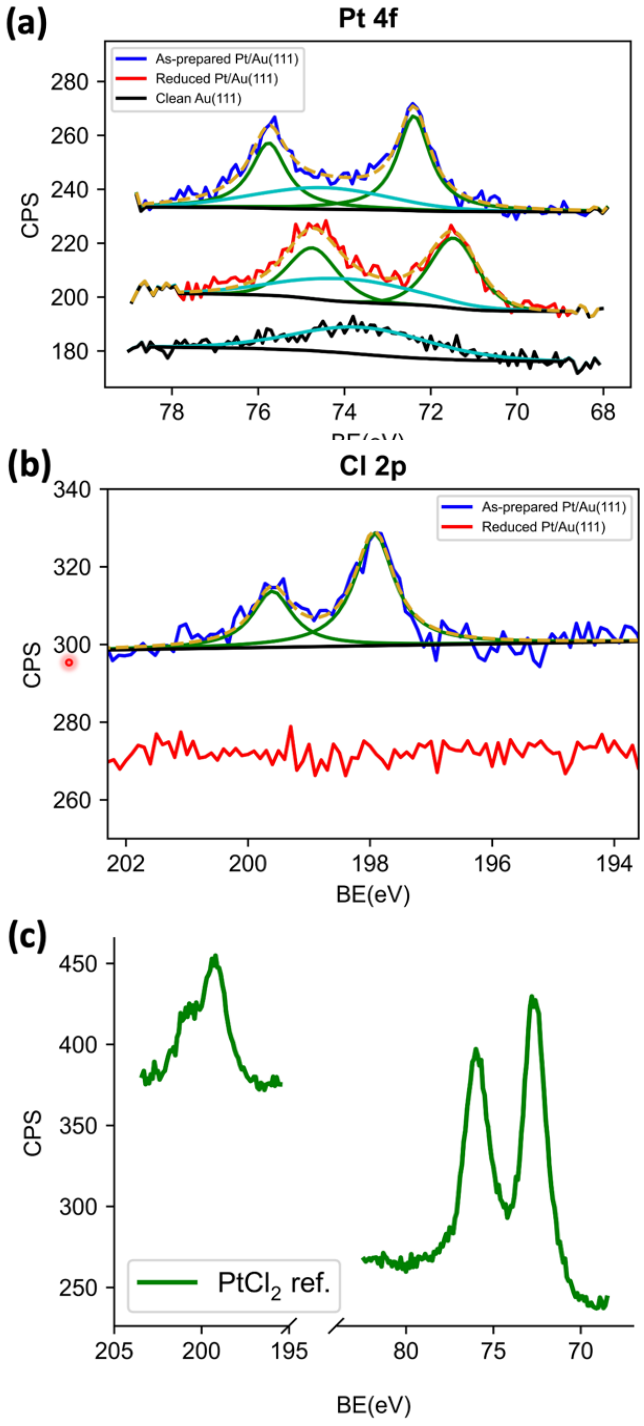

Figure 5-3. Pt 4f (a) and Cl 2p (b) XPS spectra for the as-prepared Pt/Au (111) sample (upper blue) and the reduced Pt/Au (111) sample (lower red).

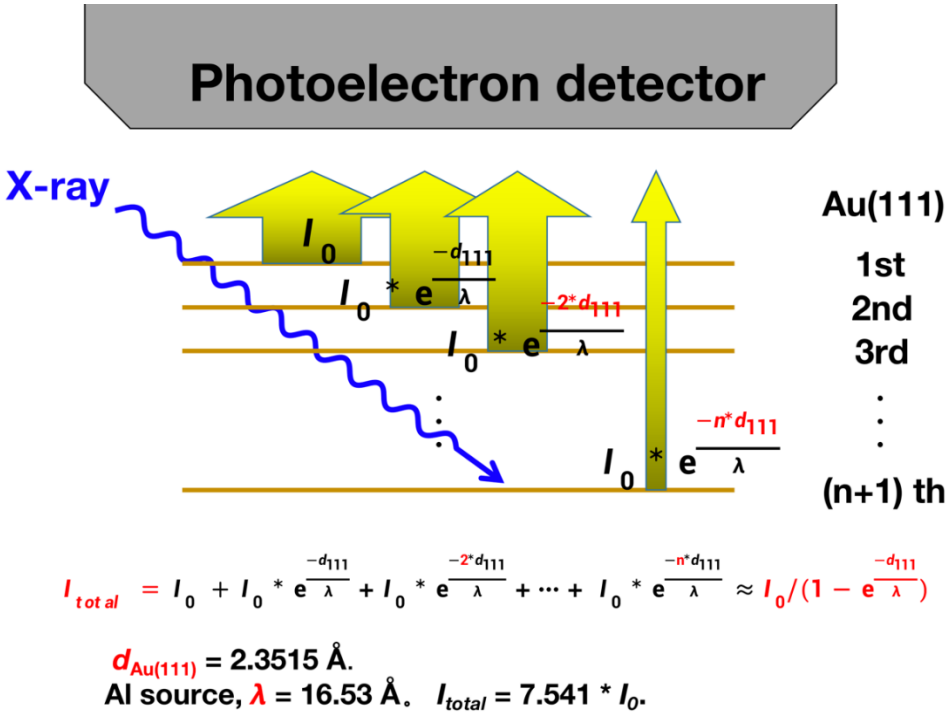

Figure 5-4. After being excited by the incident X-ray, the ejected Au 4f photoelectrons undergo attenuation within the subsurface region. Each Au (111) layer contributes less signal to the photoelectron detector as the depth increases. The total Au 4f signal of the Au (111) single crystal surface is calculated to be about 7.5 times that of a monolayer of Au (111) surface.

Table 5-1. Pt and Cl XPS intensities, and corresponding Pt/Cl ratio.

	Pt 4f area	Cl 2p area	Cl/Pt atomic ratio
$PtCl_2$	610±60	190±20	(2)
SD-Pt/Au(111)	88±7	54±7	3.9±0.8

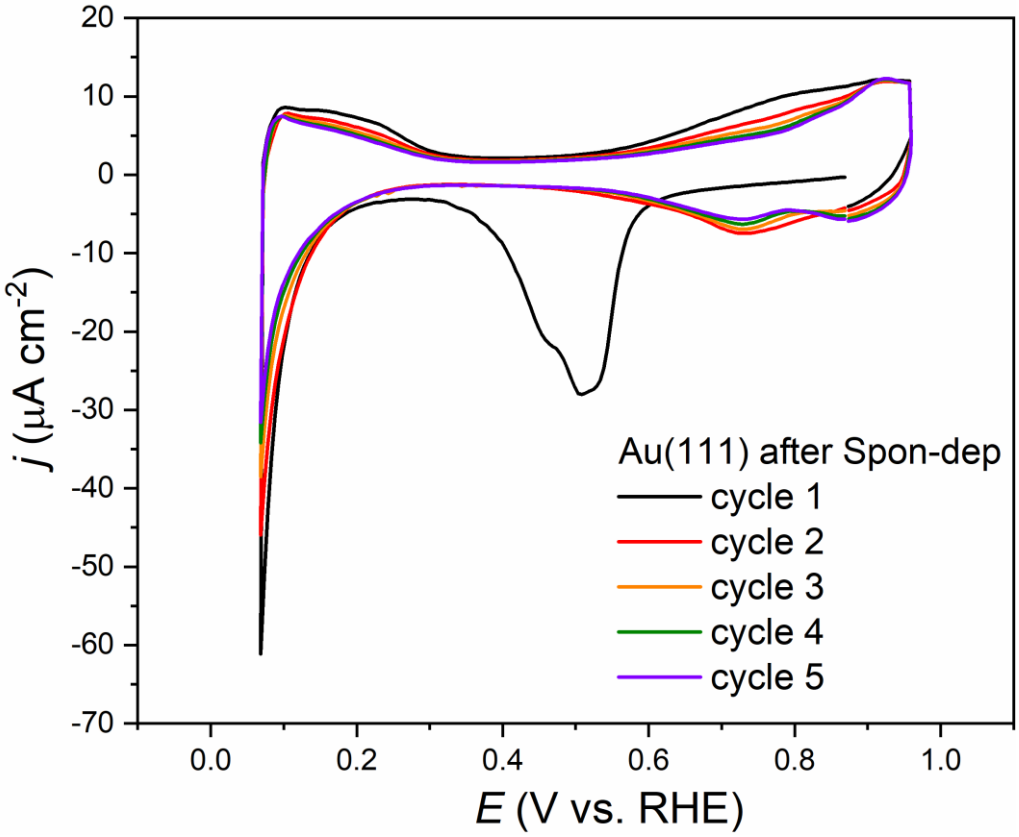

Figure 5-5. Five cycles of CV scan of the as-prepared SD-Pt_{subML}/Au (111) sample in 0.1 M $HClO_4$ between 0.07-0.96V. The starting potential is chosen to be the measured OCP of 0.87 V and then scanned in the cathodic direction at a rate of 50 mV s^{-1}.

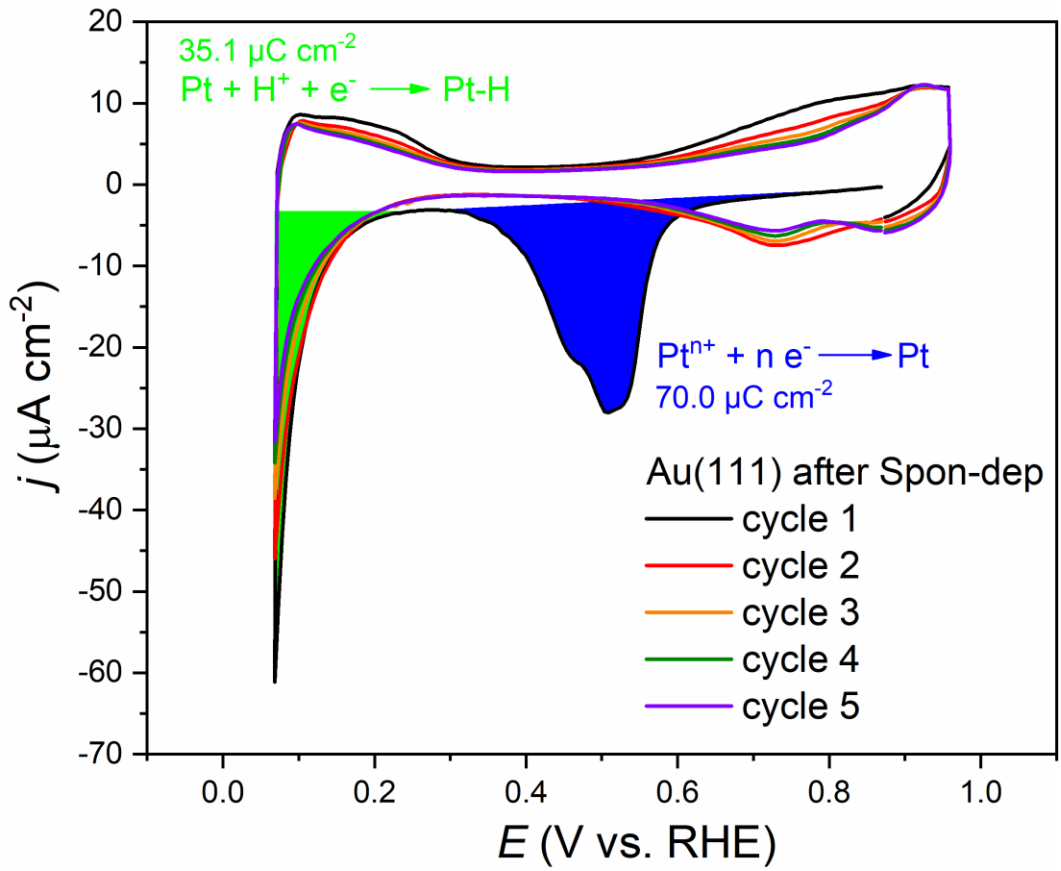

Figure 5-6. Integration of the reduction peak and the H_{UPD} peak in the first cycle CV of the as-prepared SD-Pt_{subML}/Au(111) in 0.1 M $HClO_4$.

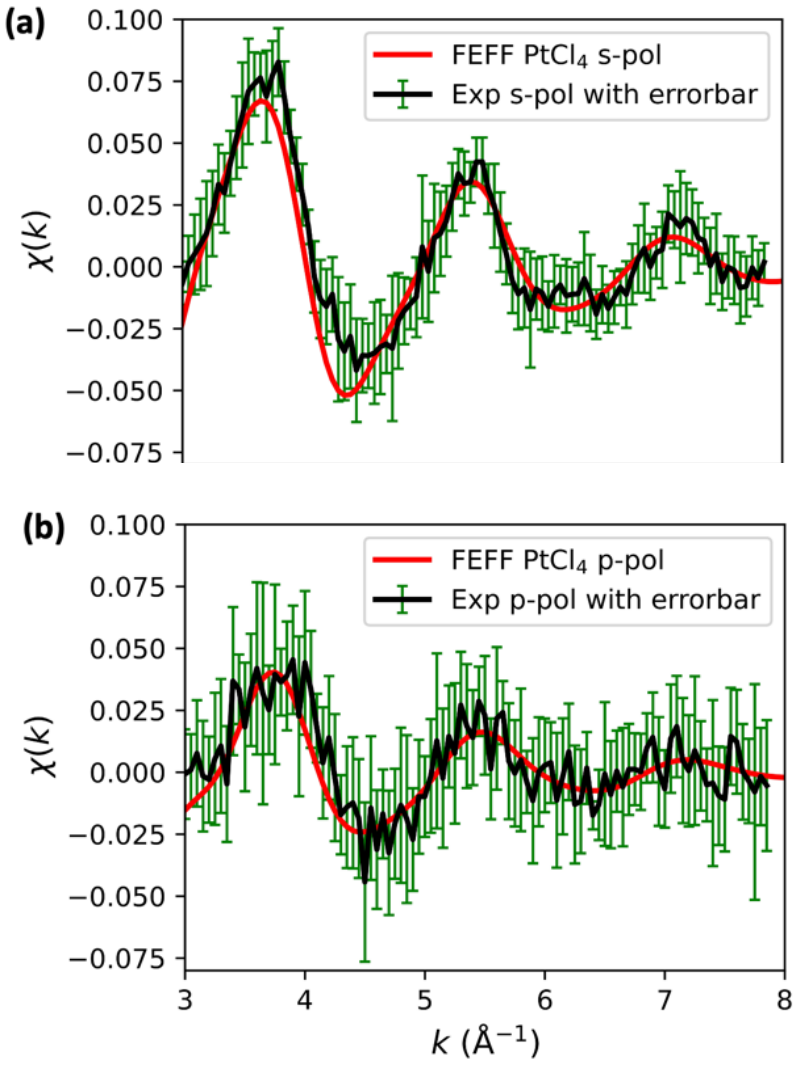

Figure 5-7. Pt L_3 edge EXAFS oscillation of the as-prepared SD-Pt_{subML}/Au (111) in s- (a) and p- (b) polarizations. The black curve with the green error bar in each graph showed the experimental data. The red curve is the simulated EXAFS oscillation for a $PtCl_4$ structure (Pt-Cl bond length: 2.27 Å) under different polarization conditions. $[PtCl_4]^{2-}$ has a planar structure with its molecular plane parallel to the surface.

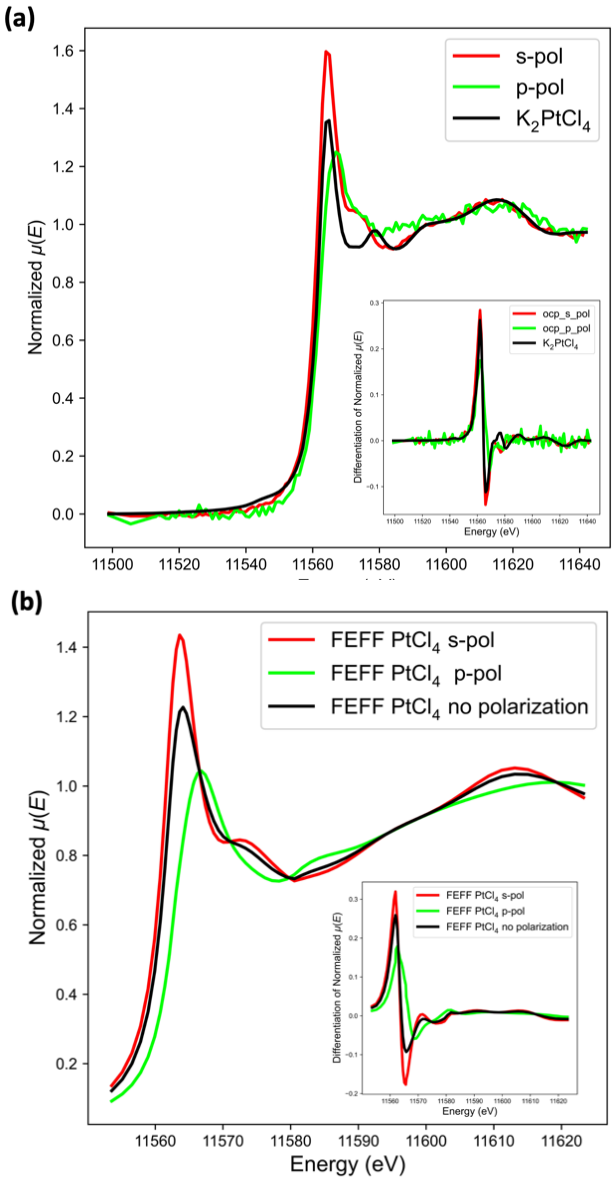

Figure 5-8. (a) Pt L_3 XANES spectra of the Pt_{subML}/Au(111) after the SD process under s- and p-polarizations, together with that of K_2PtCl_4. The inset in the bottom right shows the differentiated curve of the XANES, in which a very tiny shift of the edge (~0.5 eV) can be found. (b) FEFF simulated XANES spectra of a planar $PtCl_4$ structure (Pt-Cl bond length: 2.27 Å) under different polarization conditions. The inset in the bottom right shows the differentiated curve of the XANES. An obvious edge shift feature was presented.

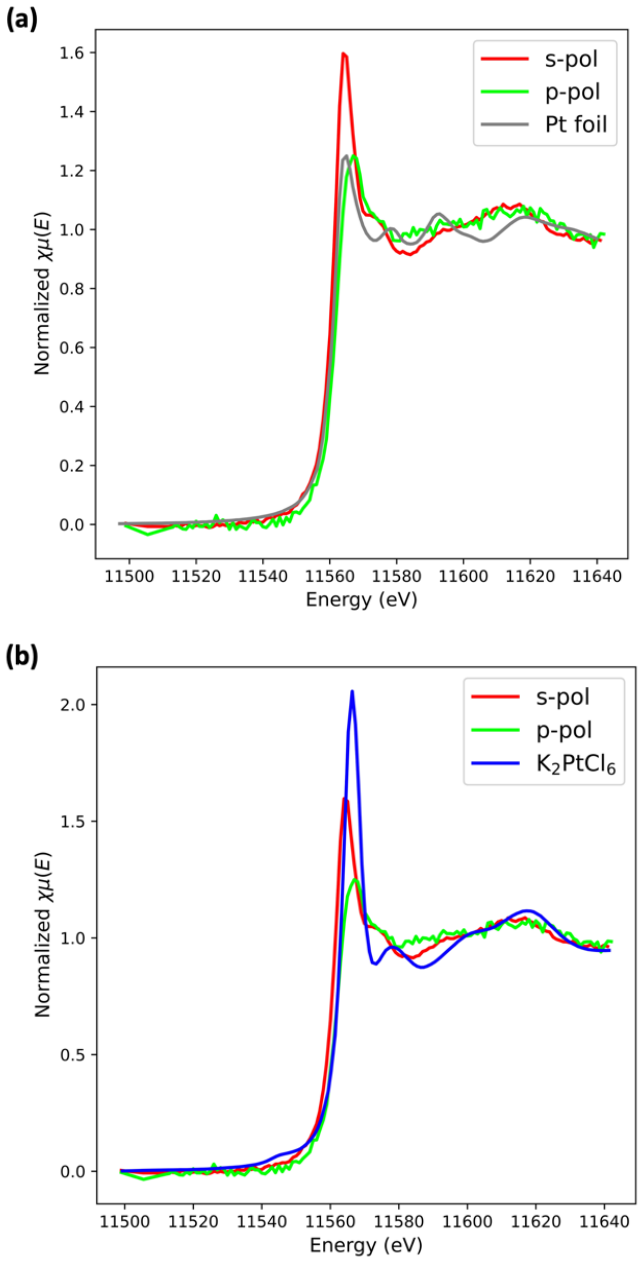

Figure 5-9. Comparison of the s-pol and p-pol Pt L_3 XANES of the Pt/Au (111) sample with those of (a) Pt foil and (b) K_2PtCl_6.

Reference

[1] Q. Yuan, Y. Wakisaka, Y. Uemura, T. Wada, H. Ariga-Miwa, S. Takakusagi, K. Asakura, S.R. Brankovic, J. Phys. Chem. C 122 (2018) 16664–16673.

[2] K. Uosaki, S. Ye, Y. Oda, T. Haba, K.I. Hamada, Langmuir 13 (1997) 594–596.

[3] S. Strbac, S. Petrovic, R. Vasilic, J. Kovac, A. Zalar, Z. Rakocevic, Electrochimica Acta 53 (2007) 998–1005.

[4] D. Gokcen, S.-E. Bae, S. Brankovic, Journal of The Electrochemical Society 157 (2010) D582.

[5] H.-F. Waibel, M. Kleinert, L.A. Kibler, D.M. Kolb, Electrochimica Acta 47 (2002) 1461–1467.

[6] J.S. Hammond, N. Winograd, Journal of Electroanalytical Chemistry and Interfacial Electrochemistry 78 (1977) 55–69.

[7] Q. Yuan, S. Takakusagi, Y. Wakisaka, Y. Uemura, T. Wada, H. Ariga, K. Asakura, Chemistry Letters 46 (2017) 1250–1253.

[8] A.J. Bard, L.R. Faulkner, H.S. White, John Wiley & Sons, 2022.

CHAPTER 6 Application of *in-situ* EC-PTRF-XAFS for the Structure Determination of Reduced Pt_{subML}/Au(111) model catalyst system prepared via Underpotential Deposition and Galvanic Replacement Reaction Methods

As mentioned in Chapter 5, M@Pt core-shell catalysts with a Pt monolayer skin is a promising alternative to the conventional carbon supported Pt NPs. To study the origin for the improved specific activity in M@Pt core-shell catalysts is essential for further improving the catalytic performance. When the Pt monolayer are decorated on Au substrate surface in core@shell catalysts systems, several properties are significantly changed due to the lattice mismatch between the Au and Pt, where the lattice parameter of Au is slightly larger than that of Pt by ~ 3.8 % in the bulk state, therefore, tensile strain exists if Pt grows epitaxially onto an Au substrate. It has been proved by DFT that the extension of Pt-Pt bond distance can lead to a change of d-band center, resulting in the obstruction of oxygen atoms or *OH hydrogenation slow kinetics. In this case, Pt monolayer modified Au single crystal surface should give lower activities than pure Pt catalysts. Zhang et al.[1] reported that the Pt ML on Au(111) showed lower activity than the clean Pt(111). However, Kaito et al.[2] reported an unexpected shortened Pt-Pt bond distance in Au@Pt core-shell system with an increased ORR electrocatalytic activity than the conventional used carbon supported Pt NPs, which is in agreement with Mukerjee et al. [3] reported. The latter proposed the Pt-Pt bond distance dependent ORR catalytic activity. To study what is the role of strain effect in Pt ML modified Au (111) substrate, how does the Pt-Pt bond distance variation contribute to the ORR catalytic activity, it is necessary to introduce the model catalyst system to obtain flat Pt ML on Au (111) single crystal surface without aggregations. SLRR reaction is a facile method to obtain noble metal monolayers for model catalyst systems preparations. Yuan et al.[4] reported that the UPD and SLRR method prepared homogeneously dispersed 0.3 ML Pt consisted of two kinds of species:

60 % are SD process induced [$PtCl_2$] complex, and 40 % are metallic Pt species. Chapter 5 investigated the SD process in detail and proposed a different Pt-Cl complex $[PtCl_4]^{2-}$ from Yuan's analysis, which was revealed by applying several kinds of surface characterizations, like XPS, AFM, as well as *in-situ* EC-PTRF-XAFS measurements. However, the discussion related to the reduced Pt_{subML}/Au (111) prepared via Cu UPD and Pt SLRR method are still lacking.

This chapter focus on investigating the Pt-Pt bond distance in reduced Pt_{subML}/Au (111) model catalyst system by applying *in-situ* EC-PTRF-XAFS apparatus. This unique technique allows the *in-situ* electrochemical study for a low concentration of Pt species within electrolyte. The polarization dependent feature was found at both XANES and EXAFS spectra, which claimed the strain effect and ligand effect between the Pt planar layer and Au (111) substrate.

6.1 Pt_{subML}/Au (111) sample preparation, Surface Characterization, and *in-situ* EC-PTRF-XAFS apparatus

6.1.1 Model Catalyst Preparation and in-situ EC-PTRF-XAFS measurement

Hexachloroplatinate (IV) Hexahydrate ($H_2PtCl_6 \cdot 6H_2O$, 99.9%) and perchloric acid (60%) were purchased from Wako Pure Chemicals Co., Ltd. 18.2 MΩ cm ultrapure water (UPW) was used for solution preparations. All the solutions were deaerated with N_2 outside for 1 hour before experiments. All potential mentioned in this paper were reported with respect to RHE, unless specially denoted. The freshly prepared Au (111) substrate as well as all the solutions and cells were transferred into the glovebox for sample preparations. An HSV-110 potentiostat (Hokuto Denko) was used for all electrochemical experiments. For sample preparation, the Cu UPD was carried out in 0.1 M $HClO_4$ + 1 mM Cu $(ClO_4)_2$ solution. A three-electrode glassy electrochemical cell with Pt foil as CE and Cu wire as RE were used for Cu UPD. The UPD potential range followed previous reported values, + 0.03 V to + 0.40 V vs Cu/Cu^{2+} pseudoeletrode. The deposition potential

was chosen as 0.03 V, holding at this value for 30 s. After this, the sample was washed by the UPW for 30 s. Then, the replacement reaction between Pt^{4+} and metallic Cu species occurred in 0.1 M $HClO_4$ + 1 mM H_2PtCl_6. Finally, the as-prepared sample was set on the *in-situ* EC-XAFS cell for further reduction in 0.1 M $HClO_4$ and XAFS measurement. The *in-situ* EC-XAFS cell configuration was the same as introduced in Chapter 4 and Chapter 5.

The *in-situ* EC-XAFS measurement was carried out in the abovementioned cell during XAFS measurement in 0.1 M $HClO_4$. The solution was continuously purged by N_2 and circulated throughout the XAFS measurement by a biomorph pump (BPF-456p, a Nitto Kohki). The *in-situ* EC-XAFS was measured at BL12C in KEK-IMSS-PF. The monochromator was a Si (111) double crystal. The fluorescence signal was collected by seven-element SDD (Techno-AP, Tsukuba, Japan), which was equipped with *Soller* slits and Zn filters. The *in-situ* EC-XAFS cell and pump system was set on a five-axis goniometer to adjust the polarization directions and total reflection conditions. Before XAFS started, the sample was lowered down to have a solution layer thicker than 1 cm, to ensure the mass or electron transportations for reduction reactions. The reduction potential was chosen at 0.3 V_{RHE}, which is before the H adsorption onset, and negative to the surface oxidations. The XAFS measurement started after applying potential for 30 mins to have [$PtCl_4$] species fully reduced into metallic Pt species. Then, the sample was pushed up, a thin solution layer was preserved around tens of micron meters, to reduce the solution scattering effect as much as possible. The electrodes was covered with Pb sheets to reduce the eliminate possible contaminations.

6.1.2 Surface Characterization

The surface quality of Au (111) was preliminary checked in 50 mM H_2SO_4 with scan rate of 50 mV/s, before deposition experiments. Characteristic peaks are clearly observed in Figure 6-1,

which revealed the perfect surface state of Au(111). Pt foil was used as CE. The Pt loading and chemical state was determined for the reduced Pt_{subML}/Au (111) sample by JEOL JPC-9010MC X-ray photoelectron spectroscopy (XPS). Due to the great peak shielding effect on Pt 4f peak regions arising from satellite peaks of Au 4f peaks between 70 eV to 80 eV, the XPS was carried out under monochromator mode equipped with Al Kα (1486.7 eV) X-ray source at 12 kV and 25 mA under 10^{-6} Pa. The binding energy (BE) was calibrated using Au 4f 7/2 peak set at 84.0 eV. XPS analysis was carried out after background removal by the Shirley method and peak fitting using Lorentzian-Gaussian curves, fixing the doublet peak separations and peak area ratios. Figure 6-2 shows the narrow scans in Au 4f, Pt 4f and Cl 2p regions for reduced Pt_{subML}/Au (111) sample. Peak fitting details are summarized in Table 6-1. For Pt 4f regions, both metallic and oxidized Pt species were found while the main species were still consisted of metallic Pt, the existence of oxidized Pt species probably caused by sample exposure to the air after XAFS measurement and before XPS measurement. As shown in Table 6-1, a flat Pt monolayer on Au (111) substrate model was assumed, which gave a total Pt amount of 4.2×10^{14} Pt atoms cm^{-2}. The basic principle for calculation of Pt amount follows the description introduced in Chapter 3 and Chapter 5, the relationship between the atom numbers and peak intensity in XPS is described as Equation (3-1) and methodology as shown in Figure 5-5.

Therefore, the calculated Pt amount was 0.3 ML, which is consistent with Yuan et al.[4] reported ones. No chloride species was found, which further indicated the successful reduction of Pt_{subML}/Au (111) sample. The surface morphology for the reduced sample was characterized by AFM (Cypher, Oxford Instruments), as shown in Figure 6-3. Steps in atomic height are clearly observed as well as uniformly dispersed Pt particles, where no aggregation was found even after long-term XAFS measurement as indicated in Figure 6-3(b). Histogram for particle height was

summarized in Figure 6-3(c), which gave an average particle height of (2.6 ± 0.7) Å. Given the XPS and AFM results, it can be concluded that a subML metallic Pt species on Au (111) with an atomic height was obtained.

6.2 *In-situ* structure determination for reduced Pt_{subML}/Au(111) model catalyst

Figure 6-4 shows the normalized XANES spectra at Pt L_3 edge for reduced Pt_{subML}/Au (111) sample measured at 0.3 V under different polarization directions with comparison to reference spectra. A clear WL feature was observed at the absorption peak, which corresponds to the dipole transition process from 2p 3/2 to 5d state, revealing the unoccupied d orbitals. For s-polarization, the WL intensity showed a higher value than Pt foil, similar to that of K_2PtCl_4, while the shape was more similar Pt foil especially from 11590 eV to 11620 eV. For p-polarization, the WL intensity was decreased when compared to the s-polarization, while the intensity was still higher than that of the Pt foil but lower than K_2PtCl_4. The peak shape was more like that of Pt foil. The metallic Pt state can be assumed from the XANES results. In addition, peak broaden feature was observed at both polarization directions when compared to the Pt foil where s-polarization data showed a more obvious feature than that of p polarization. Considering the bonding species in different directions, the peak broaden feature at p-polarization can be attributed to the Pt-Au interaction. Higher WL intensity at s-polarization can be ascribed to the polarization dependent feature induced by charge transfer between Pt_{subML} and Au (111) substrate.

Figure 6-5 shows the k^0 weighted $\chi(k)$ oscillation of reduced Pt_{subML}/Au (111) sample comparison to foil data. Due to the measurement limitations, data collection at p-polarization was only up to 8 $Å^{-1}$. Both polarization experimental data reproduced the major features of two foils, and it was hard to distinguish that experimental data was more like which reference data at low k region. However, the wavelength of $\chi(k)$ oscillation at s-polarization near high k region was more

comparable to that of the Au foil, which is the most direct evidence for Pt-Pt bonding extraction. In addition, $\chi(k)$ oscillation at different directions showed amplitude differences especially at k = 3.5 Å^{-1}, which proved the polarization-dependent feature of the reduced Pt_{subML}/Au (111) sample, probably caused by different kinds of bonding. Furthermore, similar $\chi(k)$ oscillation frequency at different polarization direction proved that the Pt-Pt and Pt-Au may possess similar bond distance values. Considering the complexity of analysis system, the $\chi(k)$ oscillation at s-polarization direction revealing Pt-Pt bonding may include extra contribution from Pt-Au bonding, therefore, the curve fitting result cannot give the most exact analysis result. Given the current analysis result of 2D surface morphology and bond distance extraction for Pt-Pt bonding, the polarization dependent feature and enlarged bond distance should be considered for further detailed structure analysis.

A simulation model with Pt_n deposited two dimensionally on Au (111) was proposed. The cluster size are altered from Pt_7, where the center Pt atom is surrounded by 6 Pt atoms as the first surrounding layer. Then, the size was increased to Pt_{19}, with 12 Pt atoms as the second surrounding layer, and so on. The theoretical simulation was carried out by Feff8. The polarization dependent feature at Pt L_3 edge was assumed as Equation (2-26). The Feff simulation result was evaluated by the R-factor, defined as:

$$R - factor = \frac{\sum\{\chi_{exp}(k) - \chi_{cal}(k)\}^2}{\sum\{\chi_{exp}(k)\}^2} \tag{6-2}$$

Figure 6-7 shows the simulation result based on the Pt_{19} planar layer supported by Au (111) substrate. The Pt-Pt bond distance is set at 2.88 Å, the distance between the Pt planar layer and

topmost Au layer is the same as the Au interlayer distance in Au (111) bulk, 2.40 Å. For Pt_{19} simulation at s-polarization, the wavelength reproduced that of experimental data and Au foil, proved that the Pt-Pt bond distance extraction in the Pt_{subML}/Au (111) model catalyst system.

The Au bulk-like Pt-Au interlayer distance assumed in the EXAFS simulation, and AFM proved slightly higher interlayer distance all indicated that there's a repulsive interaction between the Pt_{subML} and underlying Au substrate. This repulsive force can be attributed to the d-band center change due to the ligand effect between the Pt_{subML} and the Au substrate, which can be further proved by related DFT calculations.

6.3 Conclusion

The developed *in-situ* EC-PTRF-XAFS method was successfully applied for the metallic Pt_{subML}/Au(111) model catalyst with a limited amount structure investigation. Metallic Pt valence state was proved by the XPS and XANES analysis, AFM indicated the monoatomic height of the Pt_{subML} without surface aggregation. The Pt-Pt bond distance for reduced Pt_{subML}/Au(111) model catalyst were confirmed to be extracted by EXAFS simulation, which even reached that of the Au-Au bond distance, 2.88 Å. The interlayer distance between the Pt_{subML} and the underlying Au substrate was also confirmed, where a repulsive force existed. The successful application of this developed XAFS method with unique design provided a new insight for distinguishing the role of individual metals at atomic scales in bimetallic ORR catalysts studies.

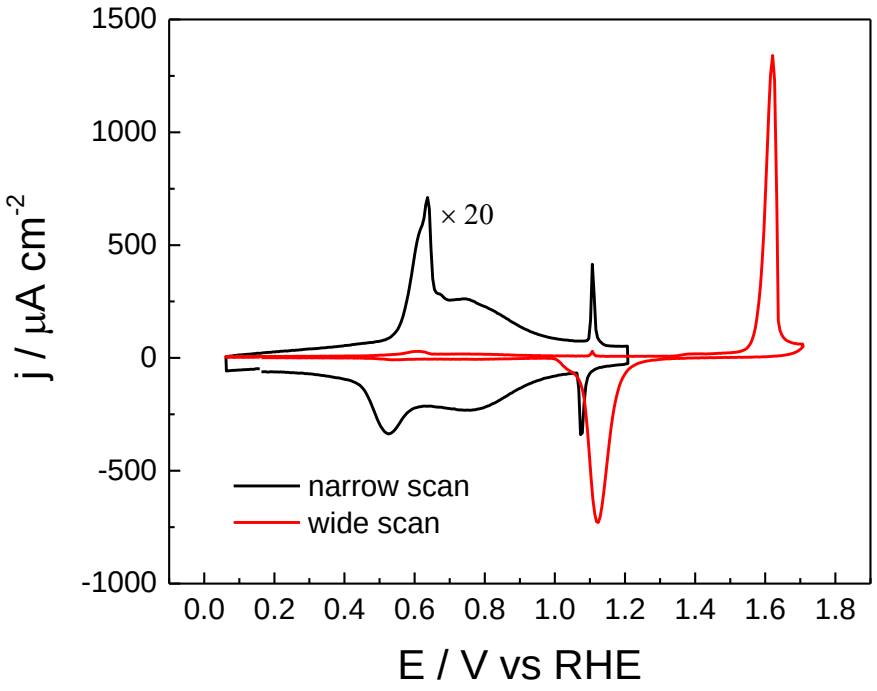

Figure 6-1. Cyclic voltammetry for Au (111) in 50 mM H_2SO_4, scan rate: 50 mV/s.

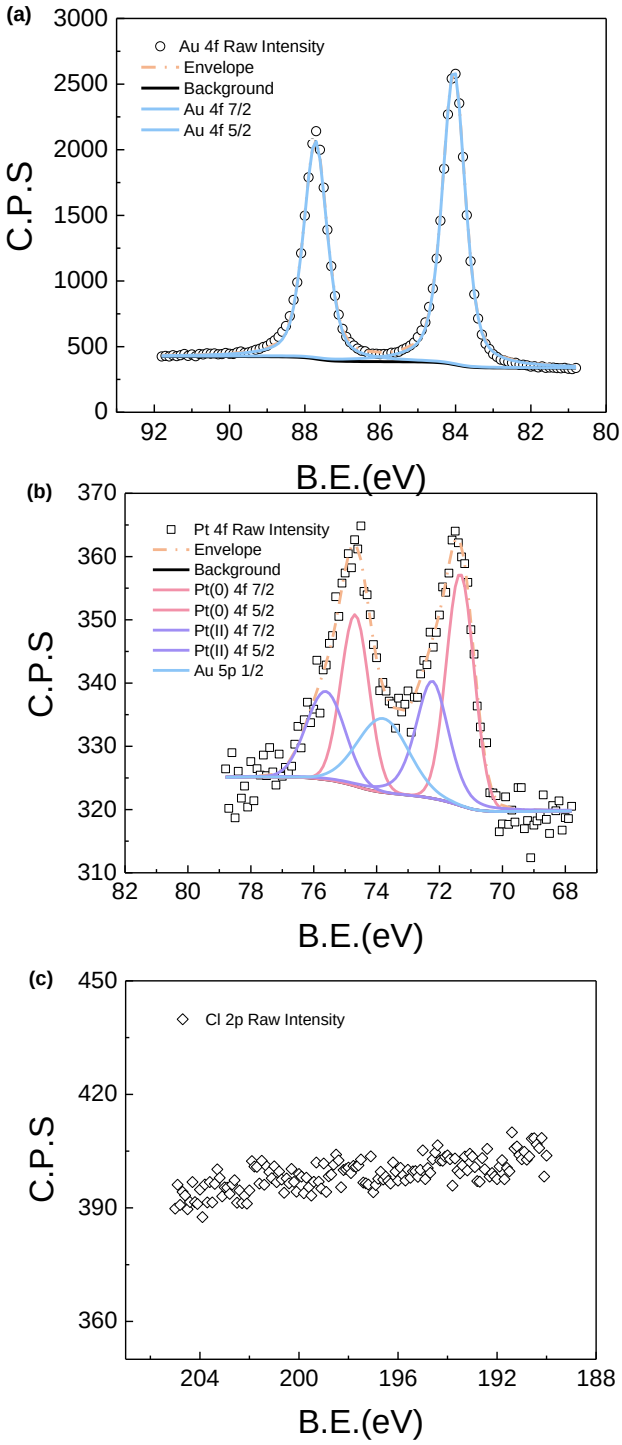

Figure 6-2. XPS peaks for (a) Au 4f, (b) Pt 4f and (c) Cl 2p regions, respectively.

Table 6-1. XPS peak positions determination

Species	Peak position / eV
Au 4f 7/2	84.0
Au 4f 5/2	87.7
Pt(0) 4f 7/2	71.4
Pt(0) 4f 5/2	74.7
Pt(Ⅱ) 4f 7/2	72.2
Pt(Ⅱ) 4f 5/2	75.6
Au 5p 1/2	73.9

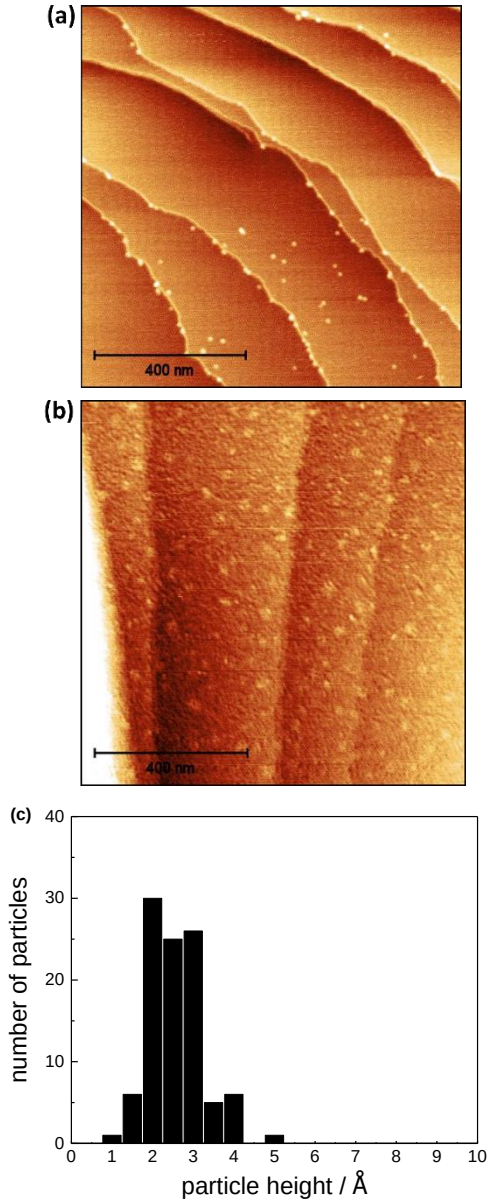

Figure 6-3. AFM for (a) bare Au(111) surface and (b) Pt_{subML}/Au(111) sample surface after sample reduction and (c) particle height histogram for Figure 6-2(b).

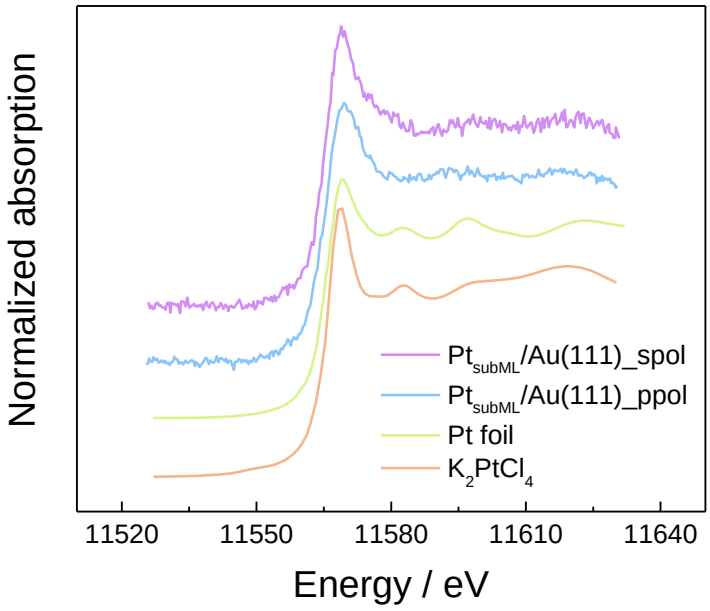

Figure 6-4. XANES spectra for reduced samples at different polarization directions.

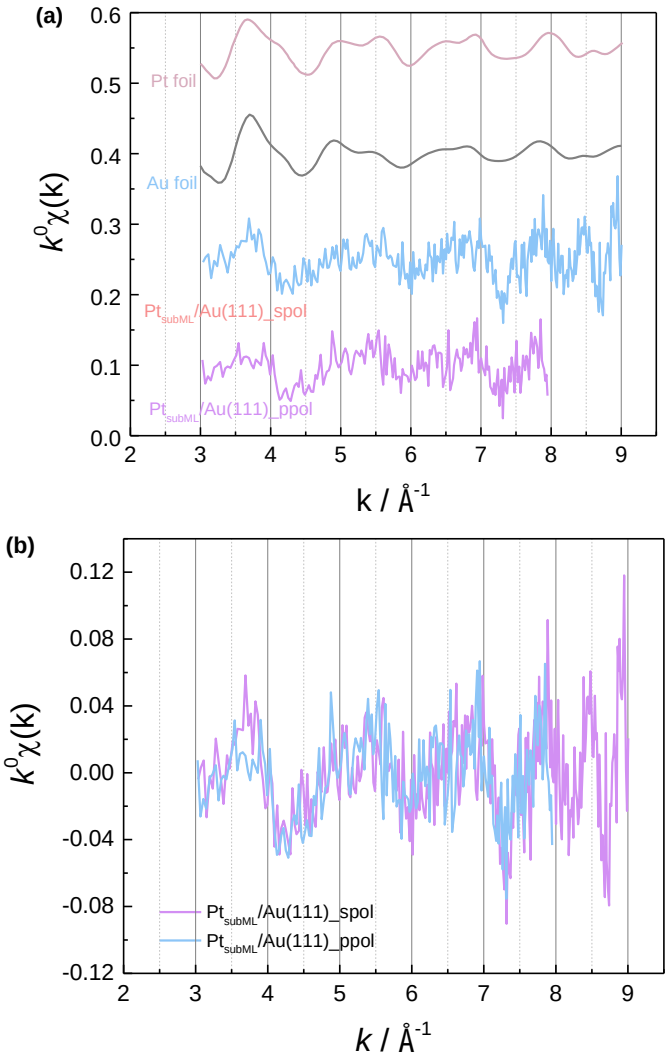

Figure 6-5. (a) k^0-weighted EXAFS oscillation for reduced Pt_{subML}/Au (111) sample in comparison with oscillation for the Pt foil. (b) k^0-weighted EXAFS oscillation amplitude comparison at different polarization directions.

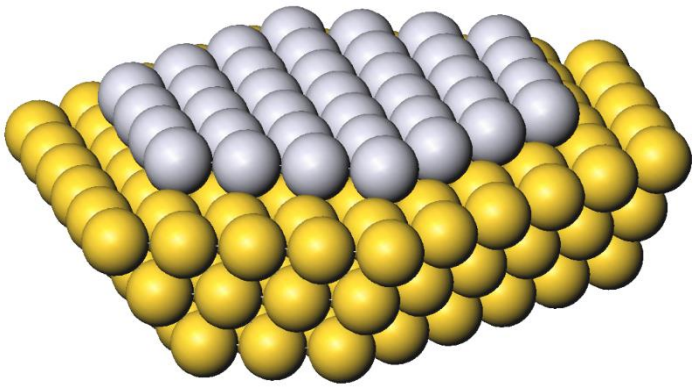

Figure 6-6. Simulation model of Au(111) supported planar Pt monolayer, Pt_{19}/Au(111), where the Pt-Pt planar bond distance and distance between the planar Pt monolayer and topmost Au layer were changed in practical simulation. Particle size was also altered while the center Pt atom position remains the same.

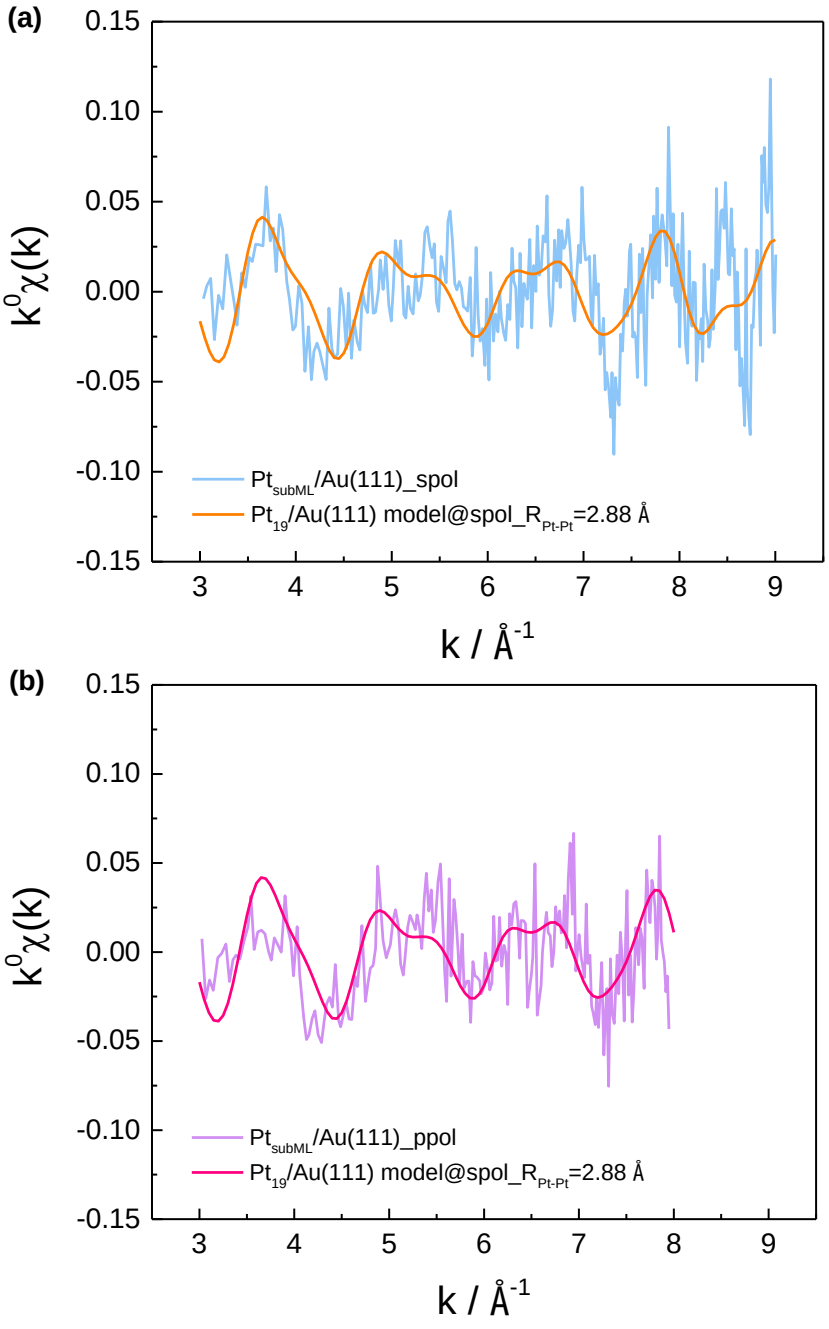

Figure 6-7. The best simulation result using Pt_{19}/Au (111) model with a Pt-Pt bond distance set at 2.88 Å and distance between the Pt planar layer distance to Au substrate topmost layer as Au interlayer distance in Au (111) bulk. (a) s-polarization; (b)p-polarization.

Reference

[1] J. Zhang, M.B. Vukmirovic, Y. Xu, M. Mavrikakis, R.R. Adzic, Angewandte Chemie International Edition 44 (2005) 2132–2135.

[2] T. Kaito, H. Mitsumoto, S. Sugawara, K. Shinohara, H. Uehara, H. Ariga, S. Takakusagi, Y. Hatakeyama, K. Nishikawa, K. Asakura, J. Phys. Chem. C 118 (2014) 8481–8490.

[3] S. Mukerjee, S. Srinivasan, M.P. Soriaga, J. McBreen, J. Phys. Chem. 99 (1995) 4577–4589.

[4] Q. Yuan, Y. Wakisaka, Y. Uemura, T. Wada, H. Ariga-Miwa, S. Takakusagi, K. Asakura, S.R. Brankovic, J. Phys. Chem. C 122 (2018) 16664–16673.

Chapter 7 General Conclusion

The target of this dissertation was to construct surface sensitive XAFS apparatus for *in-situ* structure investigation used for Pt monometallic or PtM bimetallic model catalyst systems applying well-defined surfaces, which will provide detailed 3D structure information at specific bonding directions at atomic scales. These breakthroughs will theoretically guide the ORR catalyst designs. The obstructs existed in the conventional XAFS methods such as inelastic scatterings low S/B ratio induced in aqueous environment, or the difficulty on study the low concentration system, has been successfully overcame by newly developed XAFS apparatus introduced in this dissertation.

For carbon supported Pt monometallic catalyst structure study, Chapter 3 introduced a model catalyst of flat HOPG supported highly dispersed Pt NPs, which was prepared via a two-phase liquid reduction method and deposited on substrate by spin-coating method. The developed BCLA enhanced EC-BI-XAFS effectively improved the S/B ratio and solved the problems existing in the traditional XAFS methods. The application of BCLA wisely only selected the specific Pt L_3 edge fluorescence signals by placing at a suitable focal point. The BI configuration reduced the X-ray travelling path therefore greatly inhibited the absorption of incident X-ray by solution layer. The structure of Pt NPs was successfully investigated under 0.1 M $HClO_4$ environment with application of potentials corresponding to the real ORR operation conditions. The Pt NPs was proved to possess a stable structure framework of Pt_{309} cuboctahedron model over a wide potential range. Surface adsorbates evolution was studied by XANES study, which revealed a potential dependent surface adsorbates trend, where H adsorption at 0.1 V_{RHE} involves into the -OH adsorption between 0.6 V_{RHE} to 0.8 V_{RHE}, and finally involves into -O adsorbates at higher potential of 1.0 V_{RHE}. This

unique BI configuration could be further applied to other catalyst systems to track structure framework as well as surface adsorbates evolvement under *in-situ* conditions.

Due to the nature drawbacks of carbon supports induced corrosion, and deactivation of Pt monometallic catalyst, research trend has been converted to bimetallic Pt-based catalyst system studies, which possess a higher utilization of expensive noble metals and more outstanding ORR catalytic activity when compared with commercially used Pt/C powder catalysts. Chapter 4 challenged to came up with an *in-situ* EC-(P)TRF-XAFS apparatus to investigate the structure of bimetallic catalysts under acidic ORR working environment and distinguish the individual roles of bimetallic components for improved ORR performance, where PtAu bimetallic model catalyst system with high reflectivity surface was used. Given the successful experience in applying BCLA only selecting specific fluorescence signals, efforts have been made in this chapter to equip the *in-situ* EC-(P)TRF setup with BCLA. Due to low concentration of mode catalyst system limitation, the total reflection configuration ensure the X-ray penetrate at the critical angle, which avoid long path of incident X-ray within solution layer and consequently reduced the solution induced scattering background signals. The polarization dependent feature enables the structure investigation from different bonding directions, which enables the Pt-Pt bonding and Pt-Au bonding investigation individually. For structure investigation without solution and with higher Pt deposition amount, the BCLA can significantly improve the S/B ratio by choosing suitable ROI region where Au fluorescence signals could be avoided for SDD. Therefore, it is possible to combine the portable monochromator BCLA and (P)TRF-XAFS technique for bimetallic catalyst system structure study. However, when applying the BCLA to lower Pt concentration system ~ 0.1 ML in aqueous environment, neither S/B ratio nor the S/N ratio was significantly improved. This is due to the huge background within electrolyte was too large to be simply removed by BCLA

application. The negative solution effect should be eliminated by considering applying a thinner solution layer. The BCLA would not be applied in the following practical application chapters involving *in-situ* bimetallic model catalyst system studies. In a word, the developed *in-situ* EC-BCLA+(P)TRF-XAFS is a powerful structure investigation method, which could be further applied for bimetallic catalyst system studies especially effective for those not including neighboring elements.

Chapter 5 and Chapter 6 discussed the feasibility of *in-situ* EC-PTRF-XAFS apparatus in Pt_{subML}/Au (111) model catalyst structure study. Previous group work reported UPD of Cu monolayer and galvanic replacement reaction between Cu sacrificial layer and Pt^{4+} ions lead to mixture products, where 60 % was SD process induced [$PtCl_2$] complex without replacement reaction, and 40 % are metallic Pt species, which was derived from the assumed SLRR process. However, several problems remains unclear. For example, what is the as-prepared structure of Pt complex obtained via SD process without Cu UPD ML? How does the strain effect work in the reduced Pt_{subML}/Au (111) model catalyst system? Chapter 5 and Chapter 6 investigated these questions in detail. In chapter 5, 0.2 ML Pt was prepared via facile SD process without Cu UPD and Pt SLRR processes interference. XPS proposed a different Pt/Cl ratio as 4 instead of 2, where the latter was proposed by Yuan et al. Feff8 theoretical analysis proved the as prepared sample possess a structure of Pt atoms surrounding 4 Cl atoms. Chapter 6 confirmed the reduced Pt_{subML}/Au (111) model catalyst prepared via UPD and SLRR recipe, as Yuan et al. reported one gave an expanded Pt-Pt bond distance even reached to that of Au-Au bond distance (2.88 Å) in Au bulk due to the strain effect induced by Au (111) substrate. The developed *in-situ* EC-PTRF-XAFS overcame the problems in aqueous environment XAFS investigation like the solution blocked and low amount of Pt species limited detection restrictions, where the high surface sensitivity property

contributed to investigating the intermediate as well as products during the SLRR process, which may provide a new perspective in understanding the galvanic replacement reaction mechanism and further contribute to the catalyst design principles. This developed method should play an essential role in *in-situ* catalytic structure determination for model catalyst system studies.

In this PhD work, three surface sensitive *in-situ* XAFS techniques were developed to determine the geometric and electronic structures at atomic scales based on several kinds of model catalyst systems with well-defined surfaces under the real ORR operating conditions, instead of providing an averaged structure information using traditional porous powder catalysts. These unique techniques overcame the limitations of typically applied surface science methods, such as high demand for UHV conditions for valence state studies, or high requirements for sample preparation and crystalline properties. It also overcame the conventional XAFS method limitations in aqueous environment detections, such as the solution induced inelastic scatterings, which worsen the S/B ratio. Surface adsorbates, 3D geometric structure as well as intermediates distinguishment during chemical reactions were realized in this dissertation. Related catalytic activity test work for prepared model catalyst systems mentioned in this dissertation are under preparation, which will help to establish the relationship between the catalysts structure and corresponding ORR catalytic activity. This PhD work will contribute to the fundamental research of ORR catalyst mechanism investigation and further providing catalyst design guidance for fuel cell systems.